Mechanical Behaviour of Cam-type Femoroacetabular Impingement

A Thesis submitted to The University of Manchester for the degree of Doctor of Philosophy in the Faculty of Engineering and Physical Sciences

2014

David Jimenez-Cruz

SCHOOL OF MECHANICAL, AEROSPACE AND CIVIL ENGINEERING

TABLE OF CONTENTS

LIST OF FIGURES

LIST OF TABLES

ABBREVIATIONS

00_RES_H	Model / 0 millimetres resection depth / healthy bone properties
00_RES_OP	Model / 0 millimetres resection depth / osteoporotic bone properties
06_RES_H	Model / 6 millimetres resection depth / healthy bone properties
06_RES_OP	Model / 6 millimetres resection depth / osteoporotic bone properties
12_RES_H	Model / 12 millimetres resection depth / healthy bone properties
12_RES_OP	Model / 12 millimetres resection depth / osteoporotic bone properties
2D	Two-dimensional
3D	Three-dimensional
AIT	Anterior Impingement Test
AP	Antero-posterior
Area A	Inferior-medial resection area
Area B	Superior-medial resection area
Area C	Superior-lateral resection area
Area D	Inferior-lateral resection area
ASIS	Anterior superior iliac spine
C3D4	Continuum / three dimensional / 4 node element
CAD	Computer-aided design
CDM	Continuum Damage Mechanism
CG	Centre of Gravity
CT	Computed Tomography
DICOM	Digital Imaging and Communications in Medicine
DPM	Damage Plasticity Model
FABER	Flexion Abduction External Rotation
FAI	Femoroacetabular Impingement
FCS	Flexion Coordinate System
FE	Finite Element
FEA	Finite Element Analysis
FEM	Finite Element Method
FEP	Femoral Epicondyle
FM	Failure Mechanism
GDS-HL	Going Downstairs activity subjected to High Loading

H	Healthy bone
HN	Head-Neck
IGES	Initial Graphics Exchange Specification
JCS	Joint Coordinate System
MRA	Magnetic Resonance Arthrography
MRI	Magnetic Resonance Imaging
NM	Not Measurable
OA	Osteoarthritis
OP	Osteoporotic bone
P-I	Model Patient number 1
P-II	Model Patient number 2
P-III	Model Patient number 3
P-IV	Model Patient number 4
PSIS	Posterior Superior Iliac Spine
P-V	Model Patient number 5
P-V_RT	Model Patient number 5 after virtual osteochondroplasty
P-VI	Model Patient number 6
P-VI_POST	Model Patient number 6 after actual osteochondroplasty
P-VI_PRE	Model Patient number 6 before actual osteochondroplasty
P-VI_RT	Model Patient number 6 after virtual osteochondroplasty
RCS	Rotation Coordinate System
RoM	Range of Motion
RT	Resection Tool

NOMENCLATURE

$\lVert \vec{AB_f} \rVert$	Magnitude of the vector $\vec{AB_f}$
$\lVert \vec{AB_i} \rVert$	Magnitude of the vector $\vec{AB_i}$
$\vec{AB_f}$	Vector from point $A(x, y, z)$ to point $B_f(x_f, y_f, z_f)$
$\vec{AB_i}$	Vector from point $A(x, y, z)$ to point $B_i(x_i, y_i, z_i)$
S_{E_i}	Von Mises stress in the *ith* element
V_{E_i}	Volume of the *ith* element
$A(x, y, z)$	Origin coordinates to measure the range of motion
$B_f(x_f, y_f, z_f)$	Final coordinates for the range of motion measurements
$B_i(x_i, y_i, z_i)$	Initial coordinates for the range of motion measurements
CG	Centre of Gravity
cos	Cosine of an angle
cos^{-1}	Angle that has a cosine equal to a given number (arccosine)
F	Resultant Force failure analysis
F_{FH}	Reaction Force on Femoral Head resection depth analysis
F_M	Reaction Force from Abductor Muscles resection depth analysis
GPa	Gigapascal (10^9 Pascal)
mm	Millimetres
MPa	Megapascal (10^6 Pascal)
N	Newton
^{o}	Degrees
sin	Sine of an angle
W	Body Weight
Θ	Internal Rotation Range of Motion
Θ_1	Angle between action lines of Body weight and Reaction Force on Femoral Head
Θ_2	Angle between action lines of Body weight and Reaction Force from Abductor Muscles
ρ	Density
v	Poisson's ratio
Σ_i	Summation of the ith value
E	Young's modulus

a	Constant to relate Young's modulus and density
b	Constant to relate Young's modulus and density
ε_t^{pl}	Tensile plastic strain
ε_c^{pl}	Compressive plastic strain
k	Proportional constant on Hooke's Law
x	Displacement on Hooke's Law
{F}	Force matrix
[K]	Stiffness matrix
{u}	Displacement matrix

ABSTRACT

Femoroacetabular impingement (FAI) is a hip condition which can limit hip motion and cause pain particularly in young and athletic patients. It is considered as a patho-mechanical process leading to progressive and degenerative damage of the joint. Surgical treatment for femoroacetabular impingement focuses on improving the clearance for hip motion, reducing the femoral impact against the acetabular labrum. The procedure involves the surgical resection of the cause of impingement which consists of trimming the acetabular rim and/or the femoral head-neck offset.

Currently, there are no comprehensive tools available for pre-operative planning of FAI surgery and so the area and depth of bone resection are identified based on the skill and experience of the surgeon. This means that it is difficult to predict the degree to which the procedure will be successful, in terms of reducing pain and increasing the range of motion (RoM) of the hip, prior to surgery. In addition, resection can lead to increased stress in the remaining bone which in some cases can result in post-operative femoral neck fracture, a recognized risk of FAI surgery which is increased if the bone is osteoporotic.

This thesis describes the development of a framework that will enable a tool to be created that can be used for the diagnosis, preoperative planning and selection of treatment for patients with cam-type FAI. The framework consists of a number of complementary 3-dimensional finite element (FE) models. The models are created from computer tomography (CT) data from actual patients with cam-type FAI. The first FE model was developed in order to predict the stress distribution in the head-neck region of the femur following resection surgery for FAI enabling the effect of resection depth to be investigated under loading conditions corresponding to typical daily activities. The model demonstrates that resection depth should be kept to less than one third of the diameter of the neck in order to ensure structural integrity. The second finite element model developed utilises a quasi-brittle damage plasticity material formulation to investigate the mechanism and risk of femoral neck fracture following femoral osteochondroplasty in osteoporotic and non osteoporotic hips. Predictions indicate that fracture can occur in osteoporotic hips during typical daily activities. Also, the likelihood of fracture increases when patients are subjected to high load conditions and activities, even in non-osteoporotic patients. The third FE model was developed to assess the reduction in the internal rotation movement in hips with cam-type FAI and identify and examine the areas where impingement occurs. The model shows that FAI can result in a significant reduction in hip motion and that impingement area and RoM are patient dependant. All three FE models were validated with results from experimental studies.

The three models combined provide the framework for a virtual osteochondroplasty tool. The procedure for using the tool involves undertaking a virtual resection of a FAI hip based on the areas of impingement identified by the RoM analysis provided by the third FE model. Finite element models one and two are employed to ensure that the virtual resection remains within safe limits and stress does not elevate in the remaining bone to levels that would significantly increase the risk of femoral neck fracture. The framework was validated by comparing the RoM predicted following a virtual osteochondroplasty undertaken on a model of a hip from an actual patient with FAI with the results from a model of the same hip created from CT scan data taken after an actual osteochondroplasty had been performed on the patient using a resection area and depth identified in the conventional way by a surgeon.

DECLARATION

No portion of the work referred to in the Thesis has been submitted in support of an application for another degree or qualification of this or any other university or other institute of learning.

COPYRIGHT

The author of this Report (including any appendices and/or schedules to this report) owns certain Copyright or related rights in it (the "Copyright") and he has given The University of Manchester certain rights to use such Copyright, including for administrative purposes.

Copies of this Report, either in full or in extracts and whether in hard or electronic copy, may be made only in accordance with the Copyright, Designs and Patents Act 1988 (as amended) and regulations issued under it or, where appropriate, in accordance with licensing agreements which the University has from time to time. This page must form part of any such copies made.

The ownership of certain Copyright, patents, designs, trademarks and other intellectual property (the "Intellectual Property") and any reproductions of copyright works in the Report, for example graphs and tables ("Reproductions"), which may be described in this Report, may not be owned by the author and may be owned by third parties. Such Intellectual Property and Reproductions cannot and must not be made available for use without the prior written permission of the owner(s) of the relevant Intellectual Property and/or Reproductions.

Further information on the conditions under which disclosure, publication and commercialisation of this Report, the Copyright and any Intellectual Property and/or Reproductions described in it may take place is available in the University IP Policy, in any relevant Report restriction declarations deposited in the University Library, The University Library's regulations and in The University's policy on Presentation of Theses.

ACKNOWLEDGEMENTS

Foremost, I would like to express my sincere gratitude to Prof Teresa Alonso-Rasgado, Prof Colin Bailey, and Prof Timothy Board for their support, guidance and constant encouragement over the last four years.

My sincere thanks also goes to Dr Alan Walmsley, and Dr Parthasarathi Mandal for their invaluable help and advice.

I thank my fellow colleagues for their unconditional support, but mainly for their friendship.

I also would like to thank Wrightington Hospital for their important contribution to this research.

Last but not least, I would like to thank The National Council of Science and Technology of Mexico (CONACyT) for the scholarship and the financial support to carry out this project.

CHAPTER I: INTRODUCTION

1.1 Overview

The joints are the means of union between two or more bones of the skeleton, taking charge of movement with the collaboration of muscles and ligaments. They can be classified according to their structure: synovial joints which allow a wide range of movements and the fibrous and cartilaginous joints which have a much smaller range of motion (RoM). They can also be classified according to the function performed: diarthrosis, amphiarthrosis and synarthrosis, which are freely mobile, semi-mobile and immobile, respectively. In the human body most joints are synovial, characterized by their large of range movement and the synovial sides of the joint [1-6].

There are several factors that can lead to restricted or abnormal function of the joints. These factors include congenital abnormalities, abnormalities acquired by growth or extreme physical activity and diseases such as osteoporosis and osteopenia, which affect the bone mineral density. A particular case of bony abnormalities occurs in the hip joint and is known as femoroacetabular impingement (FAI). Femoroacetabular impingement occurs due to irregular morphology of the proximal femur and/or acetabulum causing repetitive damage to the chondrolabral junction and subsequent permanent degenerative changes as a result of the constant impact between the parts of the joint. FAI is thought to be responsible for the development of osteoarthritis in many young patients that was previously described as idiopathic.

The aetiology of the most common abnormalities resulting in femoroacetabular impingement has not yet been identified. Excessive stress concentration produced by playing sports and physical activity, trauma during growth and genetics represent the main reasons for the abnormalities. In addition, there are some post-traumatic surgical procedures and iatrogenic deformities, which also lead to impingement. However, as the aetiology is not yet fully understood, preventive measures are not available at present. The risk of an incorrect diagnosis or the use of inappropriate procedures arrives from the equivocal presentation of the FAI. To prevent

complications like osteoarthritis and to avoid more radical procedures such as arthroplasty, early diagnosis and appropriate treatment of FAI are essential [3, 7-27].

1.2 Research Background

Femoroacetabular impingement is still a little-known cause of hip pain and its diagnosis is often not very accurate. Jäger *et al.*[28] mention an average delay of 5.4 years from the onset of symptoms to diagnosis, while Burnett *et al.*[29] found a 21 month delay in diagnosis with an average of 3.3 visits to different medical specialties.

In the last decade, interest in FAI as well as the number of published scientific publications about it has increased; some of the research has been focused on defining the aetiology, clinical and radiographic assessment and treatment or reshaping surgeries. However, there are no mechanistic studies to provide information of this pathology, its treatment and possible prevention [7-11, 13-15, 17, 18, 21, 23, 24, 28, 29].

In regard to surgical treatment, one experimental study has focused on the depth of resection and its impact on the mechanical performance of the bone. This investigation was based on performing compressive tests on several cadaveric femurs after resection to several different depths [3]. Another study focused on the effect of the accuracy of resection on the femoral head-neck area by performing a computer-assisted osteochondroplasty on resin models and cadaveric femurs [30]. The impact of bone quality on the outcomes of femoral osteochondroplasty has not been investigated; indicating that, more research is required to validate the mechanics, improve diagnosis and treatment of FAI.

1.3 Objectives and Methodology of the Research

The aim of the research described in this thesis was to develop a framework/methodology that would provide the foundation for the creation of a tool that can be used for the diagnosis, preoperative planning and selection of treatment for patients with cam-type FAI. This involved investigating the mechanical behaviour of the hip during cam-type FAI and developing a methodology to predict

the impingement areas to be able to recommend a more accurate surgical procedure based on the conditions of each individual patient. The research project was undertaken in collaboration with Wrightington Hospital, UK. All patient information was provided by the hospital as well as medical advice in terms of anatomy, physiology and development of the virtual medical procedures. Although the framework developed in this thesis was applied to cam-type FAI only, the methodology is general and can be applied for other types of impingement.

To accomplish the aim of the research, it was first necessary to perform a stress analysis in order to determine the safe resection limits for performing an osteochondroplasty for cam-type impingement and to find the impact of femoral osteochondroplasty on the mechanical behaviour of the bone. Once the stress analysis was undertaken, a failure analysis was performed for critical loading conditions in models of healthy and osteoporotic bones after femoral osteochondroplasty to confirm the safe resection depth limits and the impact of the resection if the bones exhibit osteoporosis.

Finally, having determined the resection depth limits it was possible to then perform a virtual osteochondroplasty with the minimal invasive procedure to alleviate the impingement after having determined the bone volume to be removed by first identifying the impingement areas during an internal rotation movement analysis performed on a hip model for each patient. The results of this study will enable surgeons to optimize treatment by identifying the location of the FAI and improving the surgical procedure for each individual case.

A novel set of models of different hip joints with impingement and healthy conditions were developed in order to simulate the behaviour of the joint with anatomic irregularities and to simulate joint function following surgical resection by virtual osteochondroplasty. The three-dimensional (3D) geometries of the bones were constructed in Scan IP® commercial software by using DICOM files (Digital Imaging and Communications in Medicine) from CT (Computed Tomography) scans obtained from patients exhibiting cam-type impingement. Once the geometries were completed, PowerSHAPE Pro® software was used to convert them to solid importable parts and to construct the tools needed to perform the virtual resections.

The final solid geometries were imported into Abaqus CAE® Finite Element Analysis software to perform all the necessary corresponding analyses for the current study [31-33].

The remaining chapters in this thesis are presented as follows: Chapter II a literature review of FAI as a medical concern; dealing with the pathology, diagnosis and treatment. In addition, a review of the relevant research work that helps to address the objectives is presented.

Chapter III describes the structure and function of the hip joint with the purpose of understanding and becoming familiar with the medical terminology, anatomy, and biomechanics of the hip; this chapter also provides descriptions of bone and cartilage, their mechanical behaviour and material characteristics.

Chapter IV provides details of the development of the numerical models, in particular the general process used to create the geometries from CT scans using ScanIP®, production of the solid geometries and performance of the virtual resection using PowerSHAPE Pro®, and, lastly, creation of the final assembly in Abaqus CAE® to perform the Finite Element Analysis. In addition, this chapter presents a stress analysis of the femoral epiphysis after osteochondroplasty for different resection depths during various daily activities.

Chapter V describes a failure analysis of the femoral epiphysis for healthy and osteoporotic bone after femoral osteochondroplasty at different resections depths during critical loading activities.

Chapter VI presents an analysis of the flexion-internal rotation movement of abnormal hips, including calculation of the range of motion (RoM) and identification of the impingement areas on the femoral epiphysis during FAI. The overall framework/methodology developed to address the reduction of range of motion and osteochondral injuries resulting from FAI by performing a virtual osteochondroplasty is then described.

Finally, conclusions of the research are presented in Chapter VII.

CHAPTER II: FEMOROACETABULAR IMPINGEMENT (FAI)

2.1 Introduction

The hip joint has a wide range of motion, supports a substantial proportion of body weight during walking and is fundamental to the movement of the body. The hip joint is frequently subjected to injuries and wear, and so hip pain is a common cause for medical complaint and is present in different diseases and in patients of all ages [1, 2, 4-6, 23, 34].

2.2 Femoroacetabular Impingement

FAI, often referred as hip impingement, is not considered a disease but a pathomechanical process resulting from abnormal morphology of the proximal femur and acetabulum. This results in abnormal contact between the parts of the joint that leads to progressive degenerative damage, mainly in soft tissue, which is critical for the development of osteoarthritis (OA) in younger patients. Frequently, FAI has a confused presentation that hinders correct diagnosis; this constitutes a risk for inappropriate treatment and even surgical procedures. Proper diagnosis of FAI and future treatment are very important in preventing complications such as osteoarthritis and avoiding more radical procedures such as arthroplasty [3, 8, 9, 11-16, 18-27, 35-37].

2.2.1 Pathology

FAI has been reported for over a century and has been identified as a sequel of some childhood diseases such as slipped capital femoral epiphysis or hip dysplasia in childhood. However, FAI was not considered as a mechanical cause of osteoarthritis until the development of open dislocation surgery of the hip, as this procedure allows observation of all the faces of the joint.

In Switzerland, in the early 90's the roots of the current concept of FAI appeared as a result of irregular bone healing on a femoral neck fracture. However, the aetiology of many of the abnormalities that can cause FAI have not been well defined. Physical stresses produced by sports or trauma during development and genetic factors

represent the main reasons for abnormalities in the femoral epiphysis, while there is an important number of post-traumatic and iatrogenic deformities, such as dysplasia, femoral retrotorsion, and femoral varus osteotomy or retroversion after pelvic osteotomy that may lead to FAI. However, because there is no clear aetiology, preventive measures are generally not effective [3, 8, 9, 11-16, 18-27].

The current concept of FAI was postulated by *Ganz et al.* [18], as a pathological process that causes mechanical impingement when an abnormality exists in the shape of one or both bones of the hip. These anatomic abnormalities reduce clearance in the hip and with it the range of motion, resulting in acetabular cartilage and labrum injuries, hip pain and eventually arthrosis [9]. Alternatively, FAI can occur in a normal shaped hip, as a consequence of an extreme rate of motion [8].

The antero-superior area of the femoral head-neck junction and the acetabular rim are the regions where abnormal contact occurs more frequently. Consequently, damage occurs in the supra-lateral area of the joint, sustained during flexion and internal rotation of the hip. Figure 2.1 shows the areas of bone excess which are the cause of FAI [9, 11, 16, 23, 25].

Figure 2.1 Excess of bone causing FAI. (a) Femoral head-neck; (b)Acetabulum (modif.) [38].
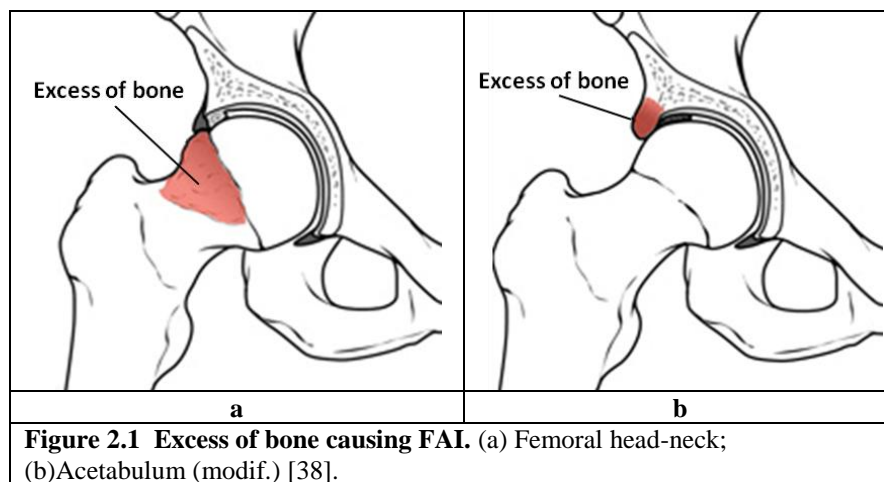
2.3 Types of Femoroacetabular Impingement

In FAI, the femoral head remains well-centred, but freedom of movement is limited either by abnormality of the acetabulum, the proximal femoral epiphysis or a combination of both.

Two types of mechanisms of FAI have been described, based mainly on intraoperative observations of the injuries. When the clearance of motion is limited by the acetabulum, this condition is known as "Pincer Impingement" whereas if movement is limited by some malformation in the femoral epiphysis, it is known as "Cam Impingement". Some 86% of patients present both abnormalities at the same time, which is known as "Mixed Impingement". Figure 2.2 shows the normal shape of the hip joint and the three different femoroacetabular impingement types [3, 9, 11, 14-16, 18-20, 23, 27, 39-42].

Figure 2.2 Types of femoroacetabular impingement. (a) Normal; (b) Cam; (c) Pincer; (d) Mixer.
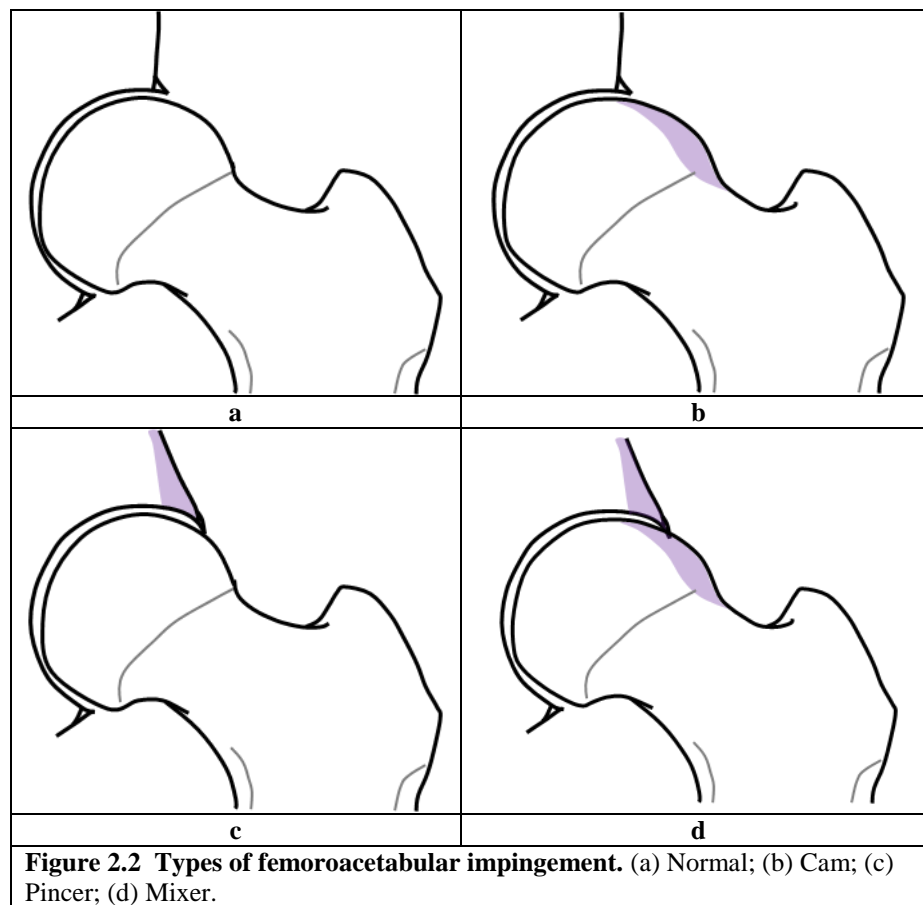
2.3.1 Cam-type Impingement

Through the years, this bone deformity has been known as "pistol grip" or "postslip" morphology and is more common in young athletic men around 30 years old. The characteristics of cam-type impingement include a synovial herniation pit, a dysplastic "lump" and a "pistol grip" deformity, which are typically located on the anterior-superior and lateral region of the femoral head, where the femoral head and the neck meet.

The cam mechanism occurs when a nonspherical femoral head or an insufficient concavity between the neck and head of the femur, enters into a morphologically regular acetabulum. Normally, this area of the proximal femur has a concave configuration but in this type of impingement, it is flattened or convex.

This pathomechanical process is more frequent in young athletic males and occurs mainly during flexion of the hip. As the hip is flexed, there is a shear stress in the superior-anterior acetabular cartilage at the labral cartilage junction. As a consequence of the shear forces, an outside-in abrasion occurs on the acetabular cartilage and/or on the labrum and bone in the region, leading to a detachment of the labrum. Osteophyte formation can occur after repetitive impingement between bones which can lead to further more serious problems.

It has been suggested that FAI may be a consequence of an asymptomatic slipped capital femoral epiphysis. Other evidence suggests the development of these abnormalities may be a result of defective elongation of the femoral common physis between greater trochanter and femoral head that may lead to a reduction in the concavity of the femoral head-neck junction. There is also evidence that the cam impingement may occur as a result of femoral retrotorsion or any abnormal increase in the neck-shaft angle, resulting in the condition known as coxa valga. Figure 2.3 illustrates the reduction in the range of movement caused by the dysplastic neck/ head lump in cam-type impingement which increases the risk of a subtle joint subluxation [3, 9, 11, 13-16, 18-20, 23, 25, 27, 28, 39-43].
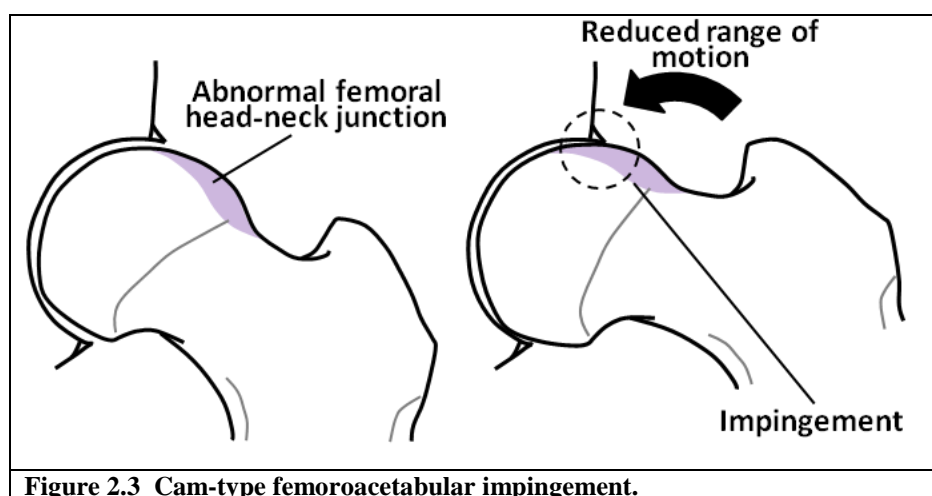
Figure 2.3 Cam-type femoroacetabular impingement.

2.3.2 Pincer-type Impingement

Women around 40 years old are the most common patients to have pincer type impingement. As in the cam-type impingement there is not a well-defined aetiology, although it is associated with some disorders such as slipped capital femoral epiphysis, acetabular retroversion, coxa profunda or post-traumatic dysplasia which leads to acetabular over-coverage. In this type of impingement, contact between bones occurs on the antero-superior region of the femoral epiphysis as in cam-type impingement, but in this case it is a consequence of the abnormal acetabular shape.

Unlike cam-type impingement, pincer impingement produces damage in a very restricted area of the hip; just a thin line near the acetabular rim leading to limited and small chondral lesions, however, the repetitive impact on the labrum produces abrasion and ossification in the soft tissue resulting in a progressive increase of the over-coverage of the femoral head. As in cam-type impingement, failure to diagnose the pathology may lead to osteoarthritis of the hip. Figure 2.4 shows the excessive acetabular coverage which reduces the range of movement. Table 2.1 compares the main characteristics of the two types of FAI [3, 9, 11, 13-16, 18-20, 23, 25, 27, 39-42].
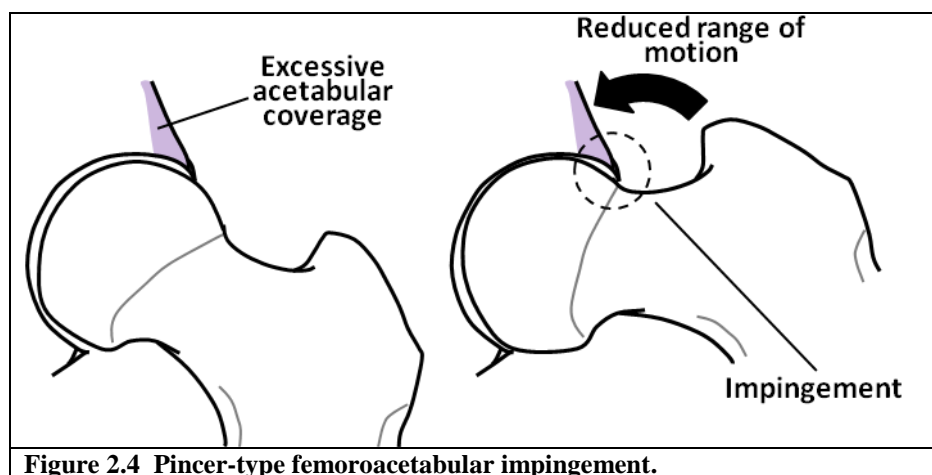
Figure 2.4 Pincer-type femoroacetabular impingement.

Table 2.1 Characteristics of femoroacetabular impingement [25]**.**

CRITERIA	CAM-TYPE	PINCER- TYPE
Cause	- Nonspherical head - Neck/head "lump"	-Focal or general over-coverage
Mechanism	Jamming of abnormal portion into acetabulum	Linear contact between overcovering rim and head/neck junction
Sex distribution (M:F)	14:1	1:3
Average age (range)	32 (21-51)	40 (40-57)
Typical location of cartilage damage	-Antero-superior -Lateral	-Circumferential with contrecoup
Average depth of cartilage damage	11 mm	4 mm
M:F → Male:Female		

2.4 Symptoms and Diagnosis

Primary presentation of FAI starts with the slow onset of groin pain, typically after a minor impact. Pain is intermittent in the initial phases of the disease, but increases according to the demands required of the joint such as athletic activities, immobilization for long periods, and even during long walks.

The initial symptoms are stiffness in the groin region or in the anterior side of the thigh, as well as inability to flex the hip further than 90 degrees.

During the second phase of symptoms, some movements become uncomfortable for the patients such as tying shoelaces or flexing the hip towards the trunk, with the rate of internal rotation motion reduced and occasionally the joint locks and gives way [11, 19, 22, 25].

2.5 Physical Evaluation

All patients are subjected to systematic physical examination, including a range-of-motion in flexion, extension, abduction, adduction, and external and internal rotations. The two principal tests to diagnose FAI, are the Anterior Impingement Test and the Flexion Abduction External Rotation Test (FABER) [11, 19, 22, 25].

2.5.1 Anterior Impingement Test

The Anterior Impingement Test (AIT) requires the examiner to flex the hip to 90º gently, followed by a forced adduction and internal rotation, as is shown in Figure 2.5. The final position brings the femoral neck-head junction close to the antero-inferior region of the acetabulum, and recreates the position that can lead to impingement. Outcomes from the AIT can be positive or negative based on the pain signals from the patient. A positive result is considered when pain is experienced during the test due to contact of the injured areas. Absence of pain is considered as a negative test outcome [19, 23, 25].
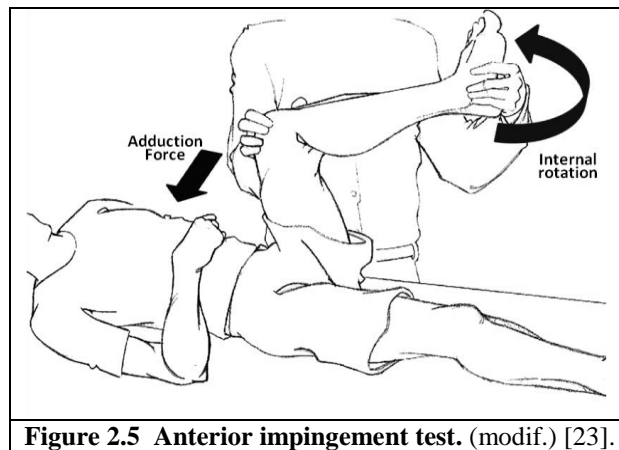
Figure 2.5 Anterior impingement test. (modif.) [23].

2.5.2 FABER Test

Initially, the FABER test was performed on golfers with pathologies of the hip and spine. The test starts with the patient in the supine position with the leg in a figure-four position following the movement sequence of flexion/abduction/external rotation. Secondly, a downward force is applied perpendicularly to the leg and the body is stabilized by applying a force to the contra-lateral hip as is shown in Figure 2.6. The test is positive for impingement when the vertical measurement taken from the lateral side of the knee to the diagnostic table is less when compared with a hip free of pathology. When this occurs it is due to the abnormal shape of the hip which restricts the femur in achieving the target position causing pain by the contact of the injured areas [22].
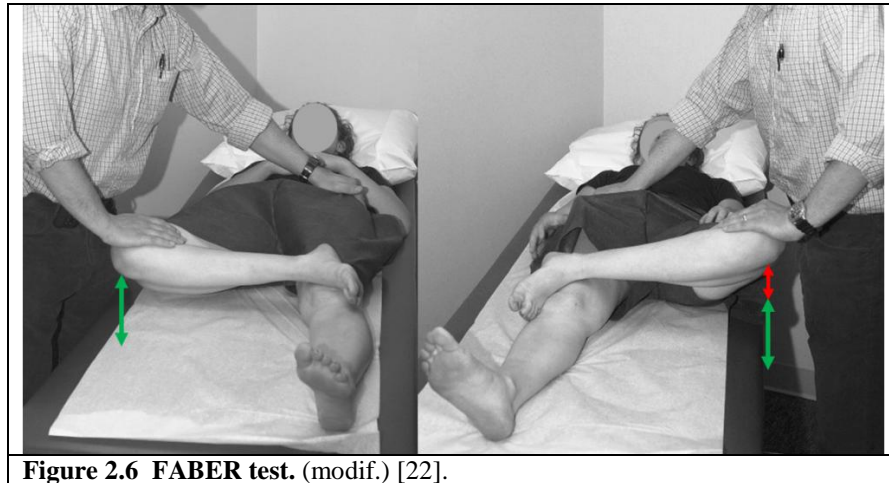
Figure 2.6 FABER test. (modif.) [22].

2.5.3 Imaging Assessment

Plane X-rays are the primary procedure to diagnose any abnormality of the bones. However, for the assessment of the abnormalities that cause impingement, 2D radiographs are sometimes not adequate, because the abnormalities are not clearly shown.

A very complex radiograph set is needed for the assessment of the FAI. For acetabular retroversion, an antero-posterior (AP) pelvic radiograph is needed because a radiograph of a hip alone does not permit the viewing of bony abnormalities. For cam-type impingement the common bump deformity is frequently seen in an AP pelvis view, because most of the non-spherical extensions of the femoral head are in the anterior region. Finally, rim ossification and retroversion of the acetabulum may also be seen in the marks on the anterior edge of the acetabulum [10, 14, 18, 22].

However, plane radiographs are not able to localize abnormalities on the femoral borderline or antero-superior abnormalities. To get a better view of the intra-articular alterations that are not easily detectable with common X-ray it is necessary to use another imaging method such as magnetic resonance imaging (MRI) or magnetic resonance arthrography (MRA).

Currently, MRA is the most helpful method in diagnosing labral pathologies. MRA has the capability to define abnormalities properly, principally in patients who present hip dysplasia and impingement and so resulting in better treatment. Figure 2.7 shows the two types of FAI in plane radiographs [10, 14, 18, 22, 44, 45].

Figure 2.7 Radiographic assessment of FAI. (a) Cam-type; (b) Pincer-type. (modif.) [18, 25].
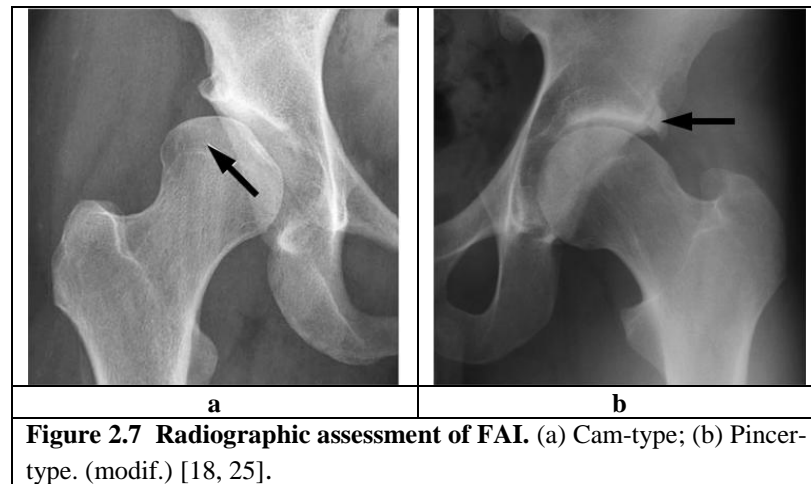
2.6 Treatment of Femoroacetabular Impingement

The first phase of treatment is a conservative plan, which includes modification of all activities that may have an impact on impingement, for example sports, and also reduction of excessive motion and loading on the hip. Early treatment includes the administration of anti-inflammatory medications to reduce the pain. However, extended pain treatment may hide the symptoms of worsening pathology. Physiotherapy focused to improving the range of movement is used; however, it could result in an iatrogenic injury.

Despite the attempts of conservative treatment on high activity patients, surgical procedure is often the only way to effectively treat this pathology. The surgical procedure is commonly known as osteochondroplasty for hip impingement; which is a procedure to repair or modify both bony and cartilaginous structures [3, 8, 10, 11, 14, 18, 19, 21, 25, 39, 46-48].

Osteochondroplasty focuses on improving the space for the movement of the hip and reducing impact of the femur against the acetabular edge. The type of treatment modality performed is determined primarily by the morphological abnormality that gives rise to the FAI.

In pincer-type impingement, over coverage of the acetabulum is modified. Figure 2.8a shows an example of a resection of the acetabular rim. In cam-type impingement, the RoM of the femoral head-neck is optimized by increasing the sphericity of the head as is shown in Figure 2.8b. Osteochondroplasty for hip

impingement is carried out by open surgical or arthroscopic procedures [3, 11, 14, 18, 19, 25, 46, 47, 49, 50].

Before resection	After resection
a	
Before resection	After resection
b	

Figure 2.8 Osteochondroplasty for FAI. (a) Acetabular resection; (b) Femoral head resection. (modif.) [19].
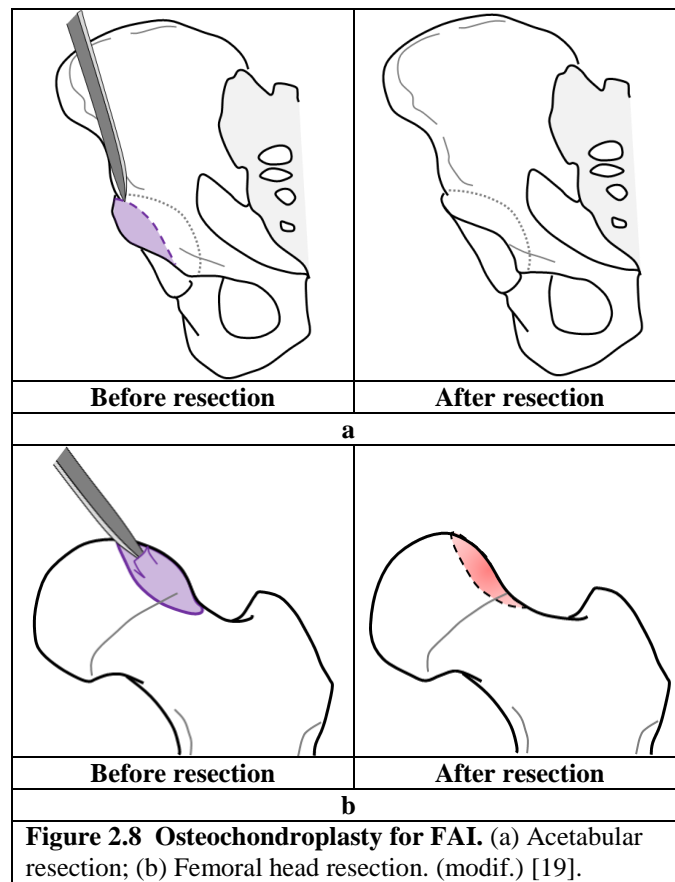
2.6.1 Open Surgical Treatment

The main objectives of surgical treatment for FAI are basically, to improve hip motion and reduce the impact between the femoral head-neck junction and the acetabulum. This procedure consists of a surgical resection or reshaping of the abnormal morphologies in the bones. One of the surgical procedures involves hip dislocation to allow a 360° view of the hip. This treatment usually has successfully mid-term results [18].

Open surgical techniques are usually more precise in dealing with impingement abnormalities; also these techniques allow resections of the head/neck, the base of the femoral neck and in the intertrochanteric region. Figure 2.9 shows how the dislocation surgery is performed. The open technique has become the main surgical treatment for FAI with more than 70% of procedures showing excellent results [3, 8, 11, 18, 19, 21, 25, 39].
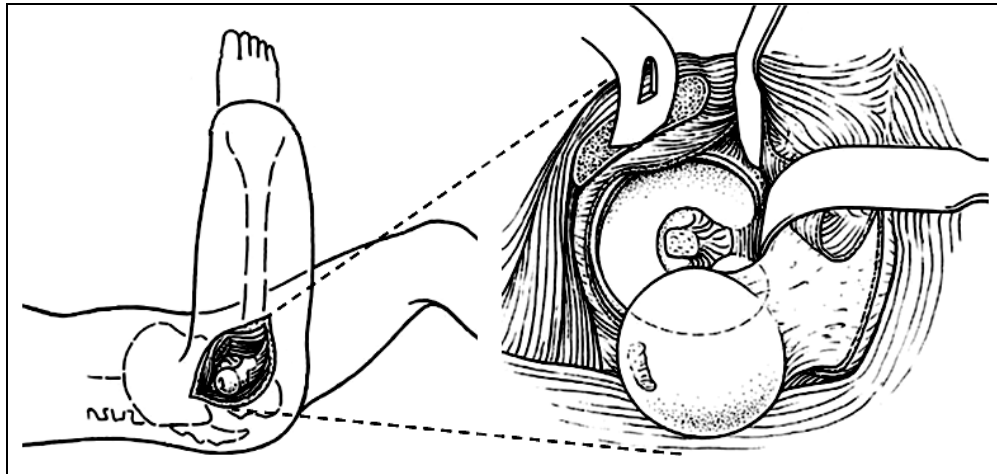
Figure 2.9 Surgical dislocation of the hip as treatment for FAI. (modif.) [19].

2.6.2 Arthroscopic Treatment

Arthroscopy is a minimally invasive procedure performed by the introduction of a visualization/illumination device called an arthroscope through a small incision, and one or two extra small incisions to introduce the irrigating and trimming instruments to perform the procedure. Minimal damage in healthy tissues during arthroscopy, and consequently, faster healing are the main advantage over the open technique as shown in Figure 2.10. However, the limited space available in this technique is a disadvantage in obtaining a proper view of the tissues involved during the surgery [3, 11, 14, 18, 19, 25, 46, 47, 49, 50].
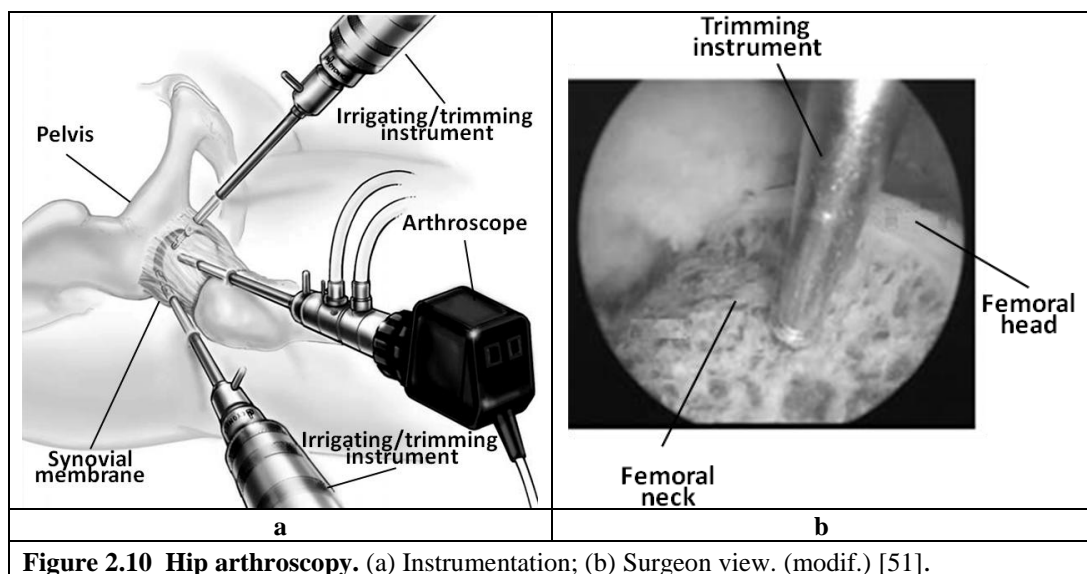
Figure 2.10 Hip arthroscopy. (a) Instrumentation; (b) Surgeon view. (modif.) [51].

2.7 Research Approaches to Address FAI Issues

Although a number of research findings have been documented regarding FAI, many of them are focus on issues such as aetiology, diagnosis, and surgical procedures from the medical point of view. However, from the mechanical point of view, there is still a lack of information about the mechanical behaviour of FAI, the mechanical impact of the surgical procedures and its consequent risk of fracture. Currently, multidisciplinary research techniques which combine imaging methods, virtual modelling and analyses in cadaveric and composite bones are employed by researchers in an attempt to answer the unsolved concerns about FAI.

Imaging methods have been used to study the effect of geometric variables on the FAI mechanism. Wyss *et al.*[37] analyzed the effectiveness of the use of MRI to prognosticate clinical symptoms. This study compares the physical examinations and the analysis of the MRI performed on subjects diagnosed with FAI and a control group of asymptomatic patients. A positive correlation (0.97) was found between the internal rotation RoM at 90º of flexion and the beta angle measured in the MRI. Two imaginary lines running through the centre of the femoral head define the beta angle, the first line going to the lateral limit of the acetabulum and the second going to the point where the cortical cortex exceeds the radius of the femoral head, as is illustrated in Figure 2.11a.

Moreover, Beaule *et al.*[52] demonstrated the usefulness of 3D CT scans as a noninvasive method to study FAI by comparing the measurements of the alpha angle on symptomatic patients and a control group. The alpha angle is defined by a line extended from the axis of the femoral neck (through the centre of the femoral head) and a line from the centre to the femoral head to the point where the cortical cortex exceeds the radius of the femoral head, as shown in Figure 2.11b.

a	b

Figure 2.11 Imaging methods approach to FAI concerns. (a) Measurements in MRI; (b) Measurements in CT scan. (modif.) [37, 52].
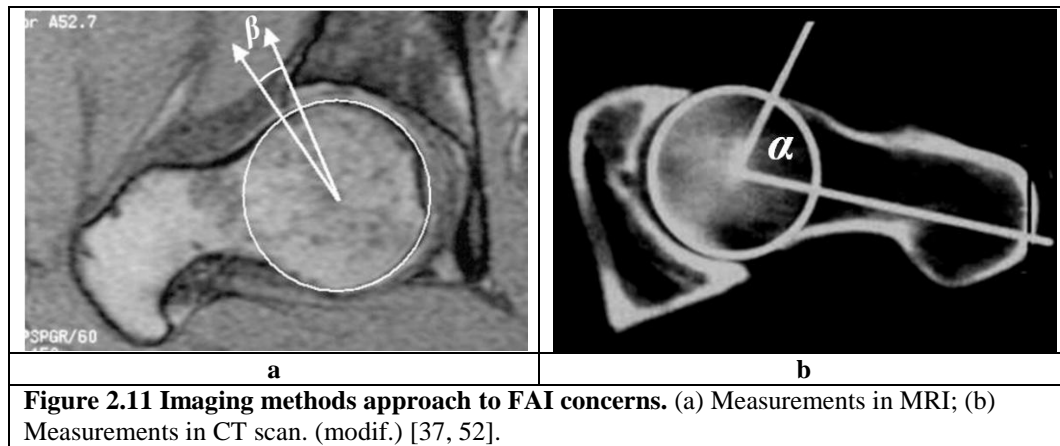
With regards to mechanical studies about surgical treatment for FAI, the only study to date to address the issue of femoral osteochondroplasty was undertaken by Mardones *et al.*[3]. It was a cadaveric study to evaluate the safety of the surgical techniques by testing 15 pairs of femurs in compression. One of the femurs was included in a control no-resection group and the corresponding femur of the pair was subjected to the resection, which was varied in depth from 10% to 50% of the diameter of the femoral neck. In this study, all femurs were tested until fracture.

The results indicated that the 10% resection depth group did not show any significant difference in the values of peak loads and energy to fracture compared with the corresponding control group. The results for the 30% resection depth group showed a reduction of around 15% in the values of peak loads and energy to fracture between the resection specimens and their corresponding non-resection control pair.

Finally, the results of the 50% resection depth group indicated a significant reduction in the peak loads needed to fracture compared with the corresponding, non-resection control pair, reaching approximately 1200N before fracture. In this group, all the fractures in the resected femurs occurred in the resection areas as a consequence of structural weakening caused by the removal of material in that region; whereas in their control pairs, fractures occurred away from the femoral head-neck shaft [3].

Regarding the use of three-dimensional (3D) models to investigate the range of motion (RoM) in patients with FAI, Tannast *et al.*[53] demonstrated a reduction in RoM using software based on a CT scan, which was validated with cadaveric and resin hips. Tannast *et al.*[53] analysed the reduction in RoM during internal rotation

movement at 90º of flexion. However, the study had substantial limitations such as the absence of cartilage and material properties in the models, and the model could not be applied in hips presenting a large dysplasia and advanced osteoarthritis.

Chegini *et al.*[54] analysed the stress distribution in the hip as a result of FAI; in this study they demonstrated the relation between irregular geometry and activities with stress concentration. However, the major limitation of this study was the use of CAD-created geometries, which are highly different to the geometries obtained from CT scans.

Lopes *et al.*[55] developed a subject–specific 3D model from magnetic resonance arthography (MRA) to evaluate contact pressures in the femoral and acetabular cartilages as a consequence of FAI. This study compares the contact pressure at four predefined nodes in the expected impingement areas and the angular displacements in the model with those obtained in the clinical analysis of the patient before surgery. Although this appears to be the only study in the literature which includes actual FAI abnormal geometries, it still has limitations such as the absence of bone material properties, exclusion of ligaments and the lack of more patient models to compare the results.

Furthermore, Clinical Graphics© has recently developed a 3D motion simulator to help surgeons to localize affected areas and RoM of impinged hips. By using CT-scan based 3D models, Clinical Graphics'© software simulates the RoM from geometric anatomic parameters of the bones such as femoral alpha angle, femoral head coverage and acetabular orientation. This software has recently emerged as a useful visualization tool, providing insight into the functioning of the hip; however, it is still not considered as a replacement for the diagnosis methods but rather as a tool to help define the surgical procedures to be performed in a hip already diagnosed. Clinical Graphics'© models only provide geometric visualization of the bones and do not include cartilaginous geometries, ligaments or material properties [56].

CHAPTER III: ANATOMY AND BIOMECHANICS OF THE HIP

3.1 Introduction

The adult human skeleton has 206 bones which represent approximately 12 to 15% of the total body weight. It is a mobile framework of bones connected at several joints, which provides support and protection for the softer tissues and the internal organs [57-63].

Commonly known as the hip, the coxo-femoral joint is formed by the connection between the innominate to the proximal femur. The hip is basically the joint between the trunk and the lower limbs and therefore is essential for weight transmission during human motion.

The hip is able to support all the body weight on one leg and maintain a stable weight transfer particularly in the movement of the trunk on the femur as occurs during walking or running. Alterations in the form of the femur and pelvic bone, and alignment of the hip can change the distribution of stress, leading to bone and cartilage damage and arthritis [1, 2, 5, 6, 64-68].

3.2 Hip Anatomy

The hip is the most proximal synovial joint in the lower limb and is composed of the femoral head and the acetabulum, as illustrated in Figure 3.1. As in all synovial joints, the hip has a capsule surrounding the articulating surfaces, which contains lubricating synovial fluid within that capsule.

The hip articulation has a loose capsule and it is surrounded by long muscles. A strong layer of hyaline cartilage covers both contact surfaces of the joint which are the femoral head and the lunate surface of the acetabulum.

The hip is the largest and most stable joint in the body; this stability is provided by the rigid ball and socket configuration with the round femoral head articulating within the round acetabular socket; the main functions are locomotion and support. When the human body is standing erect, the acetabulum does not completely cover

the femoral head, leaving the antero-superior area of the femoral head exposed. This is the main sign of the erect posture and bipedalism, because the femoral head and acetabulum coincide only when the thigh is in a quadrupedal position [1, 2, 5, 6, 64-68].
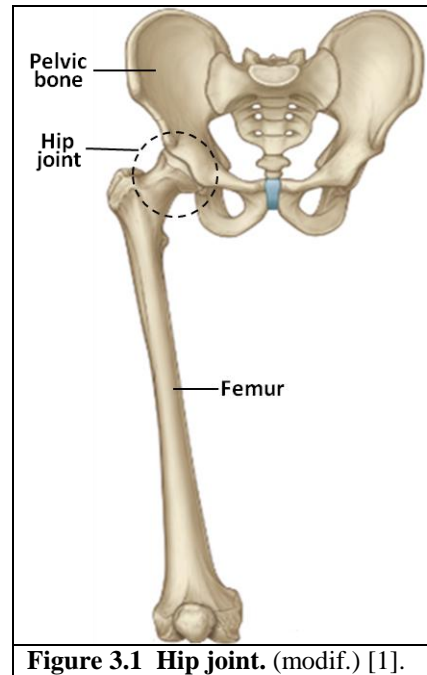
Figure 3.1 Hip joint. (modif.) [1].

3.2.1 Acetabulum

The acetabulum is a quasi-hemispherical concavity on the outer surface of the pelvis formed by the union of three components: ilium, ischium and pubis. Figure 3.2 shows that the acetabulum is divided into five parts; the pubis forms the anterior one-fifth, the ischium forms the inferior-posterior two-fifths and the superior-posterior two-fifths are formed by the by the ilium, which covers more than 50% of the femoral head [1, 2, 5, 6, 64-68].

The acetabular cavity is covered by a smooth crescent-shaped articular surface (the lunate surface) which lines the sides of the socket and is interrupted inferiorly by the deep acetabular notch. Also, Figure 3.2 shows that the acetabulum is surrounded by a fibrocartilaginous rim known as the acetabular labrum.

In the anatomical position, the acetabulum is located on the lateral surface of the pelvis; it is directed obliquely forward, outward and downward. A plane through the

labrum would intersect a sagittal plane at a posterior angle of 40° opening posteriorly and with a transverse plane at a lateral angle of 60°.
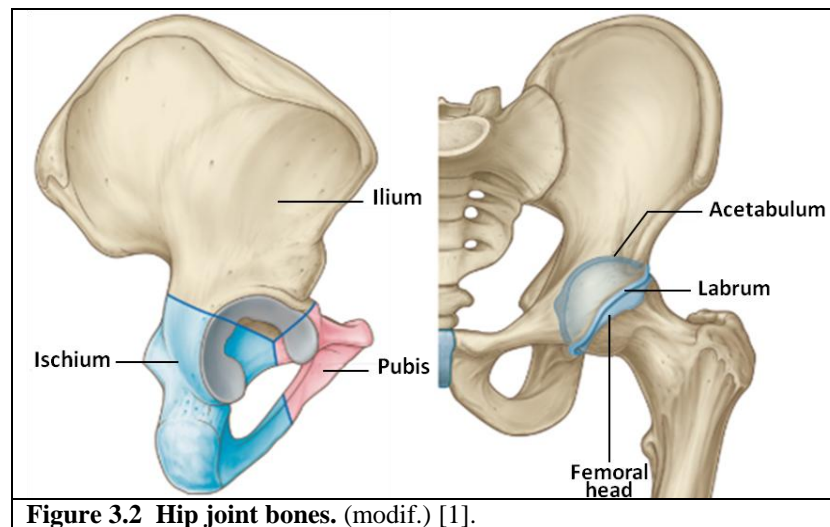
Figure 3.2 Hip joint bones. (modif.) [1].

3.2.2 Proximal Femur

The femur is the proximal segment of the lower limb. It is the longest, strongest and most voluminous bone of the body. When the body is in the upright position, the femur is directed obliquely downward and inward, so that the femurs are separated at the proximal end by the pelvis and are much closer together at the distal end. The obliquity is more pronounced in women than in men, depending on the conformation of the pelvis.

The posterior surface of the femur forms a concave arc and the femur has a slight twist in the vertical axis, which makes the transverse plane of its upper end not completely parallel to the transverse plane of the lower end. The proximal femur is the part of the femur, which articulates with the pelvis. It is formed by the femoral head, which allows the mobilization of bone, the greater and lesser trochanters, where the muscles and ligaments are inserted and the femoral neck which serves as a bridge between the trochanters and the femoral head as Figure 3.3 illustrates [1, 2, 5, 6, 64-66, 68].

Figure 3.3 Proximal femur anatomy. (modif.) [1].
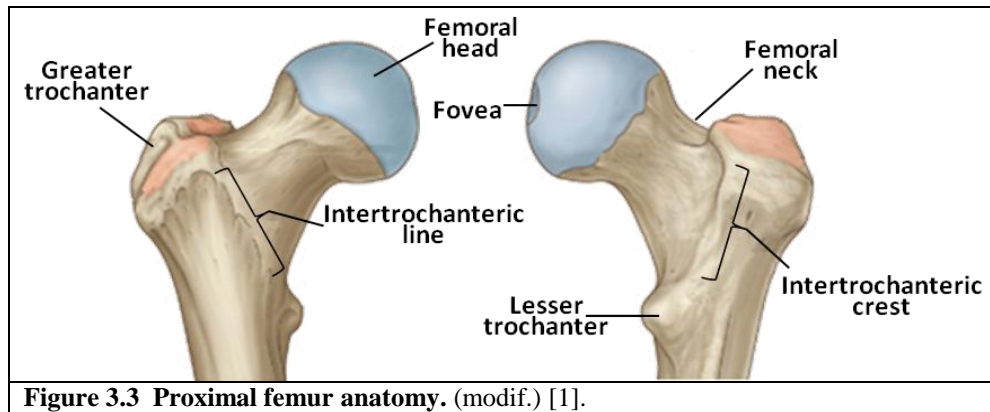
Femoral Head

The head of the femur has the approximate shape of two-thirds of a sphere and is the convex component of the ball-socket configuration of the hip. The surface is covered by hyaline cartilage, except for a small supra-lateral area next to the neck and the fovea, which is located below and behind the centre of the femoral head and provides the insertion point for the ligamentum teres. In a normal hip, the centre of the femoral head coincides with the centre of the acetabulum. The femoral head has an average diameter of 45.0 mm for females and 52.0 mm for males [1, 2, 5, 6, 64-68].

Femoral Neck

The neck of the femur is a cylindrical column of bone that connects the shaft with the head and is wider laterally than medially. The posterior surface is wide, concave and smooth while the anterior surface is tight and convex. The superior edge runs laterally from the femoral head to the greater trochanter. The axis of the neck is directed obliquely superiorly and antero-medially. The orientation of the neck relative to the shaft defines the range of movement of the hip joint [1, 2, 5, 6, 64-66, 68].

Greater and Lesser Trochanters

The trochanters provide attachment points for the muscles crossing the hip joint. The greater trochanter is a cuboid bone structure located laterally and below the femoral head. The lesser trochanter which is smaller than the greater trochanter, is located in the back and lower neck and has a conical shape, as Figures 3.3 and 3.4 show [1, 2, 5, 6, 64-66, 68].

39
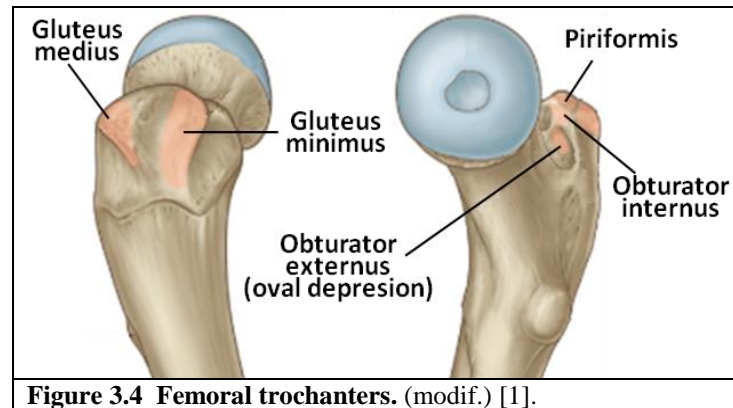
Figure 3.4 Femoral trochanters. (modif.) [1].

3.2.3 Cartilaginous Tissue

The articular cartilage allows the bones movement against each other without damage and pain as long as it remains slippery due to the fluid within the synovial membrane. Unlike bone, cartilage has a poor potential for healing, in the case of joints, any damage can lead to osteoarthritis.

Figure 3.5 illustrates that while the femoral head is totally covered by cartilage, the acetabular cartilage is a crescent-shaped tissue with a central depression named fossa that provides the insertion area for the teres ligament to connect both bones of the hip. The acetabulum is also surrounded by a rim of fibrocartilage known as labrum which avoids the loss of intracapsular fluid and it also provides greater depth to the acetabulum which hinders the potential slip of the femoral head out of place [1, 2, 5, 6, 68] .
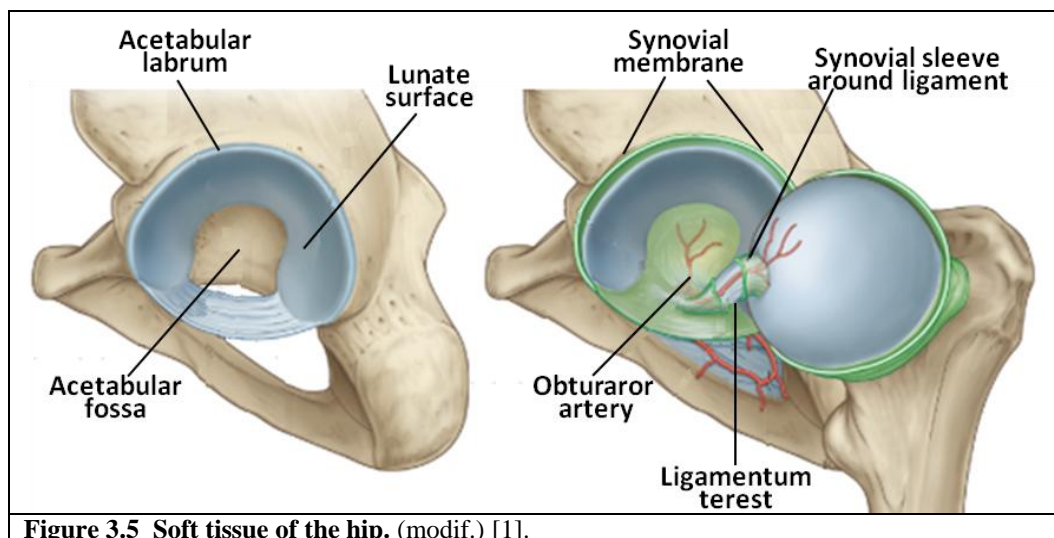
Figure 3.5 Soft tissue of the hip. (modif.) [1].

3.2.4 Ligaments of the Hip

The hip joint is fairly stable and has a wide range of motion as a result of the ball and socket configuration and the support provided by the ligaments. These ligaments are the iliofemoral, pubofemoral and ischiofemoral ligaments and are known as capsular ligaments since they are part of the joint capsule that surrounds synovial joints, as is shown in Figures 3.6a and 3.6b. In addition to capsular ligaments, there is the ligament teres which is located inside of the joint and connects the fovea in the femoral head with the acetabular notch.

| a | b |

Figure 3.6 Ligaments of the hip. (a) Iliofemoral and pubofemoral ligaments (Anterior view); (b) Ischiofemoral ligament (Posterior view). (modif.) [1].
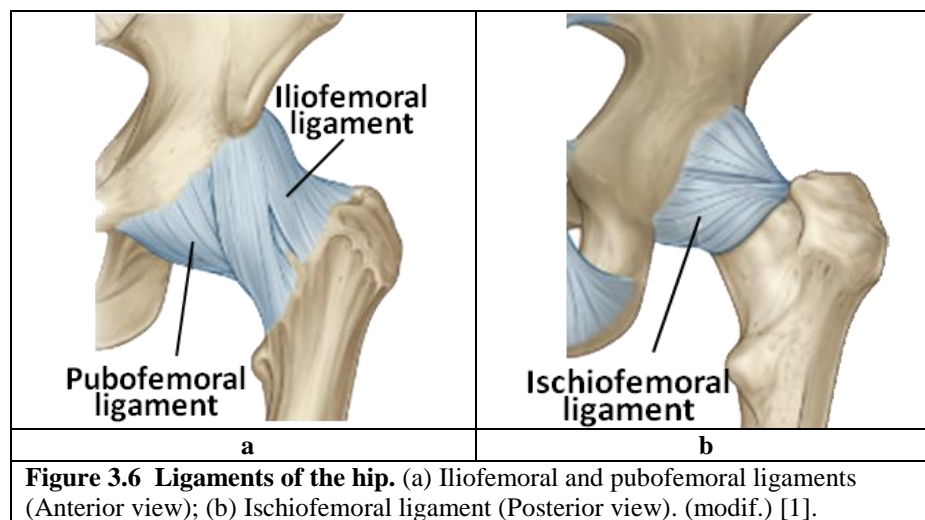
3.3 Bone Tissue

The osseous tissue is a dynamic-connective supporting tissue characterized by its complex structure and its capability to modify its structure and shape according to its location and the load demand within the skeleton. It has a large capacity for energy storage due to the porous structure of the trabecular bone.

At a first glance, the structure and composition of bone seems to be the same in all bones. However, on deeper examination, bone turns out to be a heterogeneous tissue, with composition and structure varying according to the body site, function, age and sex of the subject. Despite this heterogeneity, the components are the same in all bones.

In addition to the normal function of protection, support and locomotion, bones are the storehouse for minerals and bone matrix proteins. Bone tissue is continuously

remodelled and is considered a dynamic tissue that has excellent ability to repair itself and can alter its properties and configurations in response to mechanical demand [57-61].

Bone tissue can be considered a two-phase material. It is made up of an inorganic phase formed by mineral components, which represents 75% of the bone mass and an organic matrix, in which the collagen cells are dispersed, that constitutes the other 25% of the total bone mass.

As a consequence of the mixture of its component parts, bone has elastic properties. The inorganic component is mainly calcium phosphate crystals (hydroxyapatite), citrate ions and bicarbonate ions which contribute to the hardness and rigidity of the bone.

The organic matrix mainly consists of type-1 collagen fibres which account for over 90% of the whole organic substance and provide tensile strength to the bone. The remaining 10% corresponds to nanocollagenous components such as proteins, proteoglycans, phospholipids, glycoproteins and phosphoproteins [57-59, 61].

Collagen fibres are the structures that resist tensile forces in bone. They are formed by molecules made up of three polypeptide chains arranged in a helical configuration.

There are four cells involved during the development of bone tissue: osteoprogenitor cells, osteoblast, osteocytes and osteoclasts. Figure 3.7 shows the main micro structures that make up bone tissue as well as their spatial arrangement [57, 59, 61, 69].

Figure 3.7 Bone cells. (modif.) [58].
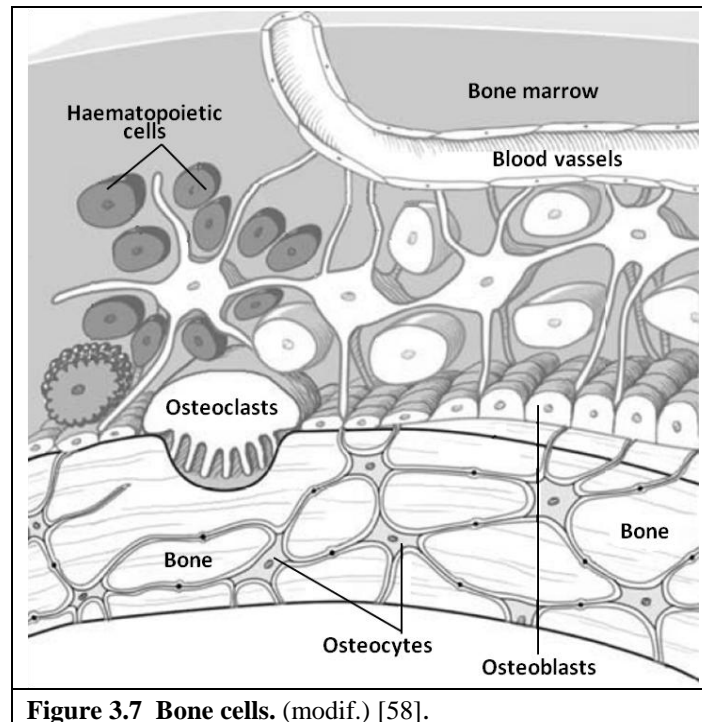
3.3.1 Types of Bone Tissue

Bone, as a tissue, consists of two histological types: non-lamellar and lamellar. Non-lamellar bone also known as "coarse fibred", "woven" or "immature bone" is characterized by the presence of collagen fibres in a quasi-random orientation. This tissue can be found in the bones of foetuses and young children and also at the beginning of the fracture healing process. The other type of bone tissue is known as lamellar or mature bone, in which the collagen fibres are organized in parallel layers or sheets (lamella).

Bones are not completely solid, having small gaps in their structure, forming small channels where the blood vessels run and fulfill their function of nutrient exchange. Macroscopically, bone tissue is classified into cortical (or compact) bone and trabecular (cancellous or spongy) bone. The basic structures of cortical and trabecular bones are osteons and trabecuale respectively, as illustrated in Figure 3.8. Both types of tissue are found in most bones.
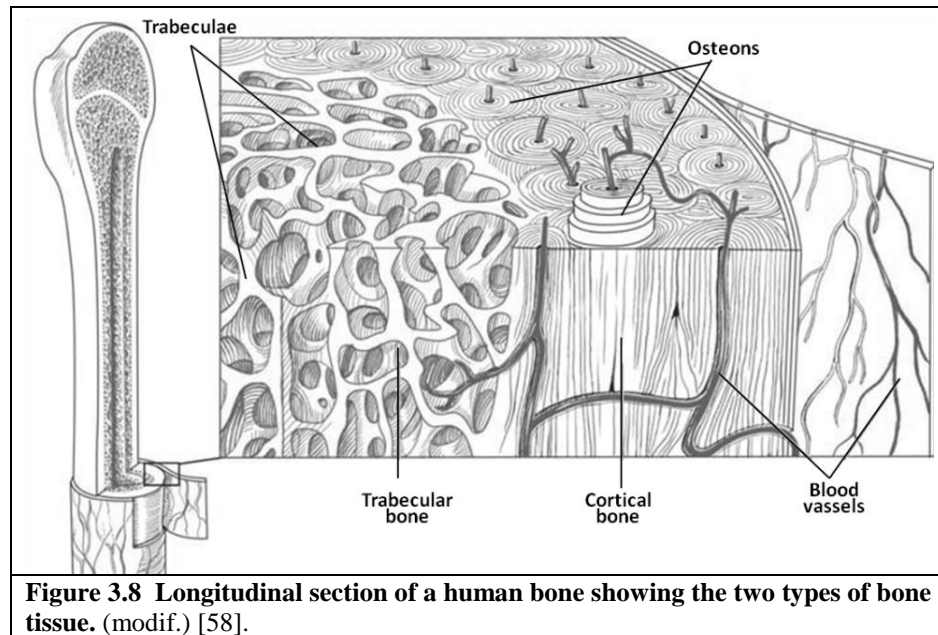
Figure 3.8 Longitudinal section of a human bone showing the two types of bone tissue. (modif.) [58].

3.3.2 Cortical or Compact Bone

Cortical bone makes up 80% of the skeleton and has few spaces between its hard components. It forms the outer layer of all bones and the majority of long bone shafts. Cortical bone withstands the stresses produced by the upright posture and movement in general [70].

In the first level of the hierarchical structure there are two different material distributions. The first is woven bone which is less organized bone tissue; it forms around a framework of collagen fibres and is eventually replaced by mature bone. The second is the osteonal cortical bone tissue, which includes central blood vessels, known as Haversian canal, and osteons, which are bone tubes surrounding the canal. The primary osteons are formed by the mineralization of cartilage while the secondary osteons are formed by replacement of existing bone as a result of remodelling [69, 71, 72].

In the second level structure of cortical bone it is the lamellae which make up the osteons. These entities are layers of bone, surrounding the Haversian canal. The lacunae (the ellipsoidal holes within the bone matrix), which contain the canaliculae and osteocytes are also found in the osteons. Caniculae appear during bone remodelling and are the tunnels that connect the lacunae and the cement lines. The

hierarchical structures of lamellar and osteonal bones are illustrated in Figure 3.9 [69, 71, 72].

Figure 3.9 Typical cortical bone structures (lamellar and osteonal bone). (modif.) [4].
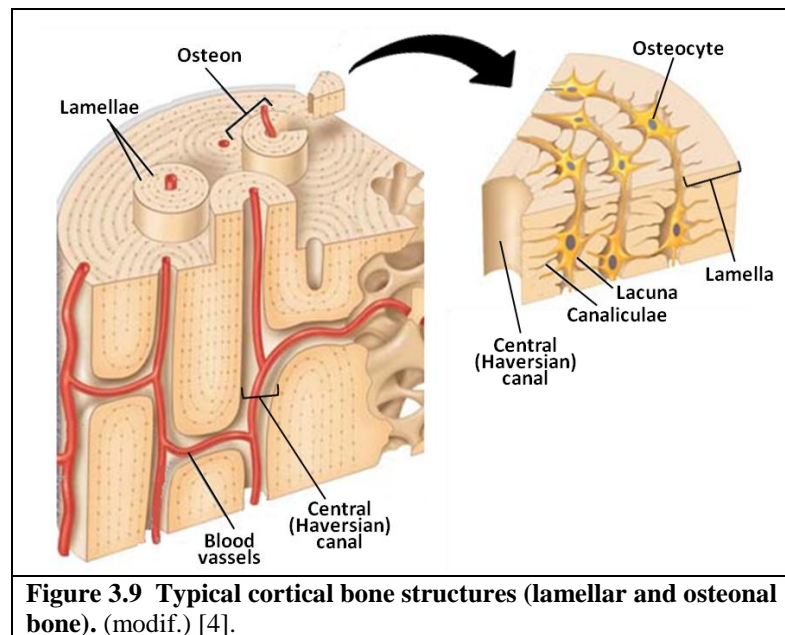
3.3.3 Trabecular or Cancellous Bone

Trabecular bone represents 20% of the mass of the skeleton but occupies a larger volume than cortical bone. This type of tissue is found primarily at the ends of long bones as well as in the vertebrae. However, all bones contain some proportion of this tissue. Trabecular bone helps in the dissipation and distribution of energy from the loads on the joints during daily activities.

The main difference between cortical and trabecular bone appears at the first structural level trabecular bone is much more porous than cortical bone, as is illustrated in Figure 3.10. At this level, the basic structural entity is the trabecula, which is a rod-like element that contains collagen fibres arranged in parallel lamellae. Trabeculae are oriented precisely along load lines, a feature that allows them to resist and transfer loads without breaking. Blood vessels are not found in trabecuale.

The second hierarchical structure of trabecular bone contains similar entities to cortical bone but with different size and arrangement as lamellae are not arranged concentrically [61, 69, 71, 72].

Figure 3.10 Typical trabecular bone structures. (modif.) [4].
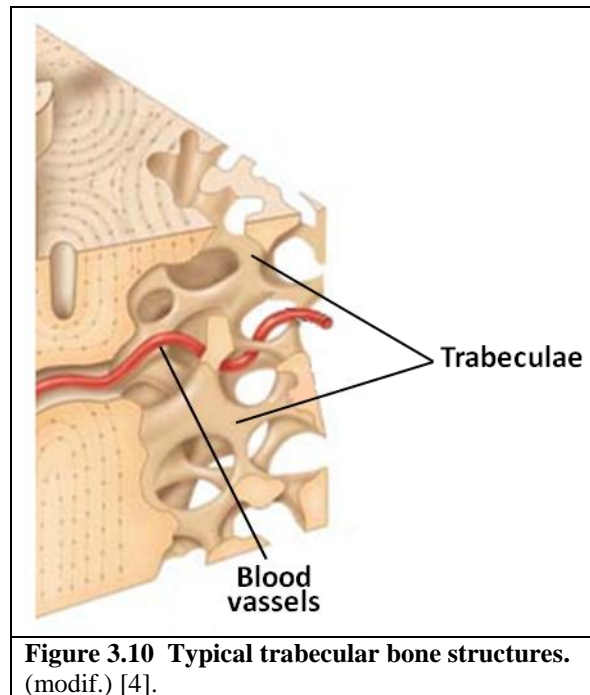
Trabecular Systems

Trabecular systems are the anatomical basis of trabecular bone; formed by the trabeculae where the loads are dissipated in order to distribute, absorb or transmit them. Trabecular systems of each bone generally continue their interaction with dissipating the loads through joints.

Two trabecular systems are present in the hip joint, both having as their origin the pelvic bone and going through the acetabulum to continue in the femoral head and neck. The lateral system, also known as the tension system, begins on the upper part of the auricular surface of the pelvis, converges at the sciatic notch, changes direction and goes toward the acetabulum where the trabeculae becomes continuous with the trabeculae from the inferior cortical zone in the femoral head, and finally finishes on the lateral femoral diaphysis. The second system is the medial, also known as the compressive system; initiating on the lower auricular surface, the trabeculae go through the proximal part of the acetabulum to become continuous with the trabeculae in the superior zone of the femoral head and finish on the medial internal cortical surface of the diaphysis. Figure 3.11a shows the location of the trabecular systems in the hip joint.

The configuration of these systems is modified in response to compressive loads in the joint, so if the direction of stresses changes, systems are remodelled to align with the patterns of stress. Figure 3.11b shows the appearance of trabecular systems when there is a morphological abnormality in the femoral proximal epiphysis and consequently a different distribution of loads [5, 73].

Figure 3.11 Trabecular system of the hip. (a) Pelvic system continues with femoral system; (b) Trabecular systems for abnormal femoral epiphysis. (modif.) [5].
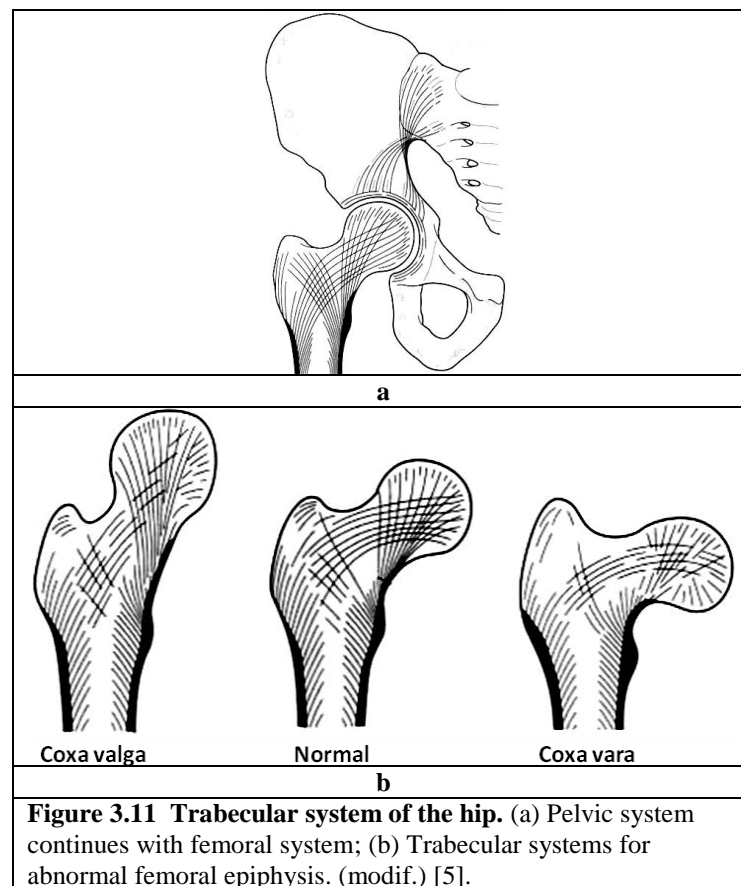
3.3.4 Mechanical Behaviour of Bone

Bone, as a physical entity, is subject to the laws of physics and mechanics that enable an understanding of its behaviour under external loads. There are significant differences in the mechanical properties of the cortical and trabecular bone. Cortical bone is stiffer than trabecular bone, supporting higher stresses but exhibiting lower strain before failure [5, 57, 61, 66, 69, 74, 75].

The mechanical properties of bone depend on the type of load applied in relation to the orientation of the trabecular systems, whereas, the properties of trabecular bone are also determined by extra factors such as density, location and function. Unlike

inert materials, biological materials such as bone can alter their mechanical properties, shape, and size under appropriate stimuli. In a physiological environment, bone tissue is subjected to continuous loading, which is essential to maintain the equilibrium in the complex formation-resorption process [5, 57, 61, 66, 69, 74, 75].

Bone is an anisotropic material because it exhibits a different response according to the loading axes, so that, bone behaviour is different when it is loaded in the longitudinal direction or in the transversal direction. In addition, its mechanical behaviour also depends on geometry, loading rates, loading modes and frequency of loading [5, 57, 61, 66, 69, 74-82].

Loads in Bones

In the vertebrates, bone is rarely loaded in a single mode during body motions. Loading of bone in vivo is complex for two principal reasons: bones are constantly subjected to multiple indeterminate loads, and their geometric structure is irregular.

Forces and moments can be applied to a structure in various directions, producing tension, compression, bending, shear and torsion, as shown in Figure 3.12.

Tension. In this mode of loading, forces of the same magnitude and opposite direction are applied outward from the surface of the structure. Tensile loading produces an elongation of the structure and the higher tensile stresses are located in a perpendicular plane to the loading application. In bones, tensile failures are a result of the detachment between the osteons and are usually seen in bones with a large proportion of trabecular bone. Pure tensile fractures are commonly found in the ligament insertion zones.

Compression. During compressive loading, a pair of equal and opposite forces is applied toward the surface of the structure, leading to a shortening in the material. As in the tension mode, the highest stresses during compression are located on a plane perpendicular to the applied loads. In cortical bone, failure under this kind of loading is mainly through oblique cracking of osteons, whereas in the trabecular bone it is by the cracking of the trabecuale. Compression fractures are commonly found in the vertebrae, which are subjected to high compressive loads.

Shear. During this loading mode, anti-parallel loads are applied on the surface of the structure. Consequently, resultant shear stress and strain are located inside the structure. Whenever a structure is loaded under tension or compression, internal shear stresses are produced.

Bending. During bending, bone is subjected to mixed tension/compression loading by applying three or four forces to produce two equal moments. Tensile stresses and strains occur on one side of the bending axis, while compressive stresses and strains occur on the opposite side.

Torsion. This mode of loading is produced by applying a load in order to twist the bone about an axis, so that an inner moment is obtained. A bone loaded in torsion produces shear stresses distributed over its entire structure [5, 57, 66, 69, 74, 75, 83-85].
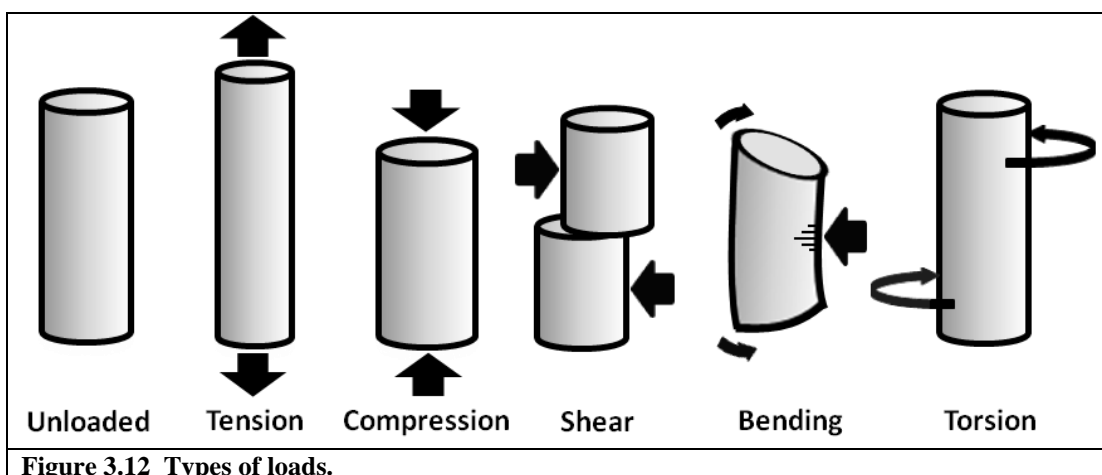
Figure 3.12 Types of loads.

Rate of Loading and Geometry

Bone biomechanical behaviour varies according to loading rate and geometry. If the bone is subjected to high rates of loading, it is stiffer when loads do not exceed the physiologic limits and is capable of storing more energy before fracture.

During fracture, accumulated energy is dissipated; when loading rate is low, this energy can produce a single crack, then the bone and soft tissues remain relatively intact, and there is little or no displacement of the bone fragments. In contrast, when the bone is under a high loading rate, energy cannot dissipate quickly enough to produce a single crack, resulting in bone crushing and a large amount of soft tissue

damage. Consequently, fractures are classified in three categories: low, high and very high energy.

Fractures in bone are a consequence of either a single load exceeding the ultimate strength of the bone or repetitive lower level loading known as fatigue fracture. The fatigue process depends on the load, the number of repetitions and the frequency of loading [5, 57, 61, 66, 69, 74-81, 84-86].

Vitro studies have shown that fracture in trabecular bone occurs when the strain exceeds 75%, but cortical bone fractures when the strain exceeds 2%. The porous structure of trabecular bone leads to a high capacity for energy storage [66].

Geometry has a great impact on the mechanical behaviour of the bone. During tensile and compressive loading the cross-sectional area of the bone governs the behaviour, with the bone being stronger and stiffer with the larger area. In bending, the mechanical behaviour of the bone is influenced by the moment of inertia, which is the mathematical entity that takes into account the distribution of tissue around the neutral axis and the cross-sectional area. Bone is stronger and stiffer when it has a large moment of inertia [66, 84, 85, 87].

Because of their length and tubular structure, long bones such as the femur are subjected to high bending moments in all directions during daily activities and also have a large moment of inertia because a substantial amount of tissue is distributed away from the neutral axis [66, 84, 85, 87].

3.3.5 Material Properties of Bone

Bone tissue is a highly vascular tissue which has the ability to repair itself and modify its material properties according to mechanical demand. Bone tissue can be considered as a two-phase material, formed by a strong and brittle material and a softer and more flexible material. The most important material properties of bone are strength and stiffness, which are determined by the material parameters and the anatomical structure.

As material parameters, strength and stiffness of the bone, are determined by the material composition, bonding between components and microscopic arrangement, whereas as structural parameters, strength and stiffness depend on the bone geometry and anatomic location.

Bone is an anisotropic material; therefore strength and stiffness vary depending on the orientation and the type of loading to which it is subjected to. Regarding the orientation, bone is stronger when the loading is applied longitudinally than transversally, whereas, in terms of the loading conditions, bone supports higher loads when it is subjected to compressive loading than in tensile conditions. Additionally, bone presents a ductile-to-brittle transition depending on the strain rate as is illustrated in Figure 3.13 [5, 57, 61, 66, 69, 74-82, 88, 89].

Figure 3.13 Ductile-to-brittle transition of bone at different loading rates. (modif.) [89]
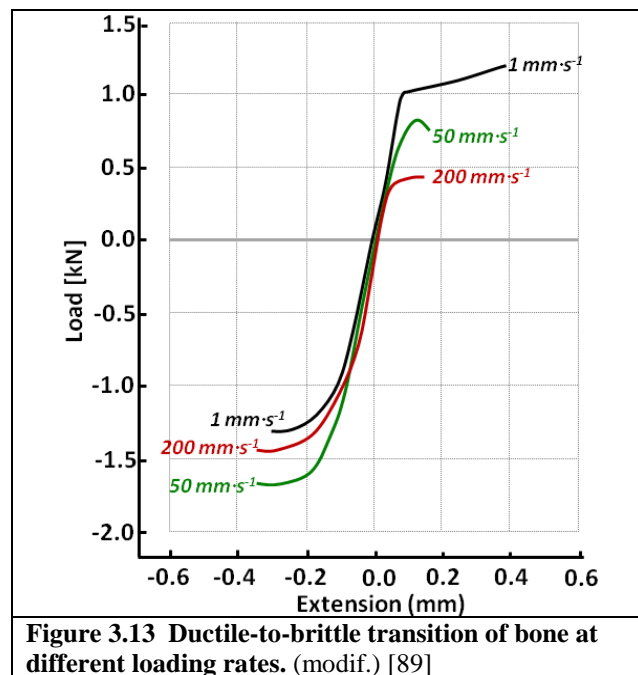
The strength of a quasi-brittle material is the ultimate stress that a material can support before it weakens or fails (σ_u). Stiffness represents how elastic a material is and can be measured by calculating the elastic modulus of the material, which is the slope of elastic region in the stress-strain curve of the material.

The stress-strain curve shows the behaviour of a material when it is subjected to different loading conditions. Stresses (σ) are the internal forces resulting from the

application of load (F) acting to deform a structure on a determined cross-sectional area (A).

$$\sigma = \frac{F}{A} \tag{1}$$

Strain (ε) is the deformation suffered by the material when stress is produced and is expressed as the change in the length (ΔL) per unit initial length (L_i).

$$\varepsilon = \frac{\Delta L}{L} \tag{2}$$

Figure 3.14 shows a characteristic stress-strain curve of bone. The initial segment of the curve (straight line) indicates the elastic region and depends on the stiffness of the bone. The slope of this portion of the curve is known as the elastic modulus of the material. At this stage, the deformation is temporary and is maintained only while the load is applied, after loading is removed, the material regains its original shape. The transition from the elastic to plastic behaviour is determined by the yield point and the value of the stress at this point is known as yield stress (σ_y).

The second section (curved) shows the plastic region, where the material, although it recovers partially, is permanently deformed. This phase is known as the elastic-continuum damage mechanism (CDM). In this section the material absorbs energy by developing micro fractures but remains an integrated structure. In the event of a further increment of the loading the material reaches the ultimate stress (σ_u). At this point the bone behaviour goes into the failure mechanism (FM) region, where the fracture of the material occurs. CDM and FM phases vary depending on the type of bone, either cortical or trabecular, capacity of energy absorption, strain rate, specimen geometry and type of loading [5, 57, 61, 66, 69, 74-82, 88, 89].

CDM →*Continuum Damage Mechanism.*
FM → *Failure Mechanism*
Figure 3.14 Stress-strain curve of bone. (modif.)[88].
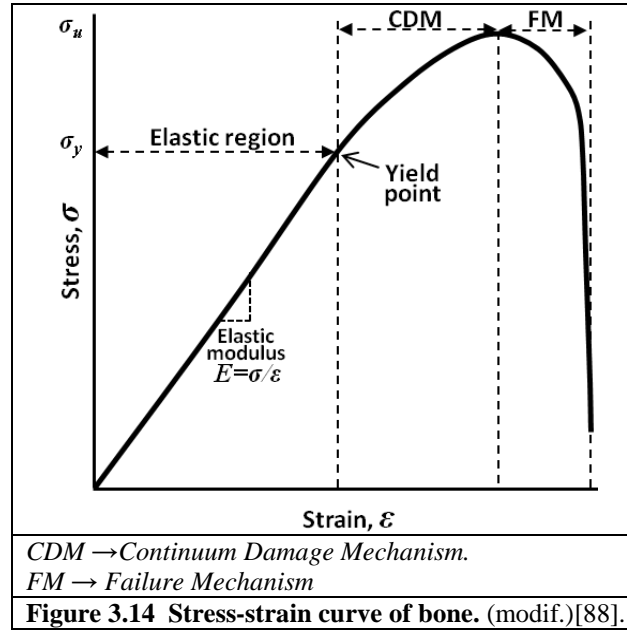
Whole bone is considered to be a quasi-brittle material; however each type of bone exhibits particular stress-strain behaviour. Figures 3.15 shows the stress-strain curves of cortical bone under tensile and compressive loading. It can be clearly appreciated that cortical bone supports much greater stresses under compression than in tension. The compression curve exhibits an elastic region from the origin to the yield point (A-B_C). Due to its brittle condition, the CDM region in cortical bone practically does not exist (B_C-C_C), as the stresses supported after passing the yield stress and before failure are minimal. However, this ultimate compressive stress (C_C) represents the start of FM in the structure before starting to show some resistance against the loading (D_C). At this point, fracture propagation continues in the cortical bone before a complete fracture occurs (E_C). The strain when FM starts under compression is known as the crushing strain. Fractures in compression are commonly comminuted fractures which are those in which the bone is splintered or crushed [5, 57, 61, 66, 69, 74-82, 85].

The tensile curve presents an elastic behaviour rising to its yield point at about half of the value of that under compression (A-B_T); however, the plastic region suggests a greater deformation before fracture (B_T-C_T). This plastic behaviour is a consequence of the organic components of the bone, which provide the bone with some ductility before complete failure. Unlike the compressive behaviour, when cortical bone

reaches its ultimate tensile strength (C_T), the failure is instantaneous and the material is split into two or more sections [5, 57, 61, 66, 69, 74-82, 85].

Figure 3.15 Stress-strain curves of cortical bone. (modif.) [66, 82].
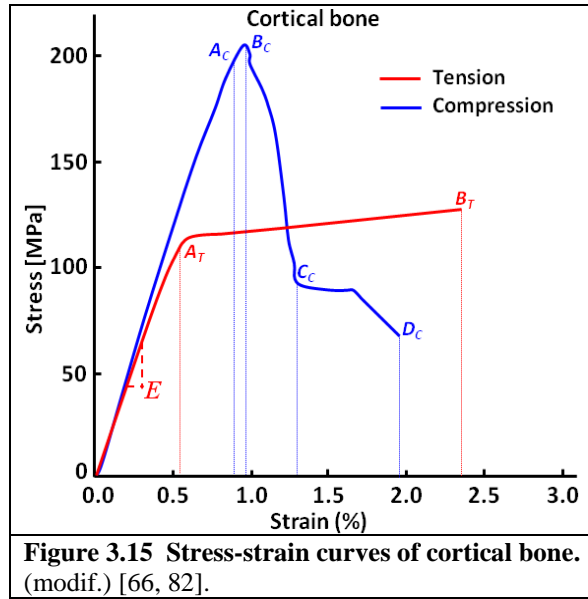
Figures 3.16 shows the stress-strain curves of the trabecular bone under tensile and compressive loading. It can be seen that as with the cortical, the trabecular bone supports greater stresses under compression (C_C) than in tension (C_T), however the values are much lower than the stresses supported by cortical bone. The compression curve exhibits an elastic region from the origin to the yield point (A-B_C). Then, the CDM phase appears (B_C-C_C) and the FM starts once the trabecular bone reaches its ultimate compressive stress (B_C), where micro fractures starts to occur; however, due to its highly porous structure, FM in trabecular bone exhibits a large crushing strain before complete fracture (C_C-D_C) [5, 57, 61, 66, 69, 74-82, 85].

The tensile curve exhibits a similar behaviour to that in compressive, having an elastic region from the origin to the yield point (A-B_T) following by a CDM region from the yield point to its ultimate tensile stress (B_T-C_T). However, after the ultimate strength point, the FM starts with micro fractures in the trabeculae where the bone exhibits a ductile but irregular behaviour due to the inconsistent cracking propagation in its porous structure (C_T-D_T). The strain under tension after ultimate stress is known as cracking strain. Final fracture in tension occurs at a lower magnitude of stress than under compression (E_T) [5, 57, 61, 66, 69, 74-82, 85].

Figure 3.16 Stress-strain curves of trabecular bone. (modif.) [66, 82].
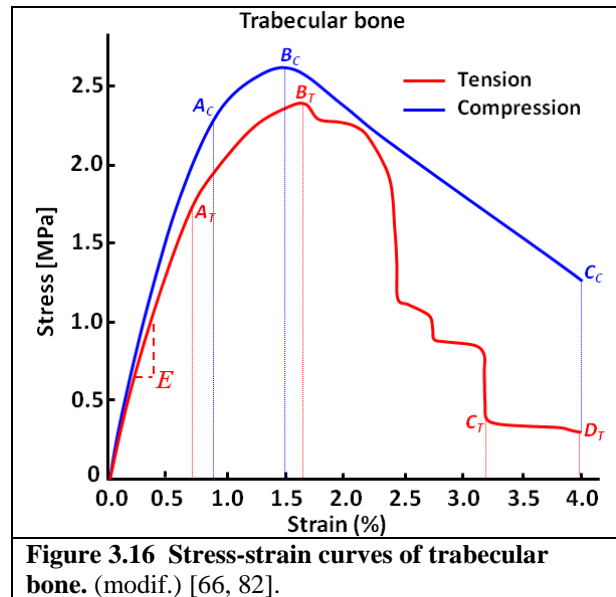
3.4 Cartilaginous Tissue

Cartilage is a connective tissue with very well defined functions. It performs a significant role in human body development. In the human embryo, it forms a primitive skeleton. This specialized tissue is fibrous and dense, does not contain blood vessels and uses the extracellular matrix for nutrient transport. Cartilage is found throughout the body, principally in the joints and spine but also located in the ears, throat and nose.

Cartilage has an inhomogeneous distribution of collagen fibrils and is divided into three zones, as shown in Figure 3.17. The superficial tangential zone contains layers of high density collagen fibres parallel to the articular surface; in the middle zone the fibres are widely spaced and finally, the deep zone contains larger collagen fibres radially oriented and mixed with the calcified cartilage. Depending on the type of cartilage, various amounts of collagen and elastin fibres are embedded in the matrix causing the cartilage to be either flexible or very strong and resistant [6, 69, 74, 75, 90, 91].
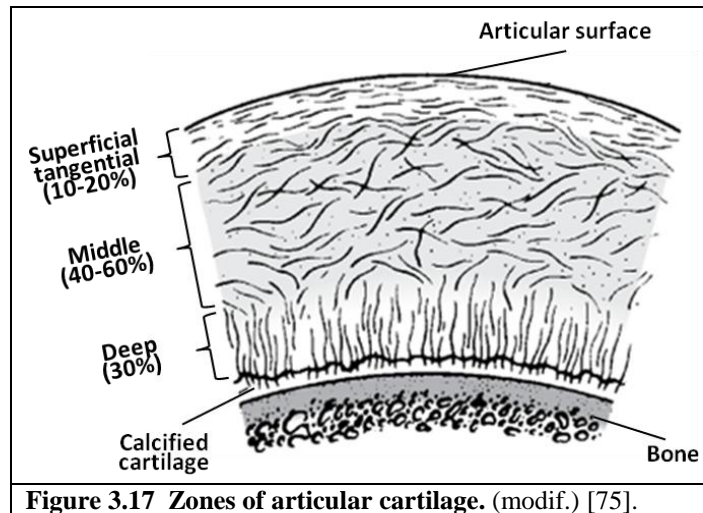
Figure 3.17 Zones of articular cartilage. (modif.) [75].

3.4.1 Types of Cartilaginous Tissue

The three types of cartilage found in the body are:

Hyaline cartilage. When the fetus is developing in the womb the entire skeletal system is made of hyaline cartilage and is visible after the first 3 months of pregnancy. Most of this hyaline cartilage is gradually replaced by bone over the next 6 months by the ossification process. However, some of it remains as a covering on the surfaces of the bones at joints, where it is known as articular cartilage. In the human body, the costal cartilages that attach the anterior ends of the upper seven pair of ribs to the sternum are hyaline cartilage.

Hyaline cartilage is a biphasic material; the fluid phase is a mixture of water and electrolytes while the solid phase is formed from chondrocytes and collagen. Water is the largest volume component within the structure of the cartilage. In normal cartilage 30% of all water resides within the intrafibrillar space of collagen, and, for normal tissue, this amount does not vary with age. This multiphasic system allows fluid flow and determines the cartilage compressive viscoelastic behaviour. The main functions of hyaline cartilage are to distribute joint loads over a large area and to allow relative movement of the joint surfaces with minimal friction and wear [4, 6, 61, 69, 75, 90, 92].

Fibrocartilage. This type of cartilage is dense and very resistant to stretching. The intervertebral disks that surround the spinal cord and act as shock absorbers between

the vertebrae are made of this strong cartilage. It also connects the pelvic bones at the pubic symphysis.

Elastic cartilage. This cartilage has a predominance of elastin fibres embedded in the matrix. These fibres make this type of cartilage stretchy and flexible while being capable of returning to its original shape. Elastic cartilage makes up the external ear or auricle and the ear canals [6, 61, 69, 75, 90-92].

3.4.2 Mechanical Behaviour of Articular Cartilage

The mechanical behaviour of articular cartilage depends on the type of loading to which it is subjected. Under compressive loads, performance of the cartilage depends on the flow of interstitial fluid, whereas, the movement of the collagen fibres determines the shear behaviour. Under tension, articular cartilage presents anisotropic properties because the collagen fibres are stronger and stiffer in the superficial areas [6, 61, 69, 75, 90, 92, 93].

3.4.3 Material Properties of Articular Cartilage

The main properties of articular cartilage are its ability to absorb and distribute the loads to which it is subjected during daily activities and its facilitation of smooth motion between articular surfaces by a very low coefficient of friction.

Articular cartilage is considered a viscoleastic composite material made up of a solid organic matrix formed by cells and collagen fibres, which provide the strength and stiffness, and an inorganic fluid matrix (water with salts and proteins). The inhomogeneous distribution of the collagen fibres is the main factor producing anisotropy [6, 61, 69, 75, 90, 92, 93].

Figure 3.18 shows an articular cartilage stress-strain curve (under tension) and the corresponding collagen fibre configuration. The first upwardly concave portion of the curve, called the toe region, is where the initial increment of force produces an alignment of the collagen fibres in the direction of the loading. The second portion of the curve represents the linear behaviour, where the fibres continue stretching to the point of failure [66, 74, 75, 94].
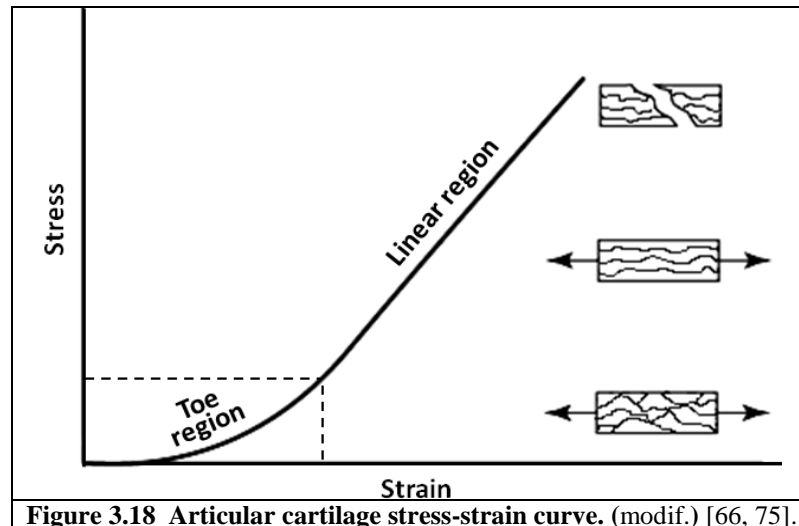
Figure 3.18 Articular cartilage stress-strain curve. (modif.) [66, 75].

3.5 Ligamentous Tissue

A ligament is a fibrous connective tissue which links bone to bone across the joints. In addition to attaching bones, ligaments provide mechanical stability and guide movement in the joints, maintaining the congruency and preventing excessive displacement. Ligaments are bands of elastin and collagen fibres arranged in a parallel assembly; they are poorly vascularised.

In synovial joints such as the hip, ligaments are known as capsular ligaments because they surround the articular capsule. The hip joint also includes an intra-capsular ligament which helps with the stability and allows a large range of motion [66, 75, 95].

3.5.1 Mechanical Behaviour of Ligaments

The structure of the ligaments varies between the insertion points and the mid-substance. They are mechanically stiffer near to the bones, where they reduce the stress concentrations and decrease the risk of tearing of the tissue at the interface with the bone. Ligaments are viscoelastic structures, flexible enough to allow the motion of the bones through the joints but strong enough to provide resistance to external forces and unusual motions. Ligaments modify their behaviour in response to the mechanical demand, so that the tensile strength increases when they are subjected to physical activities whereas it is reduced during immobilization.

3.5.2 Material Properties of Ligaments

Ligaments exhibit viscous and elastic behaviour when experiencing deformation. This viscoelastic nature leads to loading rate dependant behaviour. They contract under tensile loading and recover their original shape when tension is relieved, however they cannot preserve their original shape when the loading reaches the yield point or after long time deformations, for this reason, any joint dislocations have to be adjusted rapidly, otherwise ligaments will permanently elongated, predisposing the joint to future dislocations [66, 75, 95].

Figure 3.19 shows the typical stress-strain curve for ligaments. The initial toe region represents the alignment of the collagen and elastin fibres wherein large elongations occur with a small amount of loading. The second region represents the linear behaviour of the ligament where the fibres continue with their parallel orientation. The toe and linear regions fit within the physiologic loading. The third region starts when the loading exceeds the physiological loading, representing the beginning of microfailures (MF) of the ligament fibres which is indicated by the peaks and dips in the curve. Finally, the overloading and/or the range of motion out of the limits ends when complete failure occurs (CF) [75, 95].

MF →Microfailure
FM →Ccomplete Failure
Figure 3.19 Ligament stress-strain curve. (modif.) [75, 95].
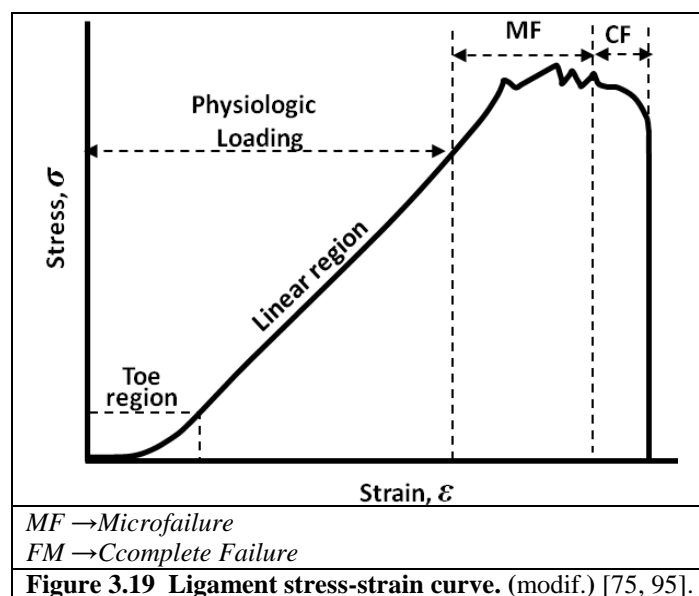
3.6 Biomechanics of the Hip

As well as being the largest joint in the human body, the hip has a wide range of motion and great stability due its socket-ball configuration. This structure is very important for the adequate performance of locomotion in vertebrates. Disorders or abnormalities of the hip could lead to a misallocation of stress in joint tissues and thus cause pathologies such as degenerative osteoarthritis.

3.6.1 Angular Relationships

There are two types of angular relationships; the first is related to the union between the acetabulum and femur. The second is related to the geometry of the femur itself.

The acetabular axis is directed laterally with antero-inferior direction to articulate with the femoral head where the axis runs medially with antero-superior direction because of the anteversion angle of the femoral neck. Thus, there is an angle of 30º to 40º between the axes of the femoral neck and acetabulum, as is illustrated in Figure 3.20a. Also, the superior part of the acetabulum covers laterally the femoral head due to an angle of 30º to 40º formed between the horizontal and the lateral-inferior inclination of the acetabulum.

Figure 3.20b shows the angle of Wiberg, which is about 30º and is formed by the intersection of a vertical imaginary line that runs through the centre of the femoral head and an oblique imaginary line formed by the centre of the femoral head to the bony margins of the acetabulum [2, 5, 62, 64, 66, 96].

a	b
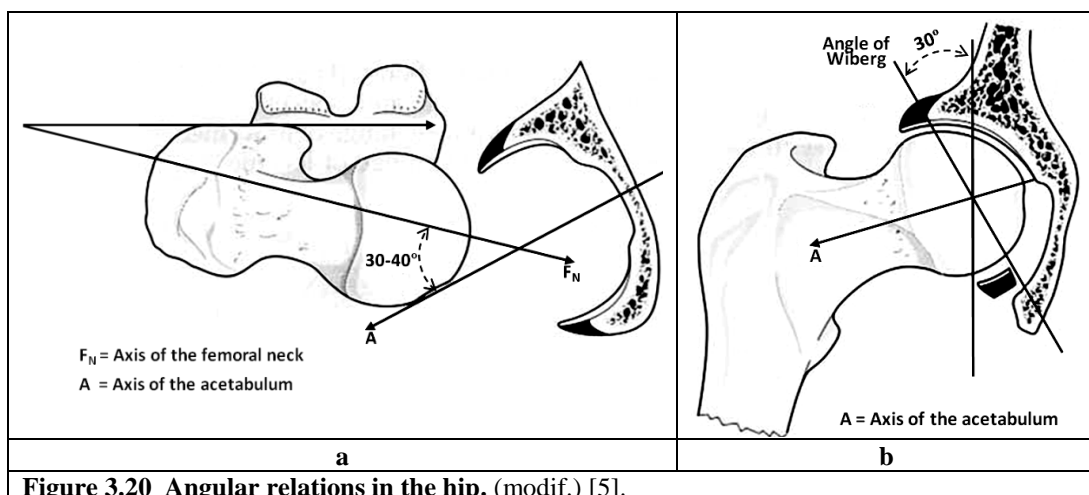
Figure 3.20 Angular relations in the hip. (modif.) [5].

The angle formed in the frontal plane between the femoral neck and the shaft of the femur is known as the neck-to-shaft angle. In newborns the neck-to-shaft angle is about 150º which decreases gradually with age until it reaches the adult value of 135º. If the neck-to-shaft angle is less than 135º the condition is known as *coxa vara* and if it exceeds 135º it is known as *coxa valga*, as illustrated in Figure 3.21. Since the trabecular system of the hip is a resultant system from the union of the systems from the pelvic bone and the femoral head, any deviations of the femoral neck alters the stress distribution in the hip as a consequence of the abnormal arrangement of the trabecular systems [2, 5, 62, 64, 66, 96].

Figure 3.21 Neck-to-shaft angle.
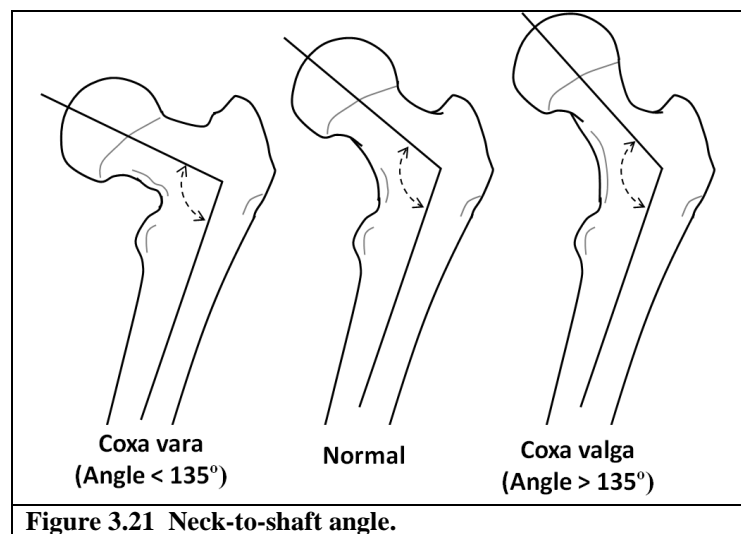
The angle of anteversion is formed by the projection of the longitudinal axis of the femoral neck and the transverse axis of the femoral condyles. This angle is directed medially and anteriorly and averages about 7.5º in adults, as shown in Figure 3.22.

If the angle of anteversion is larger than the average, a portion of the femoral head is uncovered which results in a tendency to internal rotation of the leg during gait in order to maintain the femoral head inside the acetabular cavity. If the anteversion angle is smaller, the hip joint has a propensity to rotate externally more easily than normal during the gait. This condition is known as retroverted hip [2, 5, 62, 64, 66, 96].

Figure 3.22 Anterversion angle of the femur. (modif.) [66].
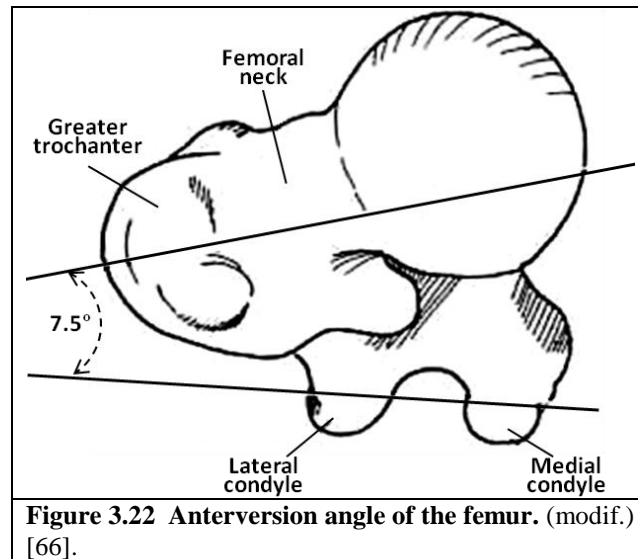
3.6.2 Axes of Movement

As mentioned above, the direction of the femoral neck to the horizontal plane and the frontal plane are very important for stability and movement of the hip. In addition to the angular relationships between the femoral head with the acetabulum and the femoral neck with the longitudinal axis, it is important to mention the axes of the femur about the vertical axis and the axes of rotation of the hip in which all movements are performed.

Femoral Axes

When the body is upright, there is a natural vertical axis from which the anatomical and mechanical axes of the femur may be located. The anatomical axis of the femur is the imaginary line that runs longitudinally from distal to proximal from the centre of the condyles and the greater trochanter, with an angle of approximately 6° from the vertical axis. The anatomical axis is also a reference to measure the inclination angle of the femoral neck. [2, 5, 62, 64, 66, 96]

The mechanical axis has the same origin as the anatomical axis but runs to the geometric centre of rotation of the femoral head with an angle of approximately 3° from the vertical axis as is shown in Figure 3.23.
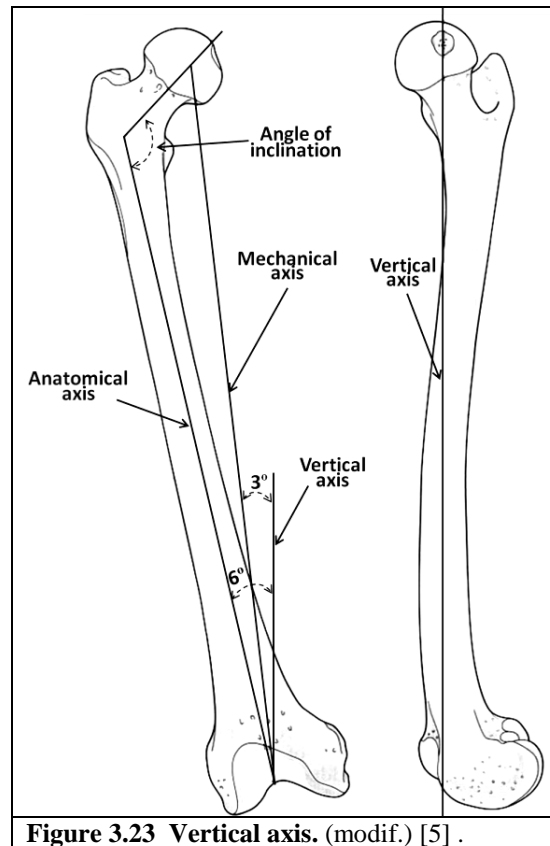
Figure 3.23 Vertical axis. (modif.) [5] .

Rotation Axes

The hip has three axes of rotation that intersect at the geometric centre of rotation of the femoral head, as shown in Figure 3.24. The three axes are related to different movements of the hip. The transverse axis is formed by a frontal plane and a horizontal plane and is the axis of flexion and extension; the sagittal axis is formed by a sagittal plane and a horizontal plane and is the axis for adduction and abduction movements; the vertical axis, which coincides with the longitudinal axis of the leg when the hip is in a neutral position, is formed by a sagittal plane and a frontal plane, and is the reference axis for internal and external rotation movements [2, 5, 62, 64, 66, 96].
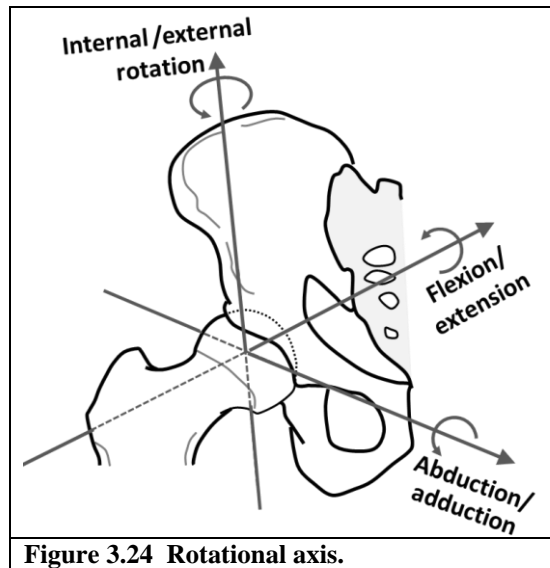
Figure 3.24 Rotational axis.

3.6.3 Centre of Rotation

The human hip is usually considered as a ball and socket joint, with the centre of rotation defined as the centre of the hip joint. The location of the centre of rotation of the hip joint is essential in reconstructive surgeries in order to find the optimal lever arm for the gluteus medius muscle [97-99].

Figure 3.25 shows the pelvic and femoral coordinate systems, and also the Joint Coordinate System (JCS) for the hip joint. In Table 3.1, a description of each of the points in the coordinate system is given.
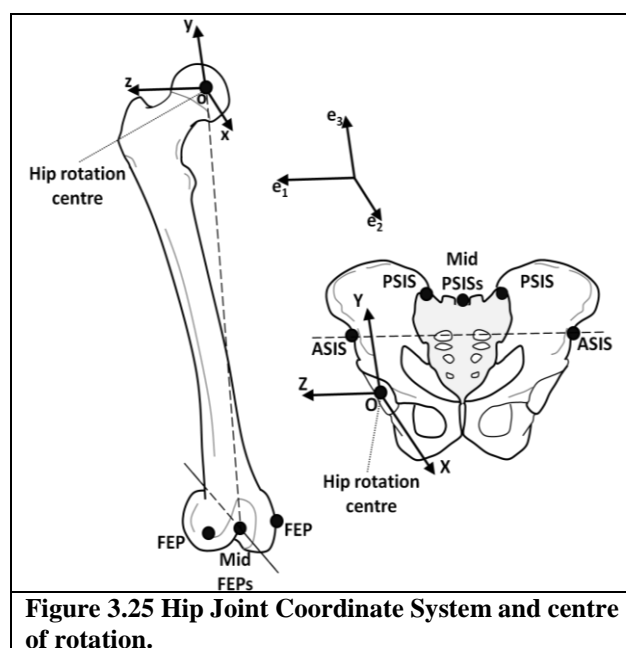
Figure 3.25 Hip Joint Coordinate System and centre of rotation.

Table 3.1 Joint Coordinate System.

Pelvic coordinate system (XYZ)		Femoral coordinate system (xyz)		Hip joint coordinate system $(e_1 e_2 e_3)$	
O	The origin coincident with the hip centre of rotation.	**o**	The origin coincident with the hip centre of rotation and coincident with the pelvic coordinate system (O) in the neutral configuration.		
Z	The line parallel to a line connecting the right and left ASISs, and pointing to the right.	**z**	The line perpendicular to the y-axis, lying in the plane defined by the origin and the two FEPs, pointing to the right.	**e₁**	The axis fixed to the pelvis and coincident with the Z-axis of the pelvic coordinate system. ***Rotation***: flexion/extension. ***Displacement***: mediolateral translation.
X	The line parallel to a line lying in the plane defined by the two ASISs and the midpoint of the two PSISs, orthogonal to the Z-axis, and pointing anteriorly.	**y**	The line joining the midpoint between the medial and lateral FEPs and the origin, and pointing cranially.	**e₂**	The floating axis, the common axis perpendicular to e_1 and e_3. ***Rotation***: adduction/abduction. ***Displacement***: antero-posterior translation.
Y	The line perpendicular to both X and Z, pointing cranially.	**x**	The line perpendicular to both y- and z-axis, pointing anteriorly.	**e₃**	The axis fixed to the femur and coincident with the y-axis of the femur coordinate system. ***Rotation***: internal/external rotation. ***Displacement***: proximo-distal translation.
Anatomical Landmarks		*ASIS: anterior superior iliac spine* *PSIS: posterior superior iliac spine* *FEP: femoral epicondyle*			
(Modif. from Wu, G., et al. 2002) [99].					

3.6.4 Hip Movements

Hip motion takes place in all the anatomical planes. The flexion-extension movement takes place in the sagittal plane; abduction-adduction takes place in the frontal plane, while internal-external rotation occurs in the transversal plane [2, 5, 62, 64, 66, 96].

Flexion/extension

Hip flexion is limited by the thigh contact with the abdominal wall, with a range of approximately 0º to 140º. In extension, the range of movement is much smaller, between 0º to 30º as is illustrated in Figure 3.26 [2, 5, 62, 64, 66, 96]

Figure 3.26 Flexion/extension movement. (modif.) [62].
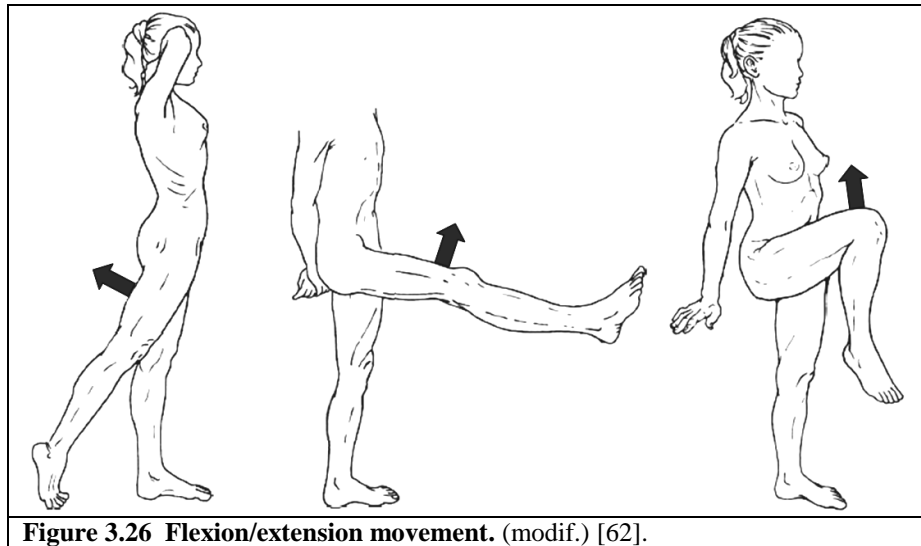
Adduction/Abduction

The range of abduction is normally from 0º to 30º when the body is in a neutral position, but when the hip is partially flexed the hip can reach about 90º of abduction. Adduction has a range of 0º to 25º, which is limited by contact with the opposite limb, as is illustrated in Figure 3.27 [2, 5, 62, 64, 66, 96].

Figure 3.27 Adduction/Abduction movement. (modif.) [62].
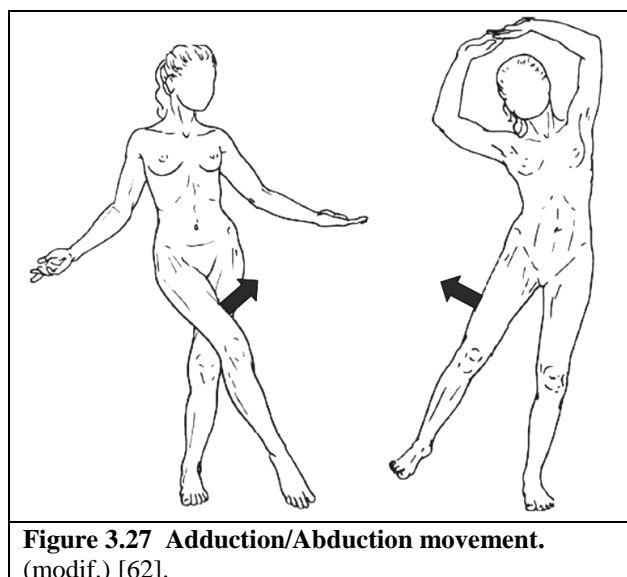
Rotation

With the hip in a neutral position, internal and external rotation involves moving the entire lower extremity, including the foot through about 50º, as shown in Figure 3.28. If the hip is flexed, the RoM increases, reaching 90º (60º external rotation and 30º internal rotation) [2, 5, 62, 64, 66, 96].
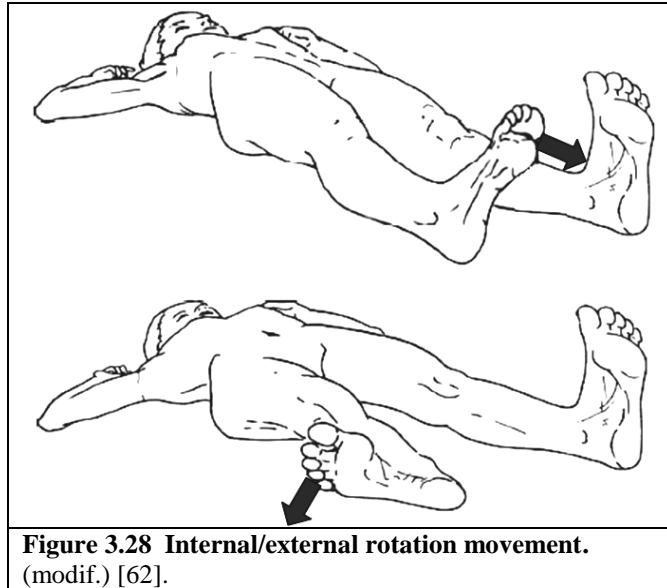
Figure 3.28 Internal/external rotation movement.
(modif.) [62].

CHAPTER IV: STRESS ANALYSIS FOLLOWING OSTEOCHONDROPLASTY

4.1 Introduction

Osteochondroplasty is the surgical procedure to repair both bony and cartilaginous structures in the joints. The surgical treatment of FAI often involves femoral osteochondroplasty. It focuses on improving the range of motion (RoM) of the hip by reducing the impact between the parts of the joint [3, 8, 10, 11, 14, 18, 19, 21, 25, 39, 46-48].

The removal of bone during osteochondroplasty increases the risk of fracture of the femoral neck after surgery because of the reduction of bone volume in an area of high importance for weight bearing in humans, and this risk increases further when the bone exhibits signs of osteoporosis [100-107].

The procedure may be undertaken via surgical hip dislocation [48], allowing 360º visualization of the hip with promising mid-term results [3, 8, 11, 18, 19, 21, 25, 50] or arthroscopically. The main drawback with arthroscopy stems from the poor visualization of the femoral neck, leading to osteochondroplasty of reduced effectiveness [3, 10, 14, 18, 19, 25, 46, 47, 49, 50].

The present Chapter describes the first finite element analysis performed with regards to femoral osteochondroplasty in the present Thesis. This analysis consists of the investigation of the relationship between depth of resection and femoral neck stress.

4.1.1 Finite Element Method (FEM)

The Finite Element Method (FEM) is a numerical procedure used to describe and obtain approximate solutions to complex engineering systems. This method has been widely employed in the stress analysis of solids and structures. However, FEM is useful in many other fields of engineering analysis such as heat transfer, electromagnetism and fluid flow.

FEM is employed for solving partial differential equations and its application results in a set of simultaneous equations that describe the structure and properties of a physical system. In this method, the geometry of the object or system to be analyzed is divided into a finite number of pieces known as elements that are connected by nodes. The morphological arrangement of elements and nodes defines the geometry using a grid known as the mesh, where the material and structural properties are defined. Consequently, many simultaneous equations result from this process and the use of computer systems to perform the analysis is essential [108-111].

The practical application of FEM is known as Finite Element Analysis (FEA). It was developed by the aircraft industry in the mid-1950s to perform airframe and structural analysis. During the next two decades, the development of computer systems continued with improvements in calculation time and the construction of more complex geometries and the analysis was extended to non-structural fields such as fluid mechanics and heat conduction. In 1972, as a result of concern about load-bearing in bones and the relationship with bone architecture, Brekelmans *et al*., introduced the application of FEA to biomechanics by analyzing the mechanical behaviour of bone under loading conditions [108-117].

FEA has continued to improve and applications have been expanded to include other areas of science. FEA development in the area of bioengineering has increased because of the improvement in obtaining complex geometries from living tissues via the development of specialized software to import data from image systems such as plane X-rays, computed tomography scans (CT scans), and magnetic resonance imaging (MRI).

The analysis in the present research has been undertaken using Abaqus/Standard for static stress analysis. The characteristics of this analysis are the following:

- It is used for three dimensional modelling.
- It can solve linear and non-linear problems.
  - Nonlinearities occurring from material non-linear behaviour, large-displacements, and boundary nonlinearities such as contacts and friction between surfaces can be handled.

- Material behaviour can be defined as linear or non-linear.
- It ignores time-dependent material behaviour.
- It considers the rate-dependent plasticity of the material.
- Inertia effects can be ignored.

For static stress analysis, the Abaqus/Standard finite element software package determines approximate solutions to the equilibrium equations taking into account the relevant constitutive and geometric relationships

The basis to solve a finite element analysis is set down by the Hooke's Law:
$$\boldsymbol{F = kx} \tag{3}$$
Where F is the force, k is a proportional constant and x is the displacement.

Since each element has several nodes and each node has an associate displacement, the same number of equations as nodes in the model has to be created. The resultant simultaneous equations are expressed as:
$$\boldsymbol{\{F\} = [K]\,\{u\}} \tag{4}$$
Where $[F]$ is the force matrix, $\{K\}$ is the stiffness matrix and $\{u\}$ is the displacement matrix.

Hooke's Law can relate the stress and strain parameters on an analysis as:
$$\boldsymbol{\sigma = E\varepsilon} \tag{5}$$
Where σ is the stress, E is the Young's modulus and ε is the strain.

Newton's method is used by Abaqus/Standard to solve the resulting nonlinear equilibrium equations, with the solution being obtained using a series of increments with iterations to obtain equilibrium within each increment. The size of the increment affects the computational performance because when the increments are too large, more iterations are required to solve the analysis [111, 118].

4.1.2 Imaging Methods

There are systems that create images of the structures and activities inside entities of living tissue by the use of electromagnetic radiation or sound waves. These imaging

methods include the commonly used plane X-Ray to more complex techniques such as CT scans, MRI, nuclear medicine scans and ultrasound [8, 9, 11, 14, 16, 18, 44, 45].

Figure 4.1a shows a plane X-Ray image used to show abnormalities in bones by applying electromagnetic radiation. Figure 4.1b shows a Magnetic Resonance Image (MRI), which uses a strong magnetic field to produce detailed soft tissue images. Figure 4.1c shows a single slice from a set of CT scans. A CT scan is a cross-section image showing more detail than a typical X-Ray. In addition to showing soft tissue structures, a 3D image can be created from CT scan data by joining several slices.

A	b	c

Figure 4.1 Types of imaging diagnosis methods. (a) Plane X-Ray; (b) MRI; (c) CT scan.
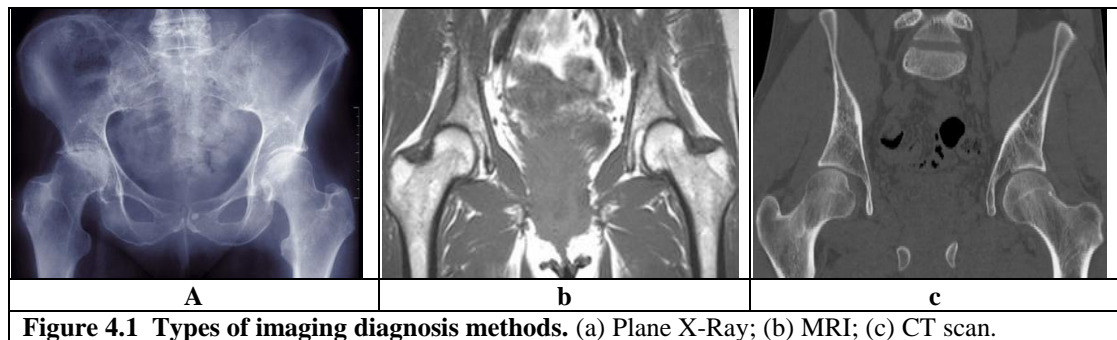
CT scans are commonly requested during the diagnosis stage of FAI and were employed in the present research to obtain the bone geometries. Unlike MRI, CT scanning produces much more transversal images, which leads to more accurate 3D geometries. Construction of the geometries is described in the following section.

4.2 Stress Analysis Following Osteochondroplasty

In cam-type FAI, abnormal contact occurs between the anterosuperior femoral head–neck junction and the acetabular cartilage [9, 11, 16, 23, 25] during flexion and internal rotation of the hip. Normally, this area of the femur has a concave configuration but in cam impingement it is flattened or convex [3, 9-11, 13-16, 18-20, 23, 25, 27, 28, 46, 47, 49], as illustrated in Figure 4.2b. Osteochondroplasty for FAI aims to alleviate abnormal contact to allow normal motion.
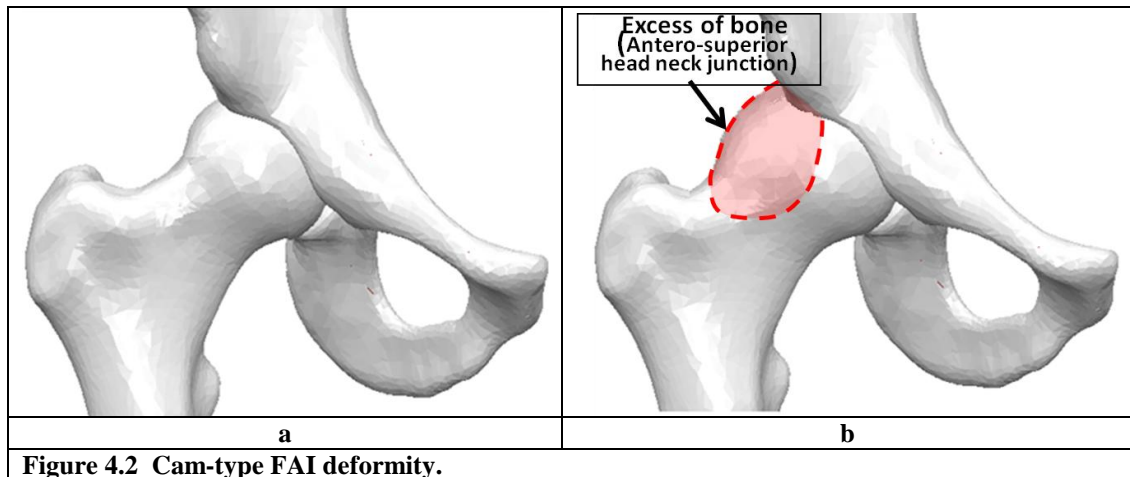
a	b
Figure 4.2 Cam-type FAI deformity.	

Logically, the greater the amount of bone removed, the greater the clearance for the safe range of hip movement without impingement. However, as resection depth increases, so would the likely stress in the remaining bone in the neck, increasing the risk of post-operative fracture. Neck fracture is recognized as a serious complication of hip arthroscopy [103, 104, 106, 107, 119] with incidence rates in the range of 0.8–1% [103, 106, 107].

To date, the only study known to address the issue of resection depth was presented by Mardones *et al.[3]*. They tested 15 cadaveric specimens from elderly patients divided into three groups (10%, 30% or 50%) based on the quantity of bone removed in the femoral neck. Bones were subjected to compressive loading to calculate their peak load, stiffness and energy to fracture.

The conclusion from the study was that the peak loads only increase significantly once 50% of the neck is removed. Although this study provides some guidance for establishing the safe resection depth limit in a femoral osteochondroplasty for FAI, the location of the resection area was fixed in the antero-lateral quadrant whereas in practice it is known that impingement area varies for each patient. In addition, this study has the disadvantage of having being performed on cadaveric specimens from elderly subjects (average age79 years), whose bones would have reduced in their strength due to the mineral decrement in people of that age.

A finite element (FE) model was developed to investigate the stress distribution in the femoral head–neck after resection. Five depths of resection in a cam-type impingement were considered in conjunction with five activities: standing on one leg (static), two-to-one-to-two leg standing, normal walking, walking down stairs, and a knee bend. The aim of this analysis was to understand the relationship between resection depth and the stress distribution in the head and neck.

4.3 Methods

To investigate the stress distribution in the femoral head-neck junction after osteochondroplasty, six 3D finite elements models were created from CT scan data of a patient exhibiting cam-type impingement (P-I). The first five models were subjected to virtual ostechondroplasties to obtain five different resection depths. The sixth model was left intact as a pre osteochondroplasty model. Each model was run under loading conditions corresponding to five daily activities: standing on one leg (static), two-to-one-to-two leg standing, normal walking, walking down stairs, and a knee bend. Figure 4.3a shows the CT scans of the abnormal morphology femur used for the models, whereas Figure 4.3b shows the contralateral hip which exhibits normal morphology.

Figure 4.3 CT scan diagnosis showing FAI. (a) Cam-type impingement hip; (b) Normal morphology hip.
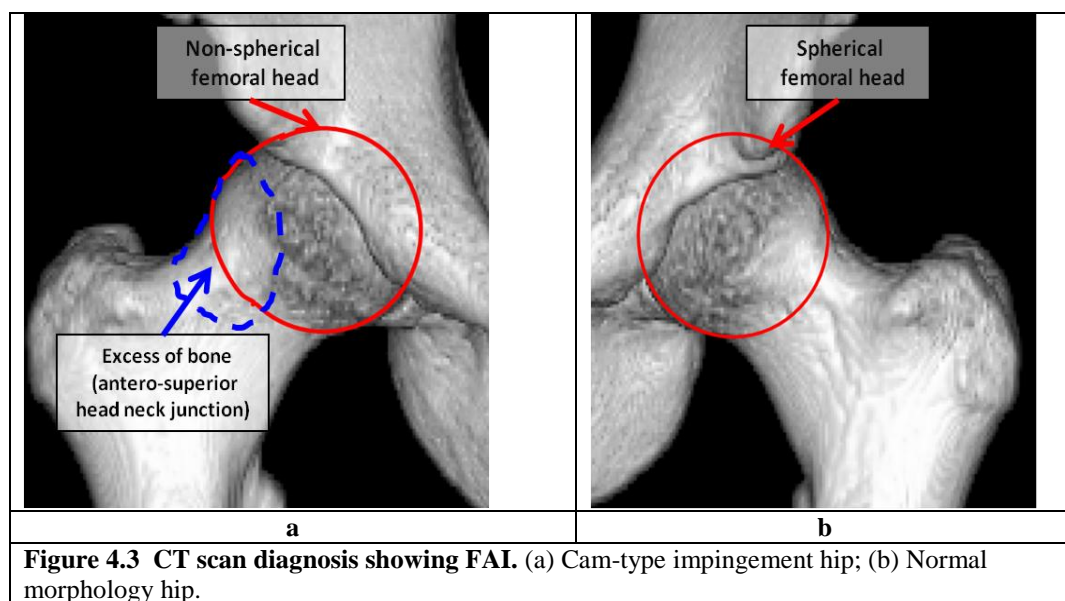
The development of the finite element models involved six main steps. First, the intact bone geometries were created from the CT scans. Secondly, the assembly of

the parts of the joint and any morphologic modifications needed were performed in Computer-aided design (CAD) software. In the third step, the necessary material properties for each tissue involved were defined according to the analysis to be performed. The fourth step was conversion of the solid geometries into a morphological arrangement of elements and nodes (mesh). In the fifth step the constraints and interactions between the geometries involved were defined, and, finally, the loading and boundary conditions needed to perform the finite element analysis were set up.

4.4 Geometry

The process of obtaining the geometry of each hip bone was performed by using Scan IP® to obtain the 3D surfaces of the bones. PowerSHAPE Pro® was used to create the solid volumes of the bones, preliminary cartilages and resection tools, and Abaqus CAE® to finalize the cartilages and to fix any conditions in the geometry that could lead to errors during the FEA.

4.4.1 Bones

The bone geometries for the finite element model were constructed using a commercial software package, ScanIP®, using DICOM data obtained from CT scanning. Each set of CT scans provides a variable number of images depending on factors such as the scanned body part, space between slices or size of the patient. Therefore, more cross sections mean less space between them and thus, less missing tissue, which results in more accurate geometry. The models constructed for this work required an average of 200 slices to accurately define the bone geometries of the hip.

CT scan greyscale images show all the tissues inside the body according to the density of the material. Bone is clearly defined but not cartilages, and so, cartilage geometry cannot be reproduced from CT scans. Software performance depends on the resolution of the images, so high resolution reduces working-time to define the geometry and software tools provide better results. Figure 4.4a shows a high resolution CT scan which is more useful for reproducing the geometries, whereas

Figure 4.4b shows a poor resolution CT scan which complicates the construction process.

a	b
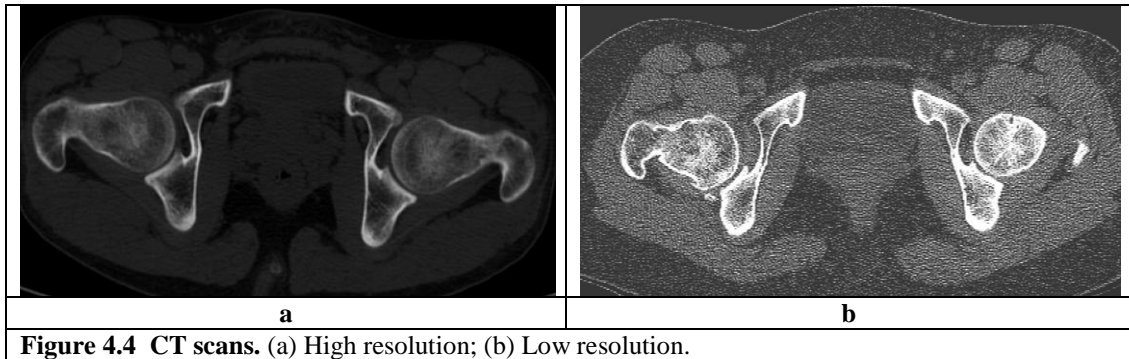
Figure 4.4 CT scans. (a) High resolution; (b) Low resolution.

Since every set of CT scans was different, the resolution, size, and position of the slices varied for each patient, and so it was important to have good knowledge of the anatomy involved to correctly interpret the images. However, it is even more important to be able to detect the bone abnormalities which are the focus of the present research in order to reproduce the geometries of the abnormal bones as accurate as possible. Scan IP® reads the DICOM images and displays each of them in different views as Figure 4.5 shows.
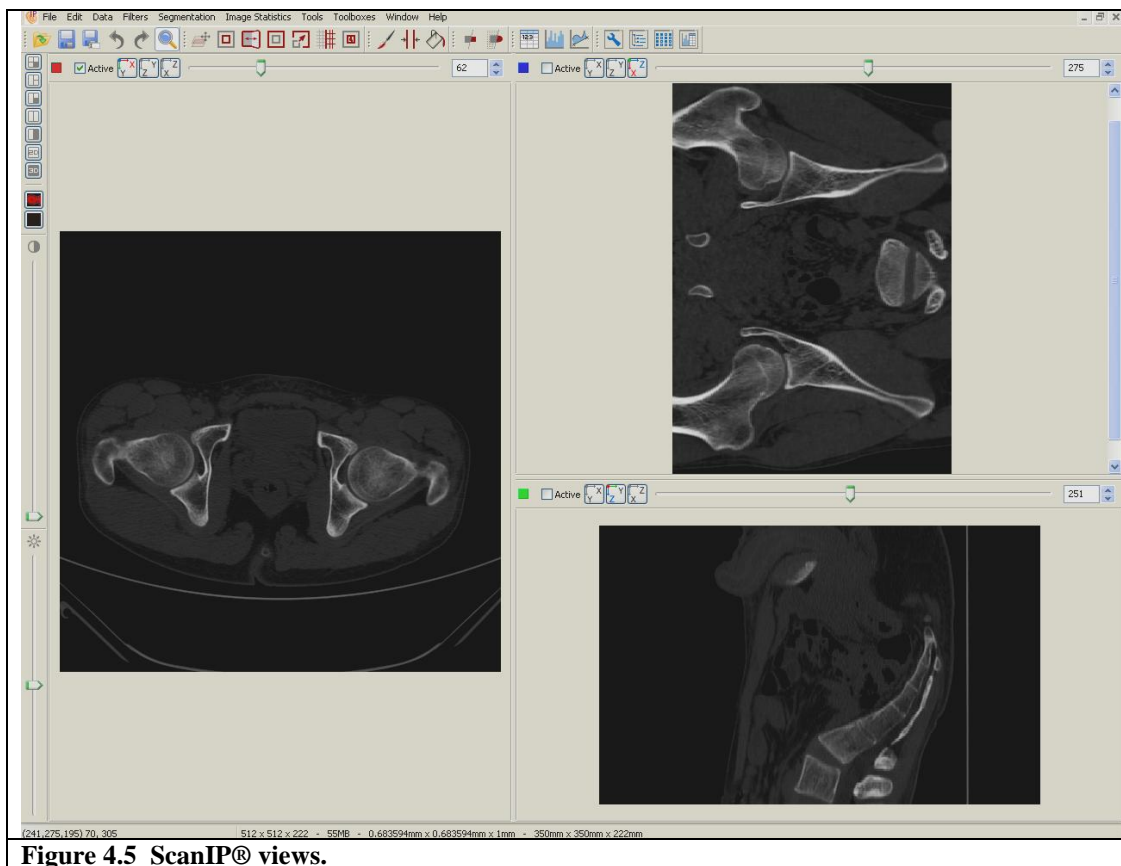
Figure 4.5 ScanIP® views.

By applying segmentation tools and morphological filters in Scan IP® colour masks were created to define the geometries. The segmentation process was performed by using "Threshold" and "Paint" tools to define the areas of interest by taking the information from the image data in order to create colour masks which delineate the tissues required. The threshold tool creates a mask based on greyscale values, so that the mask is made by the pixels included in the greyscale range defined. The paint tool allows the merging and splitting of the segments in a mask, by selecting of just an individual pixel, which is very useful for complex geometries [120].

Morphological filters are applied in the colour masks to improve the surfaces of the geometries obtained after segmentation. First, a "Binarisation" filter is applied to assign one value of the greyscale range to the complete mask to eliminate the connection between the mask and the background, and to homogenize the mask itself. Once the masks were more homogeneous, a "Smoothing" filter is applied to refine the contours of the surfaces [120].

Figures 4.6a and 4.6b show transversal and frontal views of one slice of the femoral epiphysis mask obtained in Scan IP® before and after applying the morphological filters.

Transversal plane	Frontal plane
a	
Transversal plane	Frontal plane
b	

Figure 4.6 Mask of the femoral epiphysis in Scan IP®. (a) Before filters; (b) After filters.
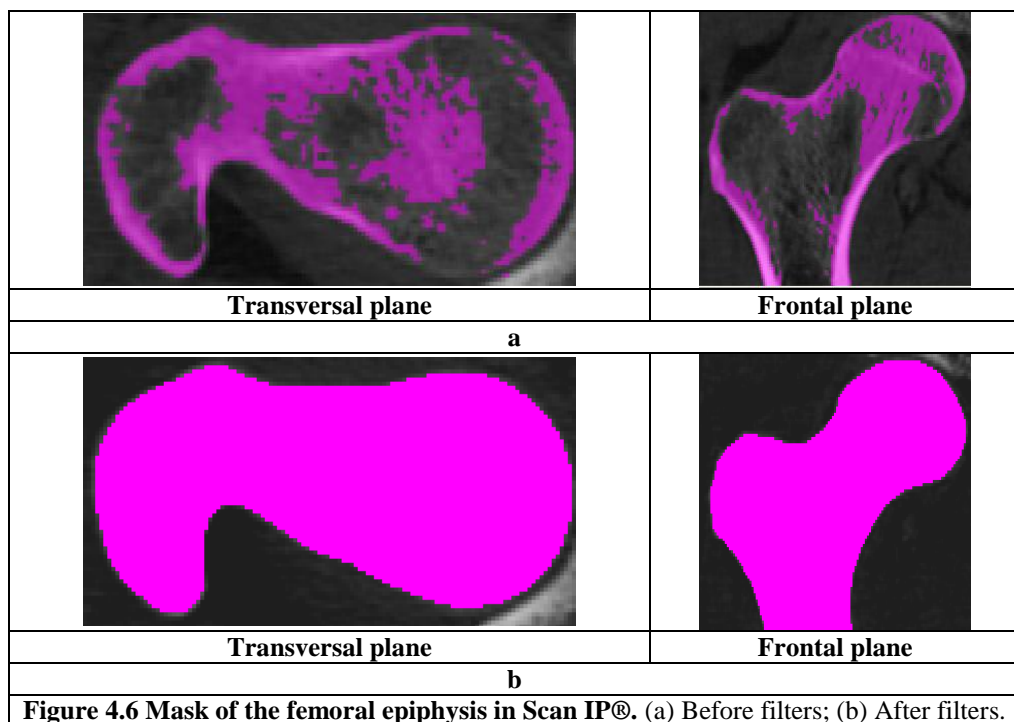
Scan IP® created a 3D surface from the final mask obtained after applying the filters, which was saved and exported as an IGES (Initial Graphics Exchange Specification) file. To describe the surface to be exported, Scan IP® uses triangular geometric entities to adjust as close as possible to the shape obtained from the CT scans.

Triangles are the geometric entities used to describe, in a finite number of regular surfaces, the outer area of an irregular 3D geometry such as bone. Scan IP® needs to describe the bone geometries in triangles in order to be able to import them into the software. So it can de deduced that, the more triangles that are used to describe the surface, the more accurate the final geometry will be. A maximum of 5000 triangles per part was used to export each 3D surface as this was the maximum number of triangles permissible on the computer system. Figure 4.7 shows the 3D view of the femur surface ready to be exported from ScanIP® .
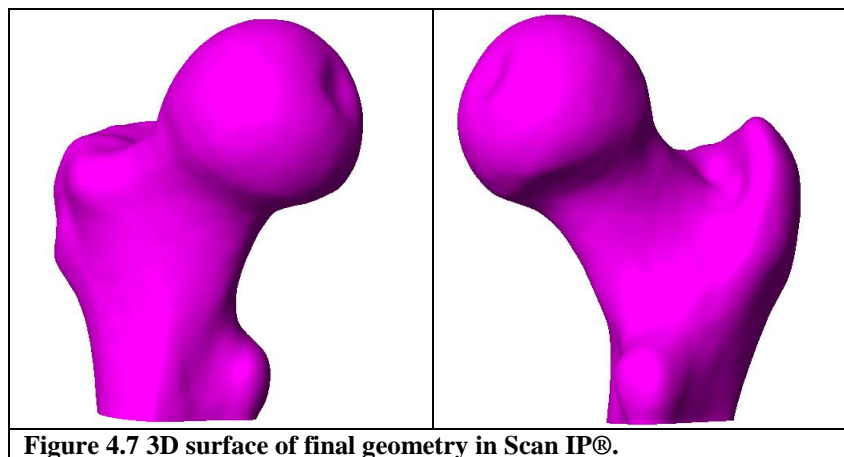
Figure 4.7 3D surface of final geometry in Scan IP®.

4.4.2 Cartilages

The geometries from ScanIP® were imported to PowerSHAPE Pro® as solid volumes in case they needed modification and mainly to help in the creation of the preliminary cartilage missing geometry.

PowerSHAPE Pro® is a Computer-aided design (CAD) system capable of designing and modifying imported 3D parts. Preliminary femoral cartilage was created from an expanded mask of the femur to cover the actual location of the cartilage, which was unclear in the DICOM images. For the creation of the preliminary acetabular cartilage an expanded mask of the pelvic bone was used, but since it was very difficult to create such complex shapes, extra regular geometries were used to

finalize the geometries in Abaqus CAE®. Figures 4.8a and 4.8b show the process of creating the preliminary cartilages in PowerSHAPE Pro®.

Femur (normal geometry)	Femur (normal + expanded geometries)	Femoral (preliminary cartilage)
	a	
Pelvis (normal geometry)	Plevis (normal + expanded geometries)	Acetabular (preliminary cartilage)
	b	

Figure 4.8 Development of preliminary cartilages in PowerSHAPE Pro®. (a) Femoral cartilage; (b) Acetabular cartilage.
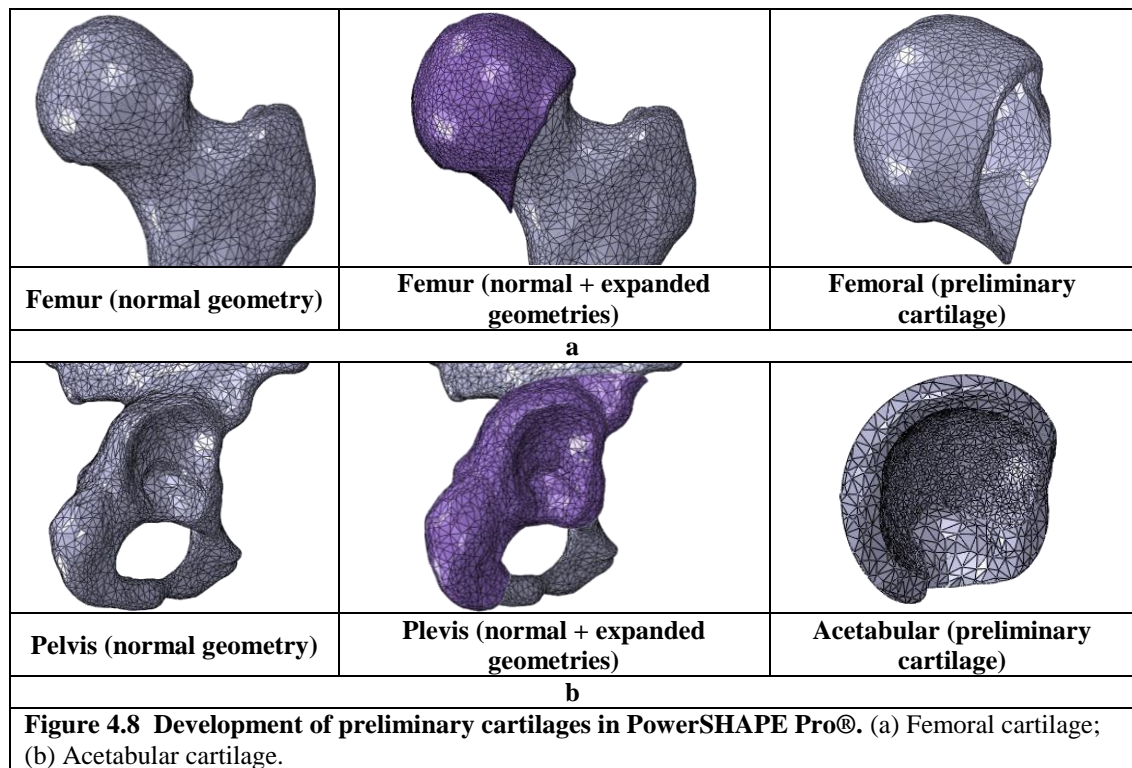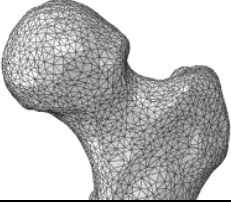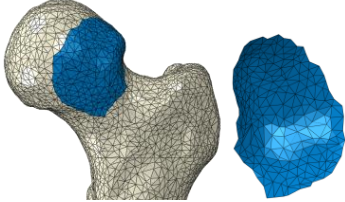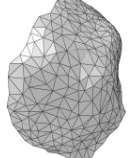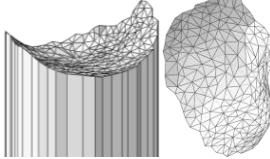
4.4.3 Resection tool

Resection tools were used to perform the extraction of volume of the femur in the models in order to simulate the osteochondroplasty surgery. They were specially created according to the requirements of each model because the location and area to be resected varied for each patient. The resection area should not stray above the equator of the femoral head which is defined as perpendicular to the femoral neck axis. The extent of the resection infero-lateral to the equator depends on the exact position of the cam deformity. Commonly this is anterior, supero-anterior or antero-medial.

During the development of the present research, the process of creating the resection tools was improved, so that, in the first analysis, the initial resection tool was a solid volume based on the triangular surfaces selected on the model by the surgeon as the area to be resected, as described in Table 4.1. The surgeon selected the triangular surfaces directly in the geometry of the cortical bone in Abaqus CAE® to form the resection area (Step 2-3). The resection area was extruded in PowerSHAPE Pro® to

create the initial resection tool, "Initial RT" (Step 5). The use of the "Initial RT" led to irregular resections as a result of the small edges and changes of direction on the perimeter of the resection area formed by the addition of the small triangular surfaces. Before starting the construction of any of the resection tools, it was essential to finish and assemble all geometries involved in the non-resection model in Abaqus CAE®.

Table 4.1 Process to create the RT.

Step	Initial RT
1. Import geometry from ScanIP®. ***Abaqus CAE®**	
2. Simulate the virtual osteochondroplasty (triangular surfaces selected by the surgeon). 3. Eliminate outer resection area surfaces. Export. ***Abaqus CAE®**	
4. Import the resection area ***PowerSHAPE Pro®**	
5. Extrude the surface, convert it to a solid part and export as IGES file (RT). ***PowerSHAPE Pro®**	
Software used during the step.	

4.4.4 Geometry Repair

Because the bones were irregular, geometric inaccuracies were common in the imported parts. In this case, the geometry was considered invalid and its use during modelling lead to errors. Abaqus CAE® was able to manually repair and improve any inaccuracy in the geometry to avoid errors in the FEA, by replacing or removing

faces, merging small edges, or stitching small gaps. Figure 4.9 shows a section of an inaccurate geometry before and after repairs.

Imprecise geometry	Imprecise faces	Repaired faces

Figure 4.9 Imprecise section repaired in Abaqus CAE®.
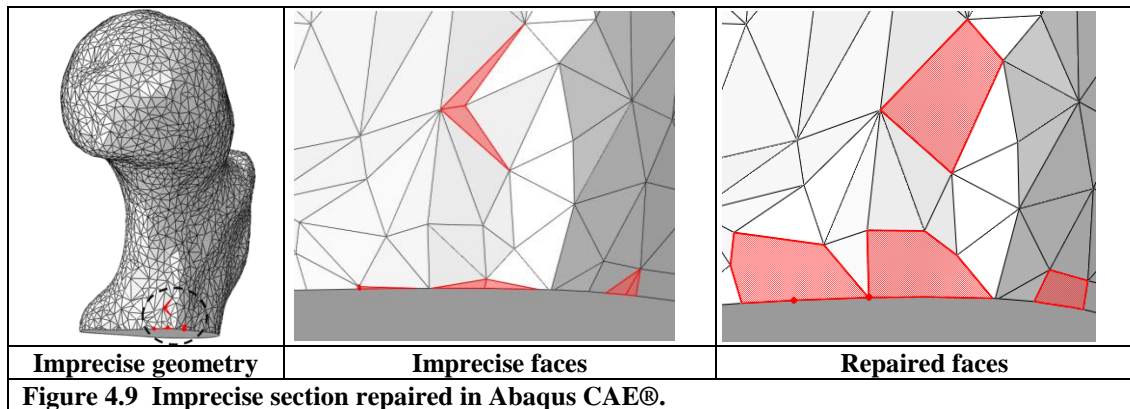
4.4.5 Virtual Resections

As described in Section 4.4.3, the development of the resection tool (RT) was needed to perform the virtual resections. The "Initial RT" was used in the analysis of the resection depth. Virtual resections were constructed in Abaqus CAE® by using subtraction/intersection operations, which facilitated the removal of virtual material. Figure 4.10 shows the steps used to perform a virtual resection with the "Initial RT" in the femoral head-neck junction.

Before virtual resection	RT	Bone - RT	After virtual resection

Figure 4.10 Volume removal in Abaqus CAE®. (Initial RT).
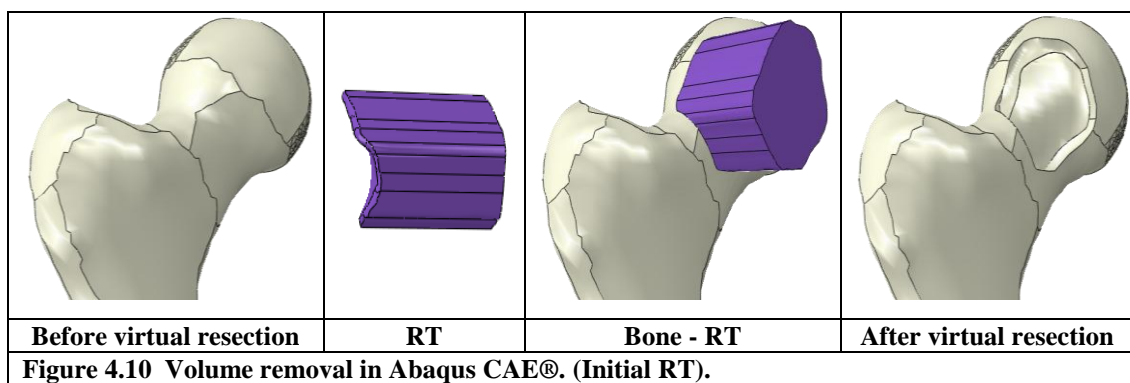
For the resection depth stress analysis, five virtual osteochondroplasty models were generated. In each case, the same outer area of resection was considered as this was the maximum extent of the impingement zone indicated by the CT scan. The resection depth for a cam-type impingement such as this one would typically be between 4 to 8 mm and involves the removal of cartilage, and cortical and trabecular

bone. Figure 4.11 illustrates the six models developed and their corresponding resection depths.

0 mm	**2 mm**	**4 mm**
6 mm	**10 mm**	**15 mm**

■ **Cortical bone**
■ **Trabecular bone**
□ **Cartilage**

Figure 4.11 Resection area and depths considered in the study.
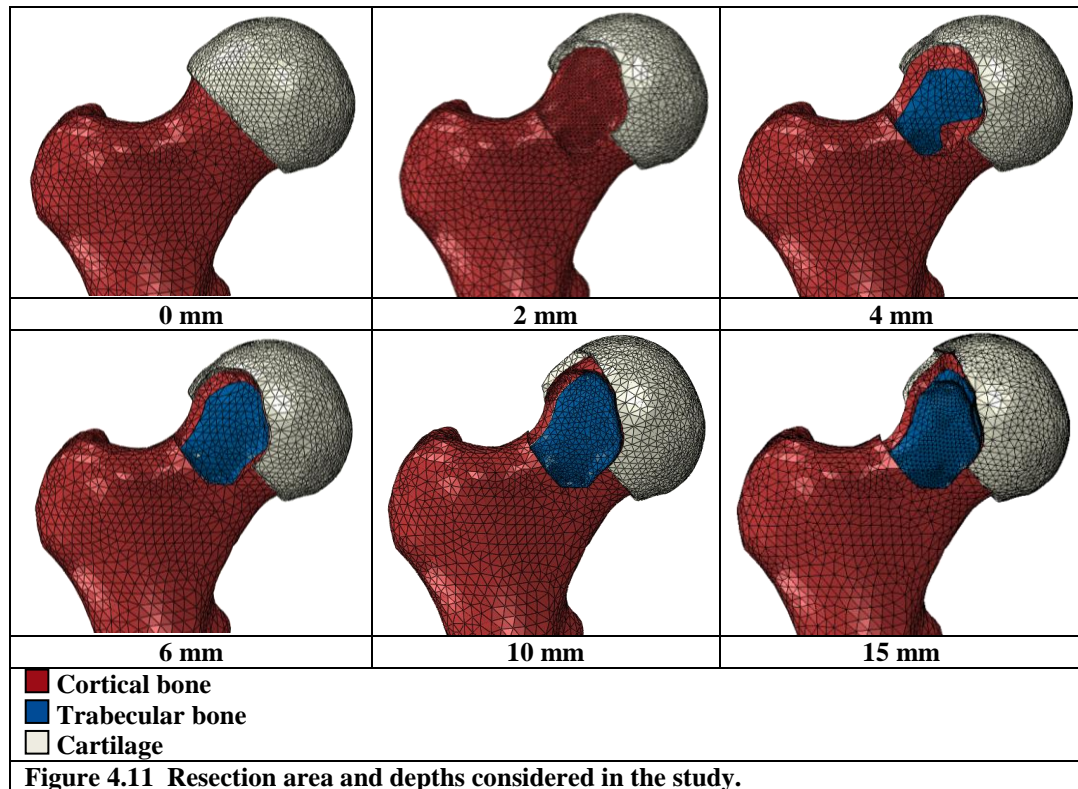
4.5 Material Properties

In contrast to engineering materials such as metals, plastic or composites, biological materials alter their mechanical properties and morphology in response to appropriate stimuli, which makes the study of their mechanical properties very challenging. Bone and cartilage are non-homogeneous anisotropic materials. However, even though their behaviour has been demonstrated before, most of the FEA of bone developed to date have assumed isotropic and homogeneous properties.

For this research, the assumption of isotropy and homogeneity of the bone was adequate, since the analysis was focused on the effect of the resection in the stress distribution within the bone, the range of motion of the joint, and in the contact surfaces [35, 76-81, 121-125].

Material properties for all the geometries involved were defined before performing the FEA. For this analysis, it was assumed that the materials exhibited simple elastic-

plastic behaviour with properties taken from the literature. Table 4.2 shows the material properties for the two types of bone and cartilage used [54, 121, 126-128].

Table 4.2 Material properties used in the resection depth and range of motion FEA [54, 121, 126-128].

Material	Young's modulus E [MPa]	Poison's ratio	Yield stress σ [MPa]	Material behaviour
Cortical bone	17,000	0.3	100	Homogeneous, elastic-plastic, isotropic
Trabecular bone	150	0.3	6	Homogeneous, elastic-plastic, isotropic
Cartilage	12	0.4	5	Homogeneous, elastic-plastic, isotropic

4.6 Boundary Conditions

Finite element modelling requires development of a single assembly that includes the geometry of all the parts and the constraints and interactions between them, and also the boundary conditions needed to define and simulate the environment for each model.

Based on a master-slave scheme, constraints allow partial or total reduction of the degrees of freedom of a slave group of nodes by defining kinematic relationships between them and a master group of nodes. Consequently, the motion of the slave depends of the motion of the master. Constraints are defined in the assembly and remain throughout the analysis. In the case of the interactions, the master-slave scheme is used to define the type of contacts, transmission of forces, and friction between parts that interact at some point of the analysis. Interactions are enabled only in the steps of the analysis where they are required.

The external conditions to which the models are subjected such as concentred forces, pressure, displacements, and rotations are simulated by using loads and boundary conditions in Abaqus CAE®. Each analysis needs to define specific conditions based on the situation to be simulated and the output variables required.

For the stress analysis, a section of the hemi-pelvis including the acetabulum was incorporated in the model to transmit the concentred forces to the femoral head. To avoid local stress concentrations and localized deformations, the pelvic section was

set as a rigid body enabling it to effectively transfer the load on to the head. The interface between the head and acetabulum was modelled using the ''tie'' constraints of Abaqus CAE 6.9-2®, so that adjoining nodes had the same displacements. Full fusion was assumed at the interface between cortical and trabecular bones.

The bottom surfaces of the proximal femoral segment were fixed in displacement and rotations in all directions. Concentred forces corresponding to each activity were used to represent the abductor muscle and the force on the head due to body weight.

The muscle force (F_M) was applied at a reference point above the greater trochanter using a kinematic coupling constraint to include the anatomy location of the abductor muscles, whereas the concentrated force corresponding to the femoral head (F_{FH}) was applied to the top of the pelvic section. Figure 4.12 illustrates all the boundary conditions used for the resection depth analysis.

Figure 4.12 Boundary conditions for the resection depth analysis.
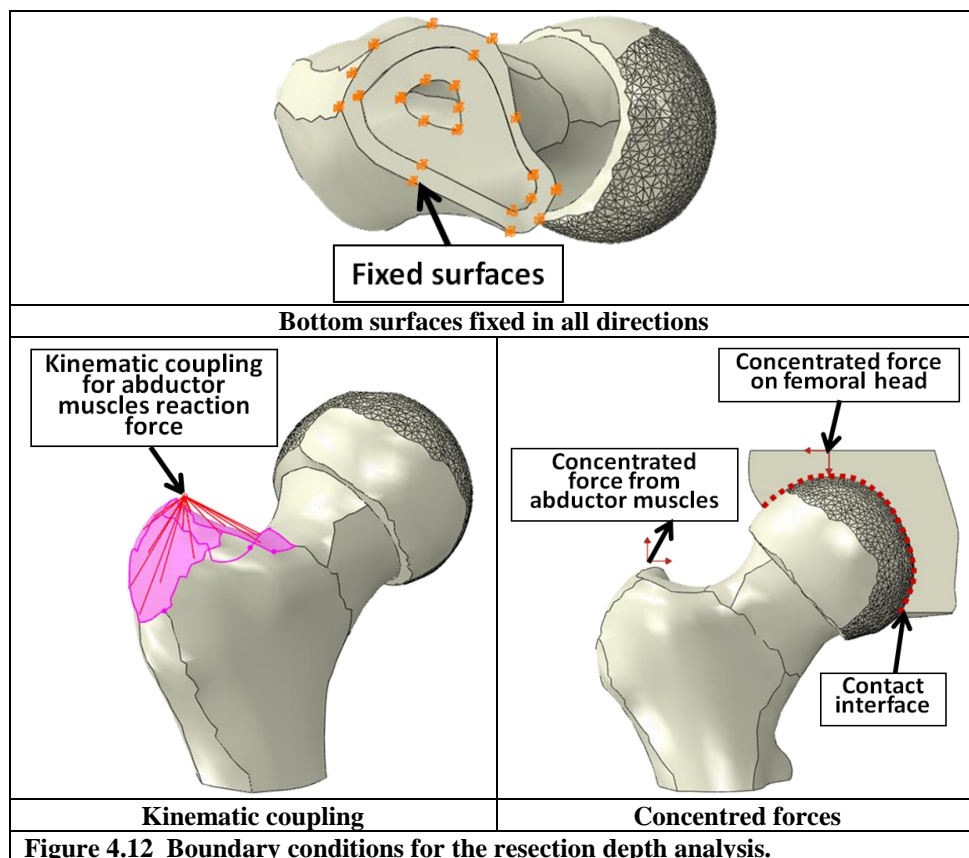
A free body diagram of the upper part of the femur was used to calculate the reaction forces on the head and from the abductor muscles, as shown in Figure 4.13.

$$F_M \cos(\Theta_2) + W = F_{FH} \cos\Theta_1$$
$$F_M \sin(\Theta_2) = F_{FH} \sin\Theta_1$$

CG = CENTRE OF GRAVITY
W = BODY WEIGHT
F$_{FH}$ = REACTION FORCE ON FEMORAL HEAD
F$_M$ = REACTION FORCE FROM ABDUCTOR MUSCLES
Θ_1 = ANGLE BETWEEN ACTION LINES OF **W** AND **F$_{FH}$**
Θ_2 = ANGLE BETWEEN ACTION LINES OF **W** AND **F$_M$**

Figure 4.13 Free body diagram of the lateral side of the upper part of the body.
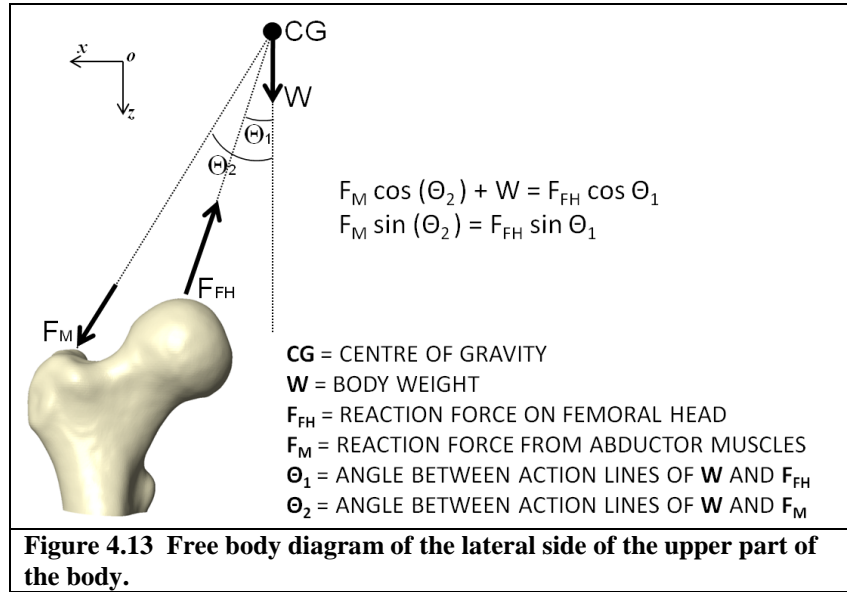
To determine the forces applied to the models, a percentage of the body weight and angles depending upon the activity were considered [129]. The maximum values for each activity were employed. Table 4.3 illustrates the forces and the associated angles calculated from the free body diagram.

Table 4.3 Concentrated forces and variables considered in the resection depth FEA.

Activity	Angles	W [N]	%W	F$_M$ [N]	F$_{FH}$ [N]
1 leg stand (static)	$\Theta_1 = 13°$ $\Theta_2 = 20°$	785	90	1,303	1,982
Normal walking	$\Theta_1 = 13°$ $\Theta_2 = 20°$	785	238	3,447	5,242
Downstairs	$\Theta_1 = 12°$ $\Theta_2 = 20°$	785	260	3,049	5,015
Knee bend	$\Theta_1 = 16°$ $\Theta_2 = 20°$	785	143	4,435	5,503
2-1-2 legs standing	$\Theta_1 = 7°$ $\Theta_2 = 20°$	785	231	982	2,757

For the present analysis, only the frontal plane forces were considered as these are generally higher forces than the transversal plane forces and our focus was on investigating which postoperative activities are important to avoid. Table 4.2 lists the force components estimated for each activity.

Table 4.4 Force decomposition.

Activity	F_M [N]	F_M Components [N]		F_{FH} [N]	F_{FH} Components [N]	
1 leg stand (static)	1,303	$F_{M(X)} = 445$		1,982	$F_{FH(X)} = -445$	
		$F_{M(Z)} = 1,225$			$F_{FH(Z)} = -1,931$	
Normal walking	3,447	$F_{M(X)} = 1,179$		5,242	$F_{FH(X)} = -1,179$	
		$F_{M(Z)} = 3,239$			$F_{FH(Z)} = -5,107$	
Down stairs	3,049	$F_{M(X)} = 1,042$		5,015	$F_{FH(X)} = -1,042$	
		$F_{M(Z)} = 2,865$			$F_{FH(Z)} = -4,906$	
Knee bend	4,435	$F_{M(X)} = 1,516$		5,503	$F_{FH(X)} = -1,517$	
		$F_{M(Z)} = 4,167$			$F_{FH(Z)} = -5,290$	
2-1-2 legs standing	982	$F_{M(X)} = 336$		2,757	$F_{FH(X)} = -355$	
		$F_{M(Z)} = 923$			$F_{FH(Z)} = -2,737$	

4.7 Mesh Sensitivity Analysis

The meshing process took place in Abaqus CAE®. Discrete geometries were created based on elements and nodes to approximate the original geometries of the model. Since the parts involved in the model of the hip joint were very complex, 4-node linear tetrahedral elements were used to mesh them; C3D4 (Continuum, 3D, 4 node). Figures 4.10.a and 4.10.b show a hypothetical 4-node tetrahedral element and a section of meshed geometry.

a	b
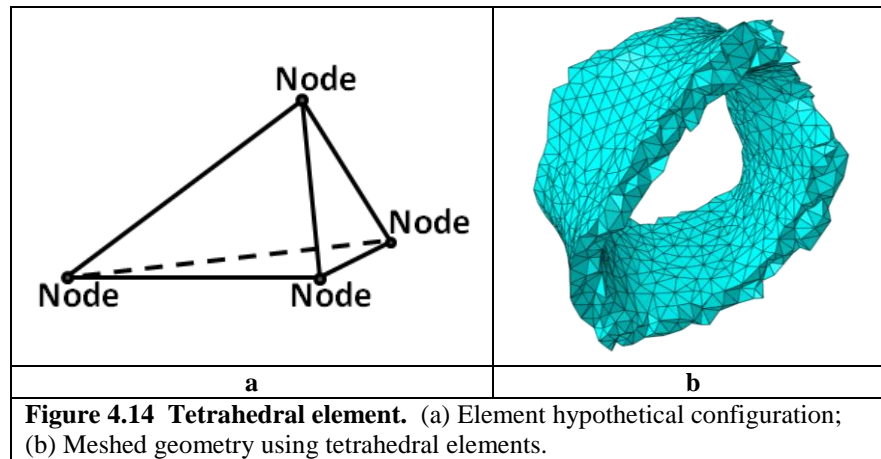
Figure 4.14 Tetrahedral element. (a) Element hypothetical configuration; (b) Meshed geometry using tetrahedral elements.

The number of elements varied in each model depending on the number needed to describe the geometry involved. In the case of complex geometries, a finer mesh means better geometry but also longer computation time to run the analysis, whereas, a coarse mesh gives imprecise geometry and unreliable results. In the meshing tools from Abaqus CAE® it is possible to assign different densities to describe the same geometry but the results may vary.
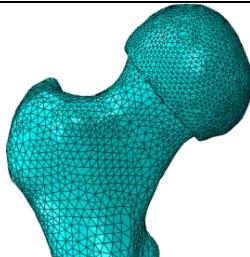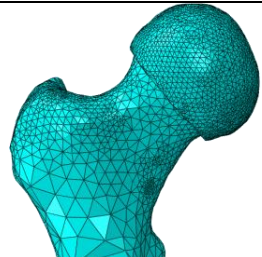
The final number of elements used to mesh the geometries was automatically calculated by Abaqus CAE® once the approximate global element size was specified, which determines the length of the edges of each element. Consequently, a mesh convergence analysis was performed to define the density of the mesh to use and to obtain consistent results.

The mesh convergence analysis was performed to ensure accuracy of the results by assigning different mesh densities in a single model and running them under the same conditions and analysing the variation in the results obtained. Mesh densities were chosen between the maximum and minimum number of elements that could describe the geometry.

The analysis consisted of employing the non-resection, intact model and three densities (360,444, 91,068 and 77,666 elements) and comparing the average von Mises stress in the head-neck shaft section. The mesh containing 360,444 elements was named the "fine" mesh, that containing 91,068 elements, the "middle" mesh and the mesh with 77,666 elements, the "coarse" mesh.

As a result of the analysis, the "middle" mesh density was chosen because the average von Mises stress changed by less than 0.5% in comparison with the "fine" mesh whilst computation time was significantly reduced. Results from the mesh sensitivity analysis are listed in Table 4.5.

Table 4.5 Mesh sensitivity analysis.

Mesh			
	Fine	**Middle**	**Coarse**
Number of elements	360,444	91,068	77,666,
Computer time	24 hours	4 hours	3.8 hours
Average von Mises variation	----	0.3%	6.5%

The number of elements used changed with resection depth due to the removal of material and the geometry of the remaining resected area. After a virtual resection, the area exposed was highly irregular, and a large number of elements were required to capture the geometry and ensure high accuracy in stress predictions. Although less volume of trabecular bone was being meshed as the resection depth increased, the number of elements employed actually increased due to the increased complexity of the geometry. Table 4.6 lists the number of elements employed in each model.

Table 4.6 Number of elements employed in the models for the resection depth FEA.

Resection depth [mm]	Tetrahedral Elements			
	Cortical	Trabecular	Cartilage	Total
0	25,959	55,465	9,644	91,068
2	28,586	55,465	9,403	93,695
4	26,453	57,231	9,248	92,932
6	25,333	58,976	9,453	93,762
10	24,991	61,043	8,702	94,736
15	24,189	67,056	8,551	99,796

4.8 Validation of the Model

The model was validated by comparing predictions from the intact femur model with results from a cadaveric study presented by Mardones *et al.* [3]. The investigation by Mardones *et al.* consisted of testing 15 pairs of femora to fracture using a materials testing system following removal of 10%, 30%, or 50% of the femoral neck from one femur in each pair. The contralateral femur was left intact as a control. A compressive load was applied to the head at a displacement rate of 20 mm/min until fracture. The intact, non-resection femur model was corroborated against the results from the control femora group in the cadaver study.

Appropriate boundary conditions were applied, and compressive loading was applied to the head at the same rate as in the experimental study. Mean age for the cadavers was 79 years (range of 57–98 years) so the elastic modulus of the cortical and trabecular bone in the model was reduced from the healthy values for cortical and trabecular bones by 32% and 66%, respectively [130, 131] to represent the typical reduction in elastic modulus with age and the degree of osteoporosis.

The stiffness of the neck was calculated from the linear portion of the load–displacement curve from the model and was compared to the mean neck stiffness from the cadaveric control group. Figure 4.15a illustrates the experimental set up for the compression testing and Figure 4.15b shows the modelling settings employed for the comparative analysis. Figure 4.16 shows the stiffness comparison between the model and the experimental results (638 N/mm for the model compared with 686 N/mm for the cadaveric study).

| a | b |

Figure 4.15 Physical corroboration settings. (a) Experimental study set up (modif.) [3]; (b) FE Model.

Figure 4.16 Stiffness comparison.
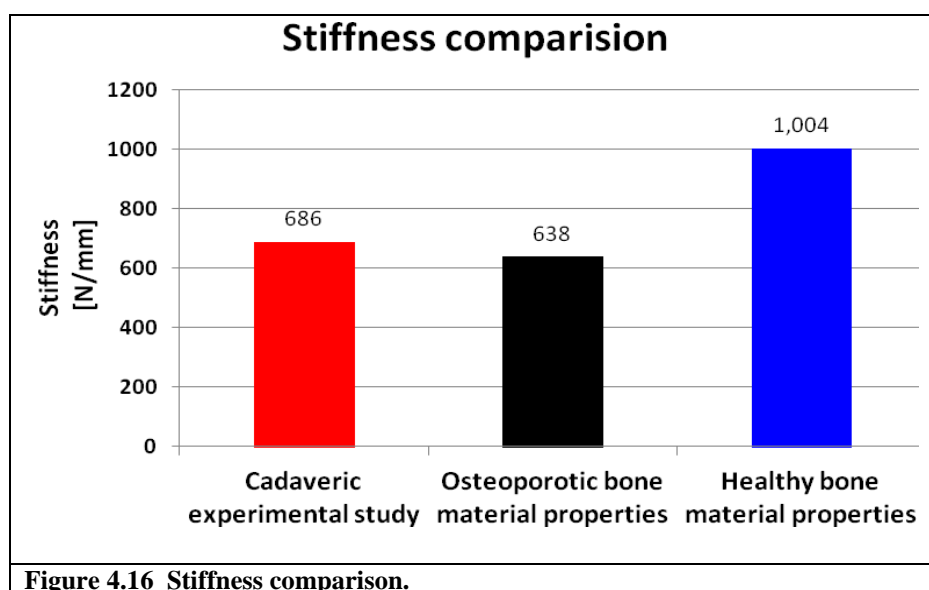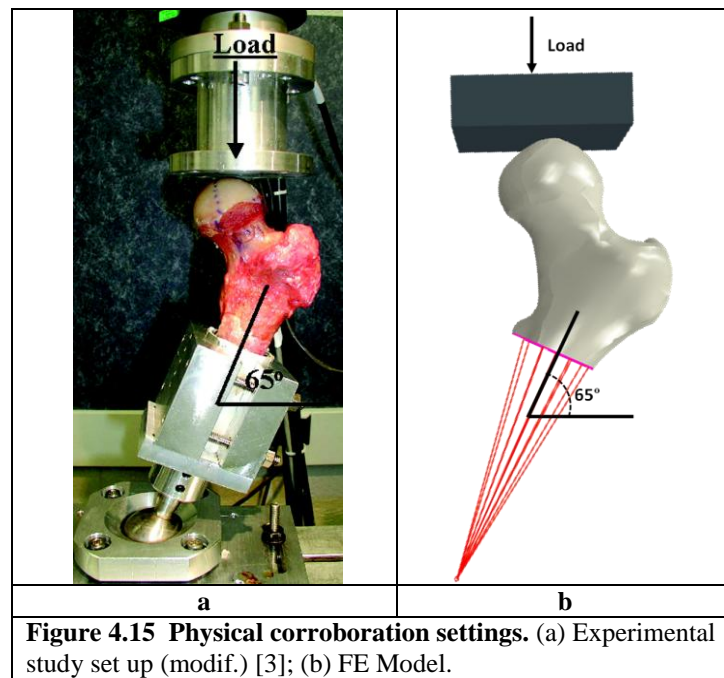
4.9 Results

A preliminary analysis was performed to compare the von Mises and the maximum principal stresses in the femoral neck. This analysis was carried out in all the resection models for the knee bend forces. In addition, the analysis was undertaken for all the activities for the 6mm resection depth model. The trend of the average values of von Mises and maximum principal stresses for various levels of resection was broadly similar; however, numerical values of maximum stress may be very high at a point due to surface irregularity after a virtual resection is performed. These irregularities may not be present in actual patients, but hard to avoid in numerical models due to non-uniform element sizes. Hence average von Mises stresses and yielded volumes were reported in four zones of the resection area.

The depth of the zones was taken to be the coronal plane at a level 1 mm below the maximum resection depth. Four zones of interest (A–D) were defined in the resection region, as shown in Figure 4.17.

| a | b | c |
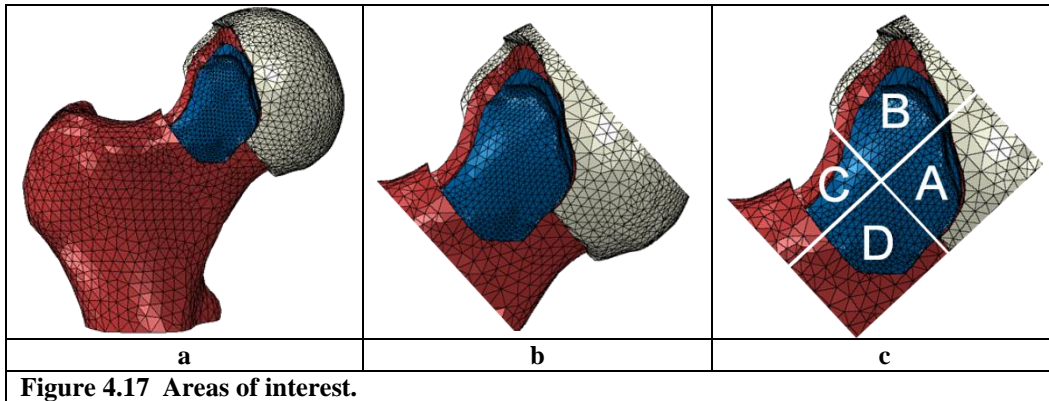
Figure 4.17 Areas of interest.

Average von Mises stresses and the yielded volume were calculated for each zone. Average stresses were calculated by multiplying the volume of each element by its corresponding stress value. These results were then added together before being divided by the total volume of the elements in the zone:

$$\text{Average von Mises stress} = \frac{\sum_i V_{E_i} S_{E_i}}{\sum V_{E_i}} \tag{6}$$

Where V_{E_i} is the volume of the *i*th element of the zone under consideration; S_{E_i} is the von Mises stress in the *i*th element of the zone.

Figures 4.18–4.21 show the average von Mises stress and the volume of material yielded in the inferior-medial (A), superior-medial (B), superior-lateral (C), and inferior-lateral (D) areas of the resection, respectively, for the different resection depths and activities. Higher von Mises stresses were obtained for the knee bend, normal walking, and walking down stairs activities. In the case of the B and C resection areas, the knee bend had the highest average stresses at all resection depths, as shown in Figures 4.18a–4.21a. For the remaining two resection areas (A and D), the results for knee bend, normal walking, and walking down stairs activities were similar, between 1.4 and 2.5 times greater for the maximum resection depth compared to the non-resection case.

In all the cases, the average von Mises stress increased with resection depth. In the case of A, B, and D resection areas, the rate of increase in average stress became greater at resections ≥10 mm, corresponding to depths equal to ≈1/3 of the average diameter of the neck and beyond. At resection depths <1/3 of the diameter of the neck (depths of <10 mm), the volume of material yielded was small, as shown in Figures 4.18b–4.21b.

The volume yielded increased significantly at resection depths of 10 and 15 mm, corresponding to 1/3 and 1/2 of the neck diameter, respectively. Yielding was confined to the cortical bone and was only significant in the knee bend, normal walking, and walking down stairs activities.

As previously described in this Chapter (Section 4.8), the non-resection model was corroborated against the control group from Mardones *et al.* So, it is possible to compare the results from the resection models with the results from the compressive tests in the resected femurs. Results from the models indicate that the rate of increase in stress becomes greater at resections ≥10 mm, which represents 30% of the head-neck shaft diameter. The results from Mardones *et al.* show that the loading required to reach the fracture in the femurs was reduced significantly when the bones have been resected by 30% of their head-neck shaft diameter. Thus, both studies suggest that the safe resection depth cannot be deeper than 1/3 of the diameter of femoral head-neck shaft.

b

a
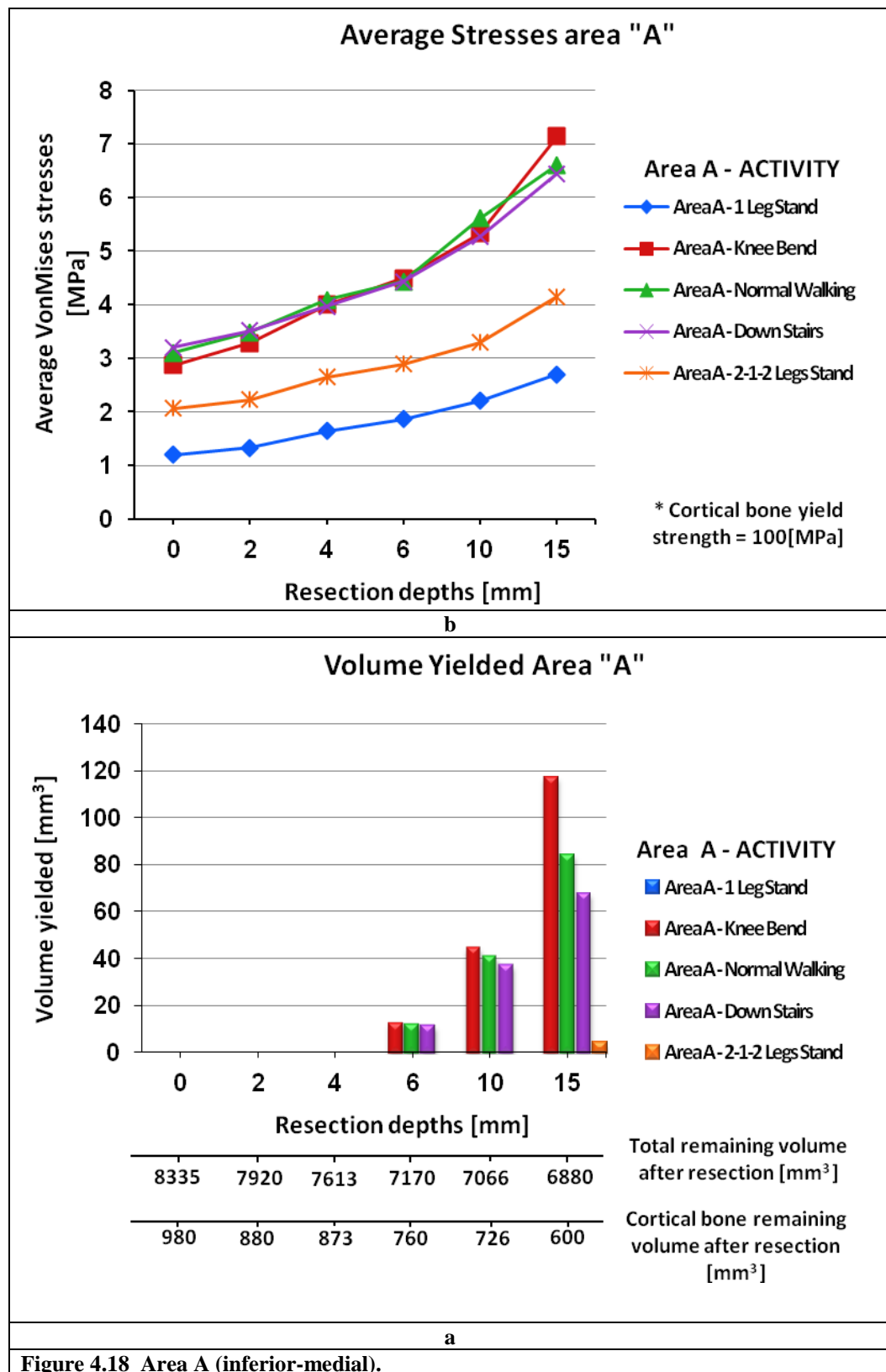
Figure 4.18 Area A (inferior-medial).

Figure 4.19 Area B (superior-medial).

a

b

Figure 4.20 Area C (superior-lateral).

a

b

Figure 4.21 Area D (inferior-lateral).
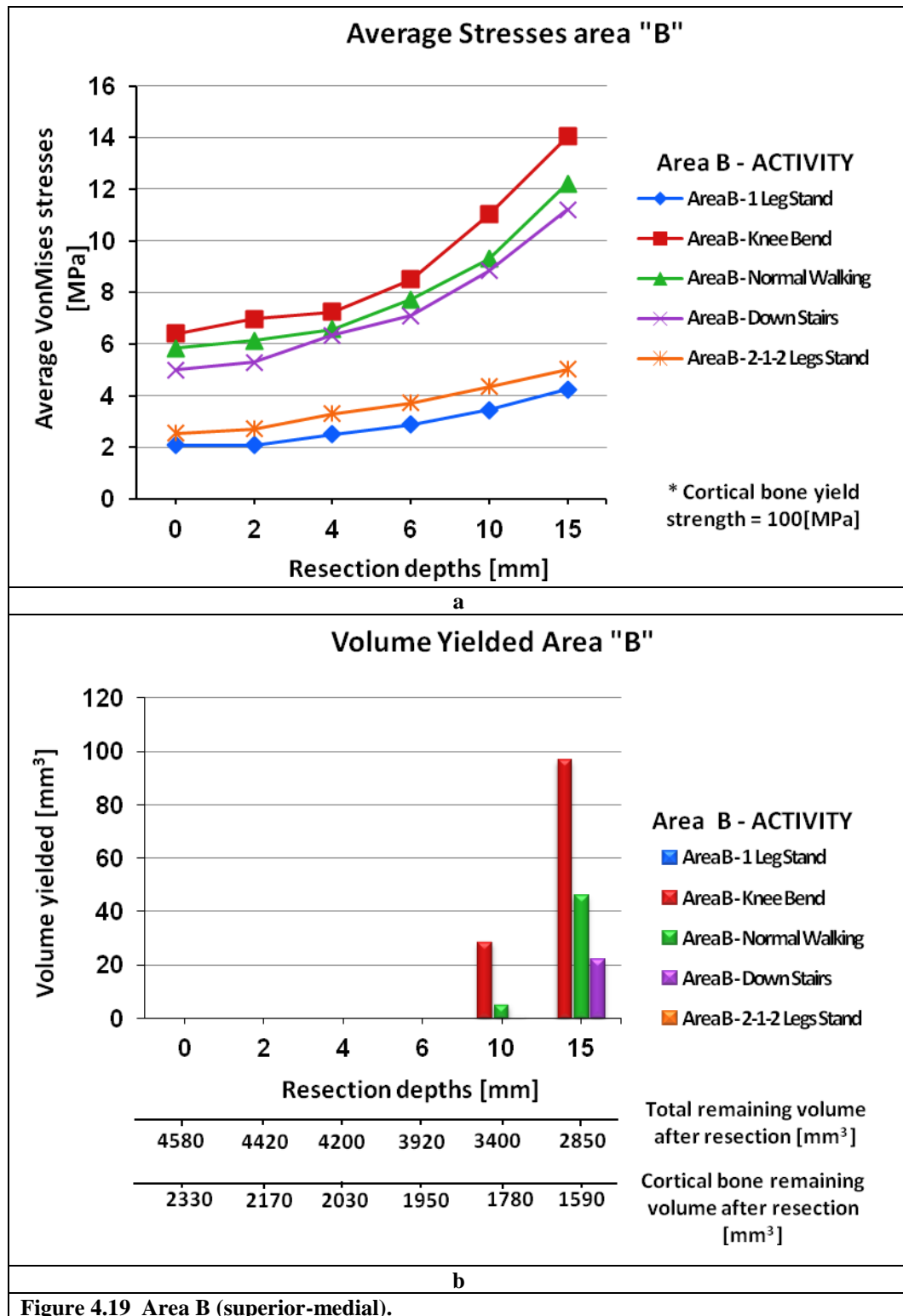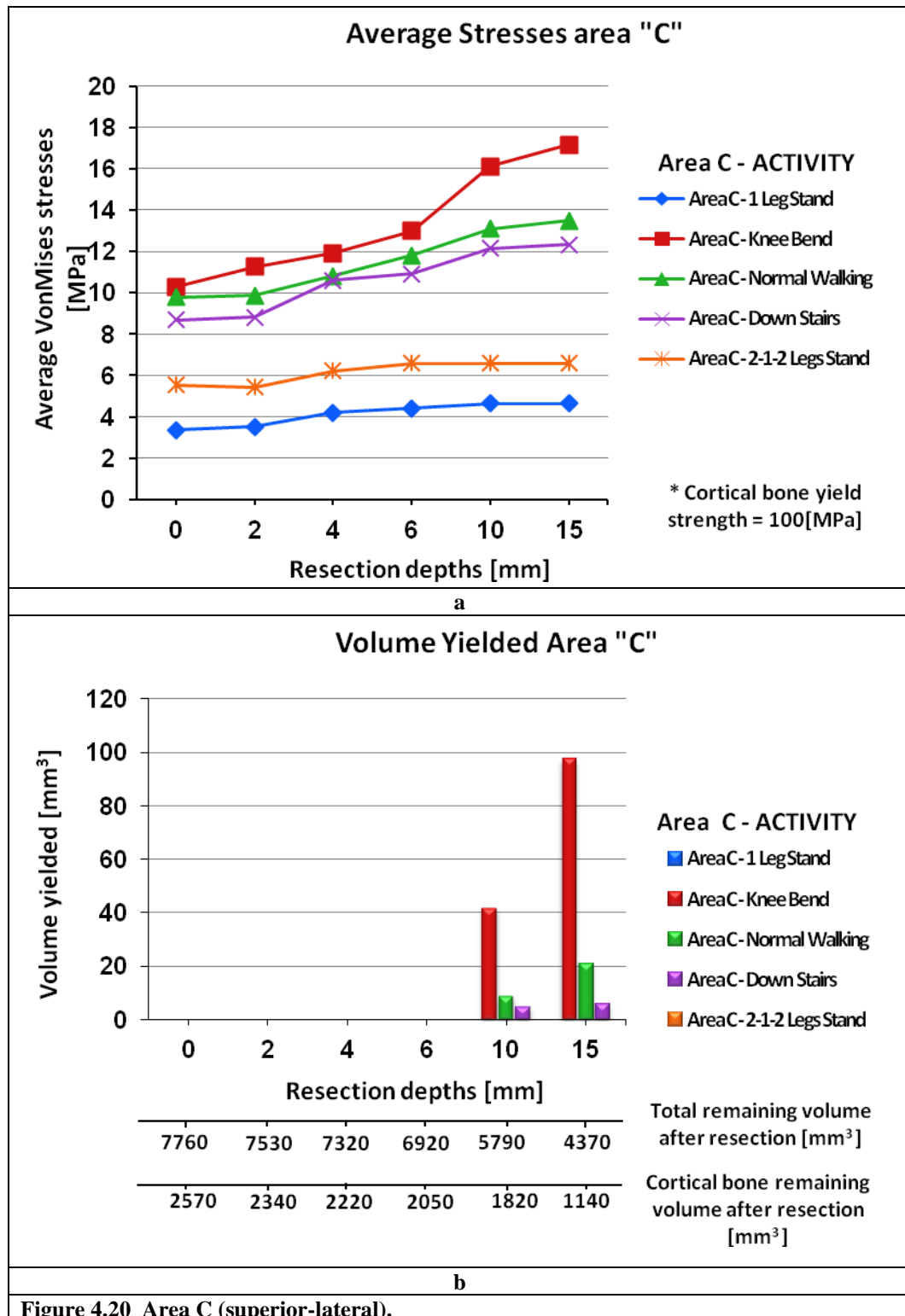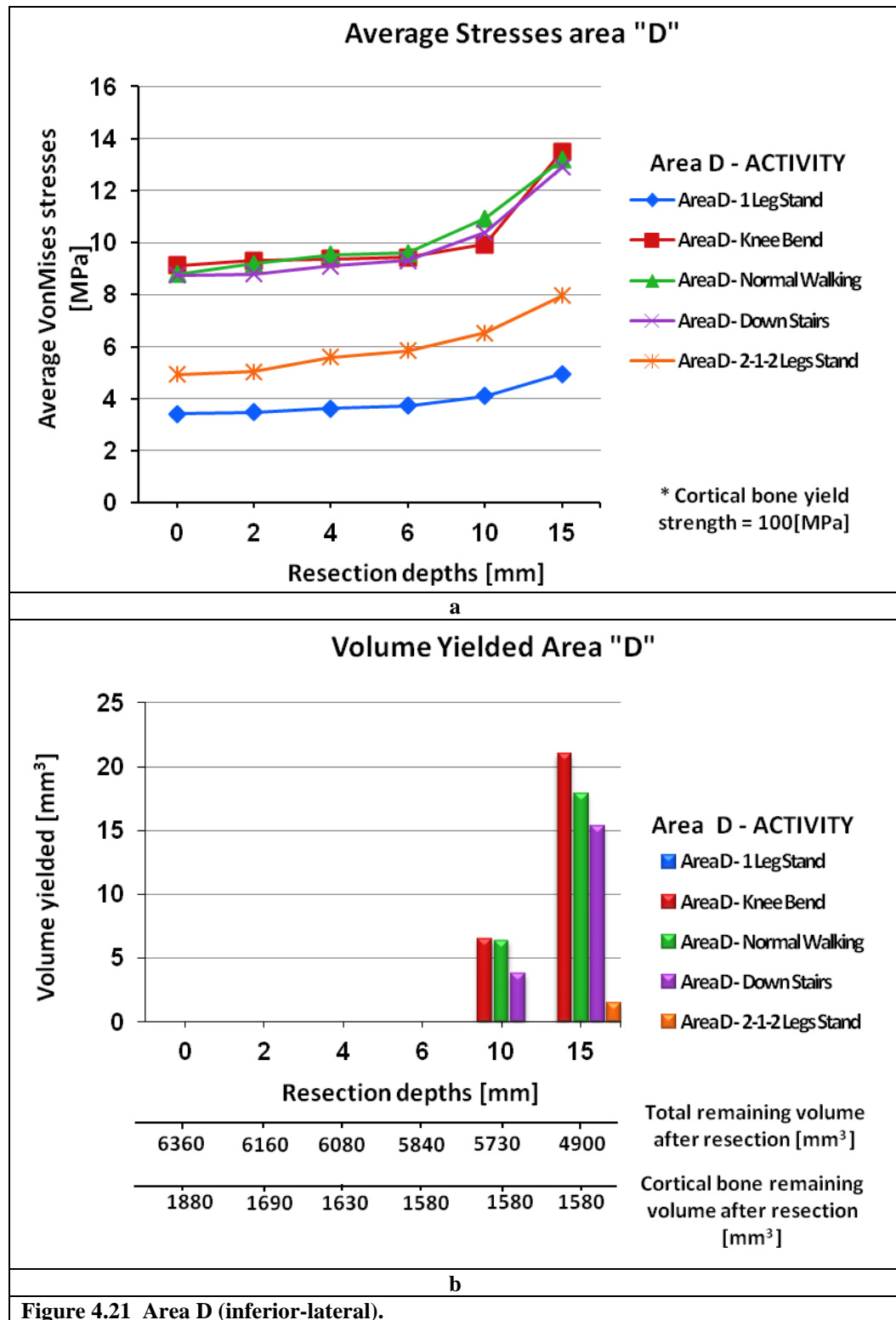
4.9.1 Contour Plot Analysis

Figure 4.22 illustrates an example of the von Mises stress distribution in the femoral head and neck for the knee bend activity at resection depths equivalent to ≥1/3 the diameter of the neck. At a resection depth of ≈1/3 the diameter of the neck (10 mm), the stress reached the yield point in the resection region, and over a small portion of the neck (depicted in red). As resection depth increased to 1/2 the diameter (15 mm) the yielded area expanded to the neck region surface and internally in the cortical bone which means that the elements in the neck region reached the elastic limit, so that the deformation will be permanent and possible failure may occur.

Frontal view / Frontal Cut view	Resection Depths	
	≈ 10 mm	≈ 15 mm
Stress von Mises		
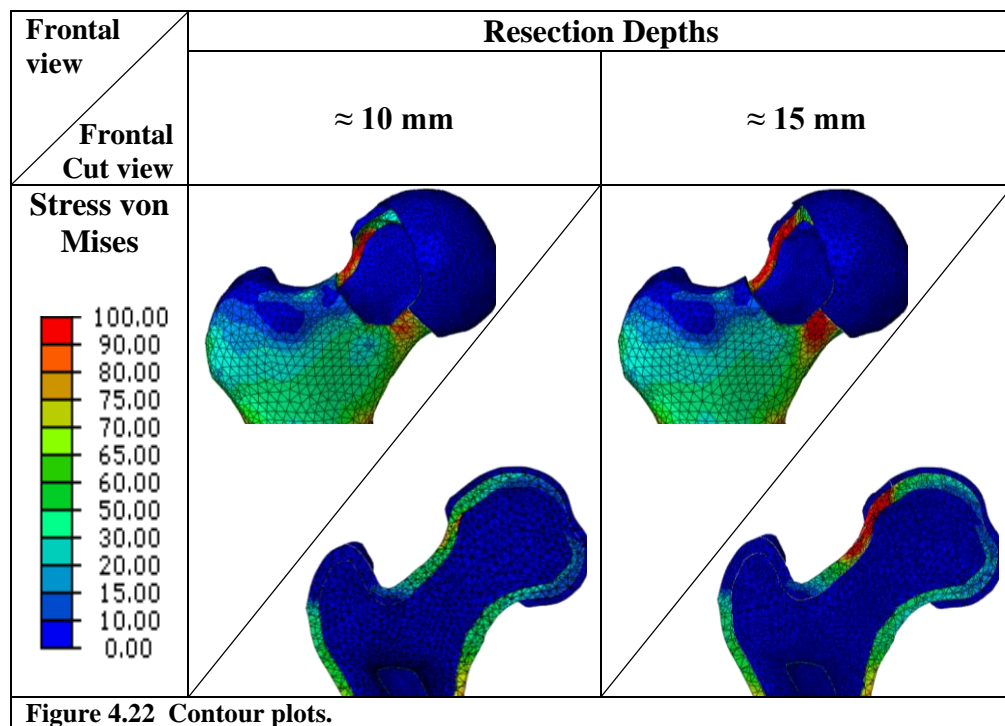
Figure 4.22 Contour plots.

The general yield pattern suggests that for resections depths of 1/3 and 1/2 of the neck diameter, fracture is likely in the resected area expanding to the femoral neck. The results presented above in addition to the occurrence of femoral fractures after osteochondroplasty for FAI, were the main reasons to then proceed with a detailed analysis of failure after femoral osteochondroplasty for FAI, considering different resection depths and bone quality properties. This failure analysis is reported in the following Chapter.

CHAPTER V: FAILURE ANALYSIS FOLLOWING OSTEOCHONDROPLASTY

5.1 Introduction

As discussed in the previous chapter, femoral osteochondroplasty is frequently performed as the surgical treatment for cam-type FAI and although femoral neck fracture is recognized as a potential post-operative complication of osteochondroplasty for FAI, little information is available as to what constitutes a safe depth of resection.

5.2 Failure analysis following osteochondroplasty

To date, only two studies have attempted to provide some insight and guidance to this problem. First, an experimental cadaveric study [3] reported that at resection depths of 30% of the diameter of the femoral neck and greater, the energy required to produce fracture reduced significantly, causing a modification to the failure pattern and second, the results from the previously described finite element study (Chapter IV) [100] which suggested that the resection depth should be kept to less than 1/3 of the diameter of the neck in order to ensure integrity of the femoral head and neck.

Hip fracture is considered to be one of the most serious potential consequences of osteoporosis [132-134]. Whilst it is acknowledged that bone quality is an important factor in addition to resection depth and the degree of post-operative weight bearing in femoral neck fractures following hip osteochondroplasty [102, 105], the effect of osteoporosis on the risk of postoperative fracture is currently unknown. The authors of the experimental study into the effect of the size of resection depth [3] noted that due to the age of the cadaveric samples used, it was likely that the specimens had a higher degree of osteoporosis than the bone of younger patients which would thus reduce their loading bearing capacity, suggesting that the results underestimated the upper limit of what can be considered to be a safe resection depth.

Even though it is relatively uncommon to perform osteochondroplasty for FAI on older patients it is sometimes appropriate and in addition osteoporosis is being found increasingly in younger patients [135, 136]. Recently, recommendations have

suggested that bone mineral density scans should be considered in cases where osteopenia or osteoporosis is suspected in patients undergoing this type of surgery [105].

The aim of the study described in this chapter was to develop a 3D finite element model using CT scan data from a patient with a cam-type femoroacetabular impingement to investigate the association between osteoporosis and both the mechanism and risk of femoral neck fracture after femoral osteochondroplasty. Two resections depths were considered in addition to the intact, non-resection case, for both healthy and osteoporotic bone scenarios, with the hip model subjected to average and high peak loads corresponding to the "descending stairs" activity. The hip model was also subjected to the loads corresponding to "stumbling", an activity that has been determined to result in high contact forces. Osteoporotic bone material properties were considered and results were compared to those obtained for healthy bone. A quasi-brittle damage plasticity material formulation was employed in the Abaqus FE analysis software to provide an in-depth evaluation of fracture risk.

5.2 Methods

Three 3D finite element models of the proximal femur were developed to analyze two resection cases and the non resection case. Models were created using CT scan data from a patient with a prominent cam-type femoroacetabular impingement. The CT scan data were imported into ScanIP® to obtain a 3D surface. It was then exported to PowerSHAPE Pro® enabling a solid model to be produced. The solid model was read into the Abaqus CAE 6.10-1® for assembly, virtual resection development, mesh generation and subsequent analysis as previously described in Chapter IV (Section 4.4.1). Models were analysed considering healthy and osteoporotic bone material conditions and were subjected to three significant loading conditions.

5.3 Geometry

As described in Chapter IV, a methodology is followed to obtain the geometries for the models, starting with Scan IP®, passing through PowerSHAPE Pro® and concluding in

Abaqus CAE®. However, for the failure analysis some improvements to the resection tool used for the stress analysis described in the previous chapter were required.

5.3.1 Bones

The construction of the bone geometries was previously described in Chapter IV (Section 4.4.1).

5.3.2 Cartilages
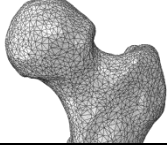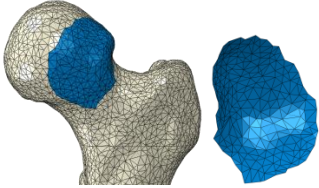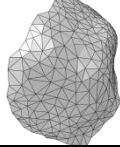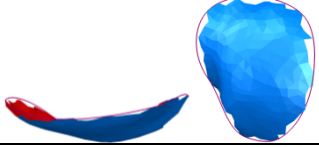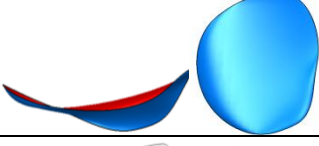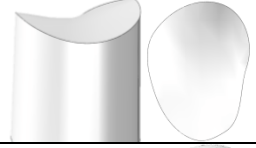
The construction of the bone geometries was previously described in Chapter IV (Section 4.4.2).

5.3.1 Resection Tool

Due to the fact that the use of the "Initial RT" led to irregular resections as previously described in Chapter IV (Section 4.4.3), an "improved" resection tool was developed to perform the virtual resections in the failure analysis as illustrated in Table 5.1. The new resection tool was created to facilitate the production of smooth resections thus avoiding the formation of irregular edges which can cause mesh irregularities and result in unrealistic stress concentrations when a structure is analysed. Starting from the same area selected by the surgeon (Steps 2-3), the construction of the RT was improved by creating a curve from several of the outer points of the selected area in order to make a smooth surface, which covered all the area selected by the surgeon in the model, and avoided the irregular edges produced by the triangular surfaces (Steps 4.1 and 4.2). This approach allowed the use of the design tools in Abaqus CAE® in case any modification was needed (Steps 5-6). As with the "Initial RT", it is essential to finish and assemble all geometries involved in the non-resection model in Abaqus CAE®, before creating the "Improved RT".

The "Improved RT" resulted in a smooth and regular resection and consequently a homogeneus mesh in the resection area, which led to the avoidance of stress concentrations and a reduction in the computation time required for the FEA. Figure 5.1 shows the steps used to perform a virtual resection with the "Improved RT" in the femoral head-neck junction.

Table 5.1 Process to create the RT.

Step	Improved RT
1. Import geometry from ScanIP®. ***Abaqus CAE®***	
2. Simulate the virtual osteochondroplasty (triangular surfaces selected by the surgeon). 3. Eliminate outer resection area surfaces. Export. ***Abaqus CAE®***	
4. Import the resection area ***PowerSHAPE Pro®***	
4.1. Create a 3D curve to include the outer limits of the resection area. ***PowerSHAPE Pro®***	
4.2. Create a surface from the curve. ***PowerSHAPE Pro®***	
5. Extrude the surface, convert it to a solid part and export as IGES file (RT). ***PowerSHAPE Pro®***	
6. Apply rounding tools. ***Abaqus CAE®***	
Software used during the step.	

Before virtual resection	RT	Bone - RT	After virtual resection

Figure 5.1 Volume removal in Abaqus CAE (Improved RT)
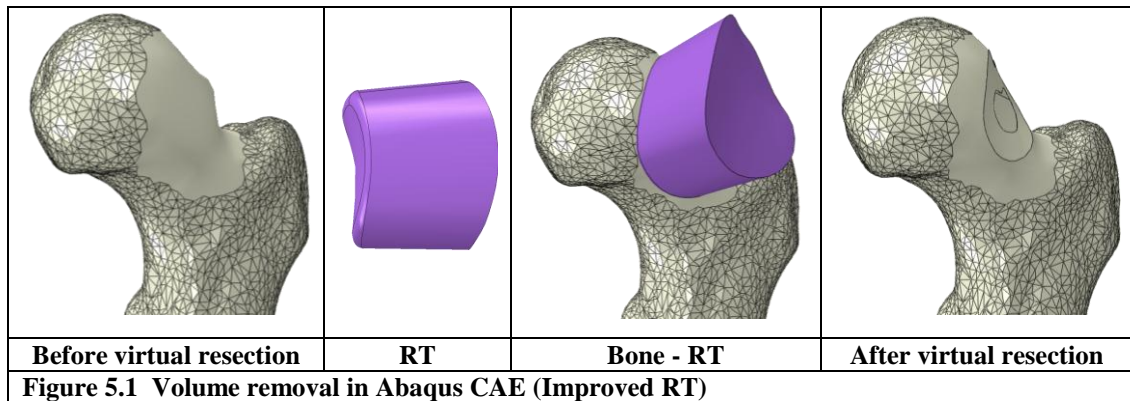
Two virtual resections were performed on the model and the shape of the resection area was considered as the maximum extent of the impingement zone as described in Chapter IV (Section 4.4.3). The "Improved RT" was used to perform the resections following the methodology described in Chapter IV (Section 4.4.5. The maximum impingement zone defined by the CT scans was considered to define the outer limits of the resection in both cases. One was a "normal" case of resection, considering only the sculpting of excess bone on the femoral head-neck junction, resulting in a resection depth of 6 mm or 18% of the overall femoral neck diameter. The second resection was considered a "critical" case, performed to a depth of 12 mm or 36% of the neck diameter. Figure 5.2 illustrates the two virtual osteochondroplasty and non resection models used for the present analysis.

0 mm	6 mm	12 mm

🟥 **Cortical bone**
🟦 **Trabecular bone**
⬜ **Cartilage**
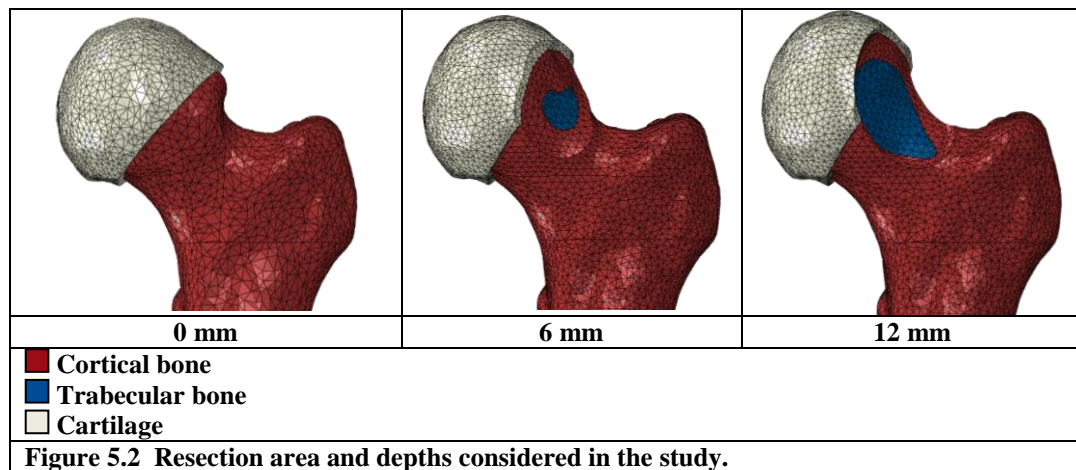
Figure 5.2 Resection area and depths considered in the study.

5.4 Material Properties

It is widely recognized that the material properties of bone change with age. The elastic modulus of human femoral cortical bone has been reported to reduce by 1-2% per decade after 35 years of age [137, 138]. Similarly, trabecular bone mass starts to decrease between the ages of 20 and 40 by around 6-8% per decade [139]. A common approach used by researchers to simulate the effects of osteoporosis in numerical models of the femoral head neck is to reduce the elastic modulus of both the cortical and trabecular bone by a percentage compared to 'normal' values [130, 131, 140].

For the analysis of the fracture mechanism in osteoporotic and non-osteoporotic bone after femoral osteochondroplasty for FAI, both cortical and trabecular bone were

assumed to be brittle materials and so the behaviour was modelled as elastic-plastic but in a complex mode. In addition, the values of density were included, since this variable is very important in the analysis of osteoporosis.

Density and elastic modulus for healthy bones were taken from the literature [57, 95, 121, 141-143] and were related by using the equation:

$$E = a\rho^{b} \tag{7}$$

Where E is the Young's modulus of the material; ρ is the apparent density and, a and b are constants dependant of the type of bone. For cortical bone $a = 2065$ and $b = 3.09$, whereas for trabecular bone $a = 1904$ and $b = 1.64$ [125].

Young's modulus for osteoporotic bone was estimated by reducing the healthy values for cortical and trabecular bones by 32% and 66%, respectively [130, 131, 144, 145]. The reduction of cortical properties is related to the experimental work from Dickenson *et al.*[127]*,* who obtained the mechanical properties of femoral cortical bone from normal subjects and subjects with osteoporosis. For the osteoporotic patients (average age 81 years) the average modulus of elasticity was determined to be around 32% less than the 'normal' value for a young adult, this value represents the reduction of 32% of the value utilised in the literature. Regarding trabecular bone, it has been reported that the reduction of 66% in the elastic modulus corresponds to an elderly osteoporotic patient [131]. This proportion is based on the relation between density and elastic modulus of the trabecular bone and the 8% of bone mass loss in the trabecular bone per decade [139].

The reduced Young's modulus values for cortical and trabecular bone employed in order to simulate the effects of osteoporosis were used in the equations above to obtain corresponding densities. Table 5.2 shows the variables used to define the elastic material behaviour of bone and the variations between healthy and osteoporotic cases.

Table 5.2 Elastic material properties used in the failure FEA [127, 130, 144, 145].

	Cortical bone		Trabecular bone	
	Healthy	**Osteoporotic**	**Healthy**	**Osteoporotic**
Density ρ **[t/mm^3]**	1.98e-9	1.75e-9	4.3e-10	2.2e-10
Young's modulus E **[MPa]**	17,000	11,560	477	162
Poisson's ratio	0.3	0.3	0.3	0.3

The material formulation employed for the analysis assumes a non-linear stress-strain relation and considers the evaluation of fracture by employing the theory of isotropic damaged elasticity combined with isotropic tensile and compressive plasticity, to define a failure envelope that encompasses cracking in tension and crushing in compression [146].

Plastic properties were defined following a Damage Plasticity Model (DPM) based on the stress-strain curves for cortical and trabecular bone [82, 147]. DPM is a predefined material formulation in Abaqus CAE® used to describe the plastic behaviour of quasi-brittle materials such as concrete or bones.

DPM is capable to model quasi-brittle materials in different structures based in the characteristic inelastic behaviour of these materials. Firstly, DPM requires defining as a linear-isotropic the elastic behaviour of the material, whereas the plastic behaviour is represented by considering the concepts of isotropic tensile and the compressive plasticity of the material [118].

DPM assumes the tensile cracking and the compressive crushing as the main failure mechanisms, so that the evolution of the fracture is referred to the tensile (ε_t^{pl}) and compressive (ε_c^{pl}) plastic strains, which are known as independent hardening variables. These variables direct the propagation of yielded material and the decrement of the elastic stiffness [118].

The relationship between the stress and the tensile (ε_t^{pl}) and compressive (ε_c^{pl}) plastic strains, is defined based on the stress-strain curves for uniaxial tension and

compression respectively. Abaqus CAE® converts the uniaxial stress-strain curves by using a scalar degradation variable into plastic-strain curves. This degradation variable goes from 0 for the undamaged material to 1 for completely damaged [118].

Healthy bone stress-strain curves were taken from the literature and osteoporotic bone curves were obtained by reducing the corresponding stress values by 32% for cortical and 66% for trabecular bone. Figure 5.3 shows the stress-strain curves used in the analysis corresponding to healthy and osteoporotic bone for both cortical and trabecular bone.

Figure 5.3 Stress-strain curves. (a) Cortical bone; (b) Trabecular bone.
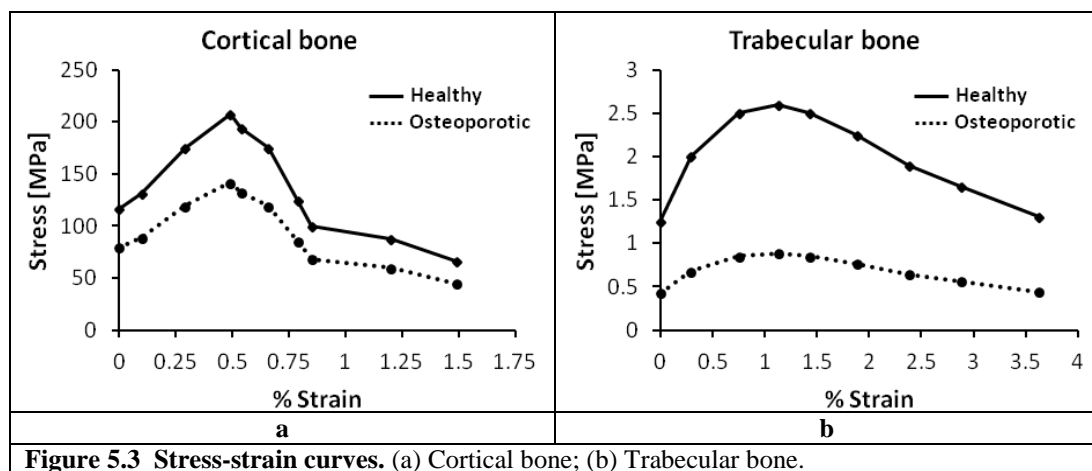
5.5 Boundary Conditions

A section of the hemi-pelvis including the acetabulum was generated and inserted in the models to transmit the joint loads to the femoral head. A "Tie" constraint in Abaqus CAE 6.10-1® was used to define the interaction between the femoral head and acetabulum, ensuring that adjacent nodes underwent the same displacement. In order to enable the effective transfer of the load to the femoral head whilst avoiding local stress concentrations, a "Rigid body" constraint was established on the hemi-pelvic bone [100]. The bottom surfaces of the proximal femoral segment were fixed in all directions for displacements and rotations. Figure 5.4 illustrates the boundary conditions used for the failure analysis.

Fixed surfaces	Concentrated force on femoral head / Contact interface
Bottom surfaces fixed in all directions	**Concentred forces**

Figure 5.4 Boundary conditions for the failure analysis.
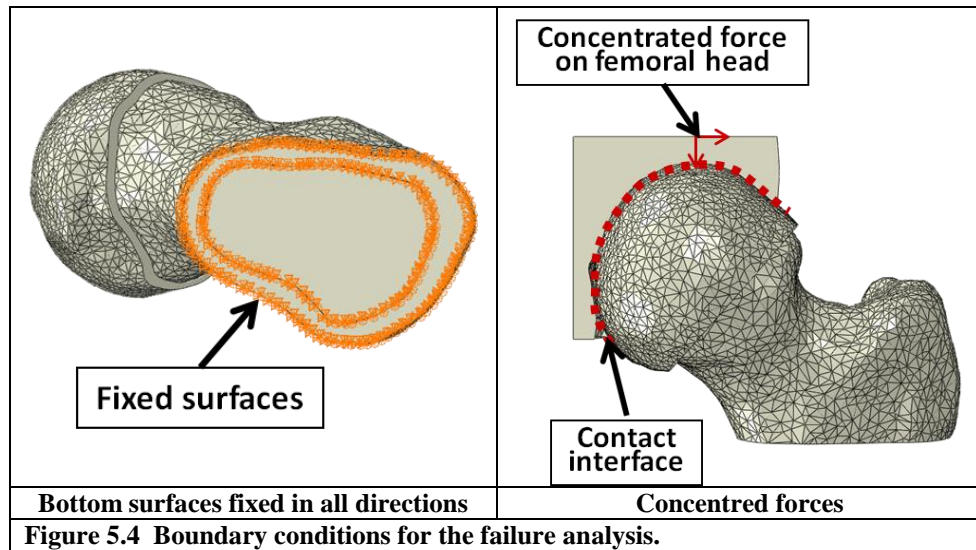
Three loading variations were applied in the models. The "average peak load" and "high peak load" derived from the "descending stairs" activity were applied [148]. The "average peak load" corresponds to the forces acting in a subject of body weight of 750 N. The "high peak load" acts in a subject of body weight of 1000 N. The forces applied in the third loading case corresponded to those derived from the "stumbling" activity, calculated under the assumptions of the "high peak loading" scenario.

Table 5.5 shows the component and resultant forces corresponding to the three loading cases considered in the models [148]. The loads were applied incrementally up to 100% of the resultant forces shown in Table 5.3.

Table 5.3 Forces considered in the models

	Peak contact forces			
Activity	**Resultant Force F [N]**	**F_x [N]**	**F_y [N]**	**F_z [N]**
Descending stairs (Average)	2000	370	292	-1944
Descending stairs (High)	4200	776	613	-1082
Stumbling	11000	2462	1523	-10607

5.6 Mesh Sensitivity Analysis

A mesh convergence analysis was undertaken in order to ensure accurate results could be obtained without requiring excessive computational resources. The analysis consisted of taking the intact, non-resection model and comparing the average von Mises stress in the femoral neck for three mesh densities: coarse, medium, and fine meshes, consisting of 79,245, 183,152, and 928,248 elements respectively. The medium density mesh was chosen since the results changed by <0.5% between this and the fine mesh. Table 5.4 shows the number of elements employed in the three models, the intact (non-resection) and 6 and 12 mm resection models.

Table 5.4 Number of elements employed in the models.

Tetrahedral Elements			
Model/Resection depth [mm]	**Cortical**	**Trabecular**	**Total**
0	45,207	137,945	183,152
6	77,201	132,056	209,257
12	74,846	129,442	204,288

5.7 Validation of the Model

Validation of the model was performed by comparing predictions with the experimental results from the cadaveric investigation described briefly in Chapter 4, that involved testing to fracture 15 pairs of human femurs [3]. One femur from each pair was resected with depth being varied; the remaining femur from each pair was left intact as a control. The mean age of the cadaveric specimens was 79 years. The osteoporotic intact non-resection model was subjected to loading and boundary conditions representative of those used in the cadaveric study. The neck stiffness predicted by the model was compared with the mean neck stiffness of the control group from the experimental study[3]. The model predicted a neck stiffness of 604 N/mm which compares favourably with that obtained from the cadaver study, which was 686 N/mm [100].

5.8 Results

The results from the model include tensile and compressive damage output variables which refer to specific material degradation at the micromechanical level indicating that the bone has undergone permanent damage. Permanent material damage was taken as indicating the initiation of fracture in the models. The volume of bone damaged in tension and in compression was calculated for both cortical and trabecular bone in the femoral head-neck shaft region. Here the focus is on analysing the volume of bone damaged in tension as it is recognized that bone is weaker in tension than in compression as previously described in Chapter III (Section 3.3.5) [87, 95, 147].

The results from the model indicate that no permanent material damage occurs at any resection depth in the trabecular and cortical bone in both the non-osteoporotic and osteoporotic cases for the "descending stairs" activity when subjected to "average" peak loading. However, when subjected to "high peak" loading, although no material damage was indicated in the cortical bone at any resection depth, material damage was registered at resection depths of 6 and 12mm in the osteoporotic bone and at 12 mm in the non-osteoporotic trabecular bone indicating an increased likelihood of fracture occurring.

Figure 5.5 shows the damage volume in tension in non-osteoporotic and osteoporotic trabecular bone for the different resection depths in the "descending stairs" scenario for the "high peak loading" case. The results are shown at loading increments up to 100% of the applied load. It can be seen upon inspection of this figure that no material damage is present in the non resection cases.

In the case of the "normal" resection depth (6 mm), damage occurs in 10% of the osteoporotic trabecular bone volume at 100% of the "high peak load" but not in the non-osteoporotic, healthy trabecular bone. For the "critical" resection depth (12 mm), a level of material damage is recorded for both non-osteoporotic and osteoporotic trabecular bone. Damage occurs in approximately 4% of the non-osteoporotic trabecular bone when 100% of the "high peak load" is applied. In the osteoporotic

case, 15% of the trabecular bone volume shows damage at around 60% of the "high peak load" rising sharply to 54% at full load.

00_ RES = Non-resection model → Remaining volume 27,511 mm^3
06_RES = 6 mm resection depth → Remaining volume 27,398 mm^3
12_RES = 12 mm resection depth → Remaining volume 25,820 mm^3
GDS-HL = Going Downstairs activity subjected to High Loading

Figure 5.5 Fractured volumes in trabecular bone for all resection depths and both healthy and osteoporotic properties during "Going downstairs-High loading" activity.

In the "stumbling" scenario damage was registered in both trabecular and cortical bone types. Figure 5.6a shows the volume damage in the cortical bone for the "stumbling" scenario. No material damage is indicated in the healthy, non-osteoporotic bone for all resection depths considered. However, a level of damage is present in the osteoporotic cortical bone at all resection depths, including the non resection case. The volume of cortical bone damage is 5% at 100% loading for the non resection scenario, rising to 6% and 10% for the "normal" and "critical" resection depths respectively. Damage is initiated at around 82% of the full load in both resection cases and at approximately 92% load in the non resection simulation.
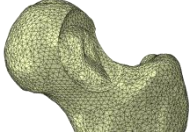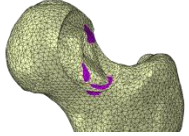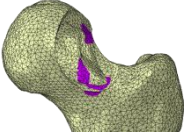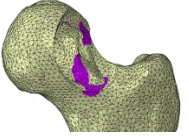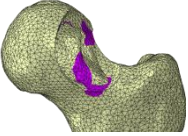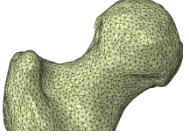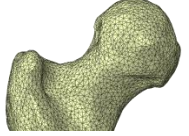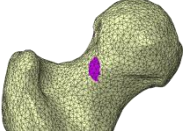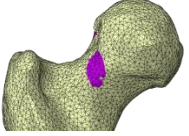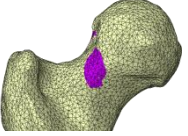
In the trabecular bone for the "stumbling" scenario, damage was observed in both healthy and osteoporotic bone at all resection depths including the non-resection case, as can be seen in Figure 5.6b. In the non-resection scenario, 6% of the non-

osteoporotic trabecular bone volume indicated material damage at 100% load compared to 34% for the osteoporotic bone case. The percentage of bone damage then increased with resection depth in both the non-osteoporotic and osteoporotic trabecular bone scenarios. At a resection depth of 6 mm, the bone damage volume was 44% and 49% in healthy and osteoporotic trabecular bone respectively. The bone damage percentage at a resection depth of 12mm was 70% for both non osteoporotic and osteoporotic trabecular bone. Figure 5.6b also indicates that damage starts to occur in the osteoporotic trabecular bone at lower loads than in the corresponding healthy, non osteoporotic bone cases.

Volume of bone fractured during "Stumbling" in osteoporotic and healthy cortical bone

00_ RES = Non-resection model → Remaining volume 20,112 mm3
06_RES = 6 mm resection depth → Remaining volume 18,940 mm3
12_RES = 12 mm resection depth → Remaining volume 16,824 mm3

a

Volume of bone fractured during "Stumbling" In trabecular bone

00_ RES = Non-resection model → Remaining volume 27,511 mm^3
06_RES = 6 mm resection depth → Remaining volume 27,398 mm^3
12_RES = 12 mm resection depth → Remaining volume 25,820 mm^3

b

Figure 5.6 Fractured volume in (a) cortical and (b) trabecular bone for all resection depths in both healthy and osteoporotic bone during "Stumbling" activity.

5.8.1 Contour Plot Analysis

Analysis of the damage distribution pattern in the cortical osteoporotic bone of the proximal femur at a resection depth of 12 mm for the "stumbling" activity simulation suggests that damage will initiate in the resection area at around 80% of the loading, as shown in Figure 5.7. As load increases further, damage expands over the resection area and transversely through to the posterior area of the femoral neck. A similar analysis in the trabecular bone indicates that damage initiates here in the inferior-medial area of the resection at 25% of the loading. Damage on the posterior surface of the neck is confined to a few small areas which start to appear at 90% load.

	Fracture pattern during "stumbling"				
	Osteoporotic cortical bone – 12 mm resection depth				
Anterior view					
Posterior view					
	0 % Load	**≈80 % Load**	**≈90% Load**	**≈95 % Load**	**100 % Load**

Figure 5.7 Fracture pattern on cortical osteoporotic bone for 12mm resection depth during "Stumbling" activity.

CHAPTER VI: NOVEL TECHNIQUE ASSESSING THE OSTEOCHONDRAL INJURIES

6.1 Introduction

The equivocal presentation of femoroacetabular impingement (FAI) results in frequent incorrect diagnosis and inappropriate treatment procedures. An important symptom for the diagnosis of FAI is the reduction in the Range of Motion (RoM) of the hip as a result of the abnormal morphology of the bones. In cam-type impingement, the presence of excess bone in the antero-superior region of the femoral head-neck junction reduces the RoM particularly in flexion and internal rotation movements [11, 19, 22, 25, 37].

This chapter describes the development of a novel methodology to investigate the reduction in the internal rotation RoM in hips with cam-type impingement and to locate the areas of impingement associated with the osteochondral injuries. This methodology consists of two main stages in order to provide insight and guidance regarding the surgical procedures that should be performed to alleviate the impingement.

The first stage of the presented methodology consists of an analysis of internal rotation of movement to elucidate the actual RoM of abnormal hips. This analysis investigates the reduction in the internal rotation RoM in hips with cam-type FAI and identifies the impingement areas in order to indicate the least invasive possible surgical intervention required to alleviate the impingement.

The second stage involves the development a virtual osteochondroplasty procedure. This new virtual osteochondroplasty procedure is based on the impingement areas obtained from the first stage. Following the virtual resection it is then possible to measure to what degree RoM has been improved in the hip model, with the aim of obtaining a RoM close to that which is typical of a normal hip.

The accuracy of the virtual osteochondroplasty methodology is validated by taking an existing FAI diagnosed hip. A model of the FAI hip is created and an analysis undertaken to identify the impingement areas. These results are then used to guide

the virtual osteochondroplasty procedure. RoM is assessed following the virtual osteochondroplasty procedure and this is compared with that obtained from a model of the same hip created from CT scan data taken after an actual osteochondroplasty had been performed on the patient where the resection area and depth had been established in the usual way using the skill and experience of the surgeon.
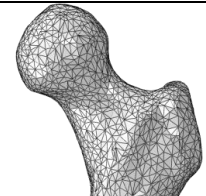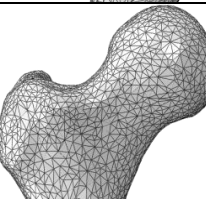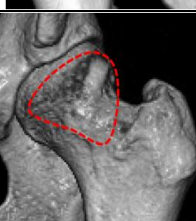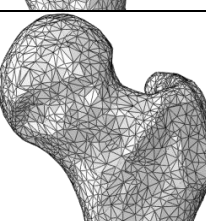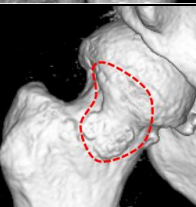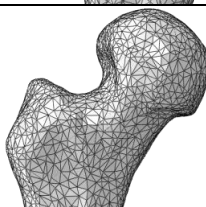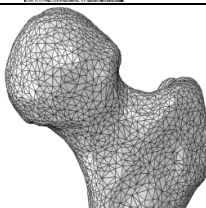
6.2 Analysis of Range of Motion

Femoral osteochondroplasty is a surgical procedure commonly used to alleviate the problems associated with FAI including the reduction of the range of motion (RoM) of the hip and osteochondral injuries associated with FAI. Although several studies of FAI are documented in the literature, the challenge remains to address the effect of the morphological abnormalities on the mechanical behaviour of the joint elements in FAI [3, 8, 9, 11, 13-15, 19-25]. Further information has been previously described in Chapter II (Section 2.7).

6.2.1 Methods – Range of Motion Analysis

Five 3D finite element models were created from CT scan data of hips, denoted P-I, P-II, P-III, P-IV and P-V. The first model was from a subject with normal hip morphology whereas the last four models were created from CT scans of hips from patients exhibiting cam-type FAI. Figure 6.1 compares the CT scan visualization (3D) with the final geometries obtained for the modelling in Abaqus CAE 6.10-1®.

The Abaqus 6.10-1® FE software package was employed for the analysis with the surface to surface contact option within Abaqus utilised to identify any interaction between the femoral head and acetabulum.

Patient	CT Scan (3D view)	Abaqus 3D Model
*P-I		
P-II		
P-III		
P-IV		
P-V		

P-I→ Normal morphology model
P-II to P-IV →Cam-type morphology model
*Plane X-rays

Figure 6.1 Patient geometries.

The five hip models were subjected to conditions to reproduce the internal rotation movement of the hip at different stages of flexion (0º, 45º, 90º, 110º). Figure 6.2 illustrates the initial positions of flexion considered for each patient.

0º Flexion	45º Flexion	90º Flexion	110º Flexion

Figure 6.2 Pre-flexion positions to perform the internal rotation RoM analysis.
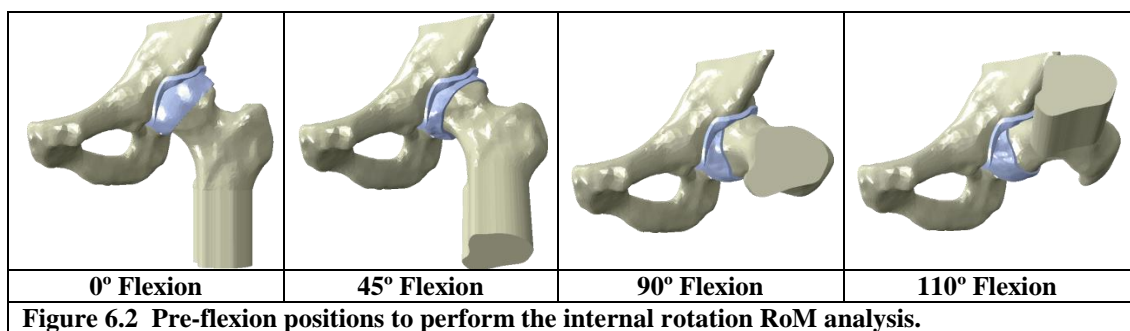
At each flexion position the hip models underwent internal rotation, up to a maximum rotation of 55°, until a collision between the femoral head-neck junction and the acetabulum was detected. At this point, rotation was ceased and RoM, contact (impingement) area and position were calculated.

To facilitate flexion and internal rotation movements in the hip models, cartesian coordinate systems were defined Since the CT scans were taken in supine position in 0° of flexion, a default coordinate system defined by the Abaqus software was employed in this position, with its origin at the centre of rotation of the femoral head. A second 'flexion' coordinate system, also having its origin at the femoral head rotation centre, was then defined, with one axis corresponding to the mechanical axis (the axis defined by the line running from the femoral head to the knee), a second axis running in the medial-lateral direction and the third, anterior-posterior. Flexion was then simulated by rotating the femoral head by the required angle (0°, 45°, 90°, or 110°) about the medial-lateral axis of the "flexion" coordinate system. The "flexion" rotation system was then itself rotated by the flexion angle about the medial-lateral axis in order to create a third coordinate system that could be used to facilitate the internal rotation. The femoral head was then rotated about the vertical axis of this third coordinate system.

The internal RoM was estimated by obtaining the positions of the femur prior to the start of the internal rotation and once rotation had been stopped, when impingement was detected. The angles of rotation were estimated by using the equation:

$$\theta = \cos^{-1} \frac{\overrightarrow{AB_i} \cdot \overrightarrow{AB_f}}{\left\| \overrightarrow{AB_i} \right\| \cdot \left\| \overrightarrow{AB_f} \right\|} \tag{8}$$

Where, $A(x, y, z)$ is the point obtained by projecting the rotation centre of the hip to a plane parallel to the internal rotation movement, $B_i(x_i, y_i, z_i)$ is the point where the rotations were applied before the analysis and $B_f(x_f, y_f, z_f)$ is the same point after the completion of the analysis, as illustrated in Figure 6.3.

Figure 6.3 Points to calculate the internal rotation RoM.
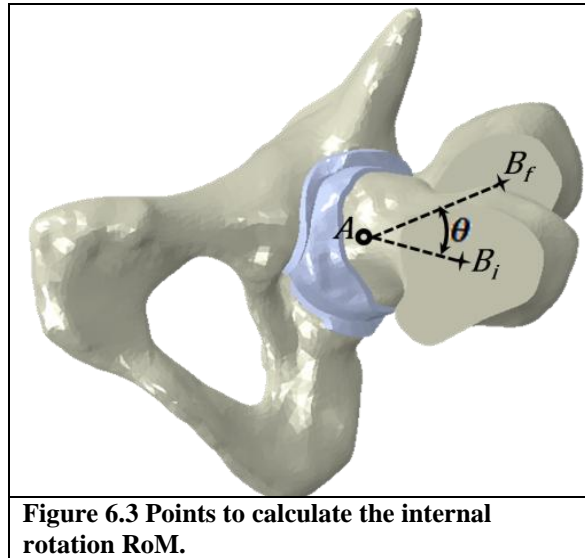
The impingement area was calculated from the coordinates of the nodes that were identified as being on the surfaces of the femoral epiphysis and acetabulum that had come into contact during internal rotation in the four flexion positions considered.

In more detail, the process used to determine the contact area was as follows:

1. For each hip model, the nodes on the surfaces of the femoral epiphysis and acetabulum that had come into contact during the internal rotation in the four flexion positions were identified as shown in Figure 6.4a.
2. MATLAB R2010a® (The MathWorks Inc., Natick, MA.) code was developed to locate the coordinates of the contact nodes in the input data of the model in Abaqus CAE 6.10-1®, as shown in Figure 6.4b.
3. The set of the coordinates located in step 2 was imported into SolidWorks® (Figure 6.4c) where they were used to create a 3D surface in order to facilitate calculation of the impingement area (Figure 6.4d). The 3D surfaces were saved as IGES files to be used in the subsequent virtual ostreochondroplasy analysis described in Section 6.10.

a	**b**	**c**	**d**	**e**

Figure 6.4 Steps to obtain the contact area (Model P-V). (a) Contact area after internal rotation movement in four different pre-flexion positions (Abaqus CAE 6.10-1®); (b) Node coordinates of the contact areas (MathLAB®); (c) Cloud of points (SolidWorks); (d) 3D surface (SolidWorks); (e) Contact area over solid model (PowerSHAPE PRO®).
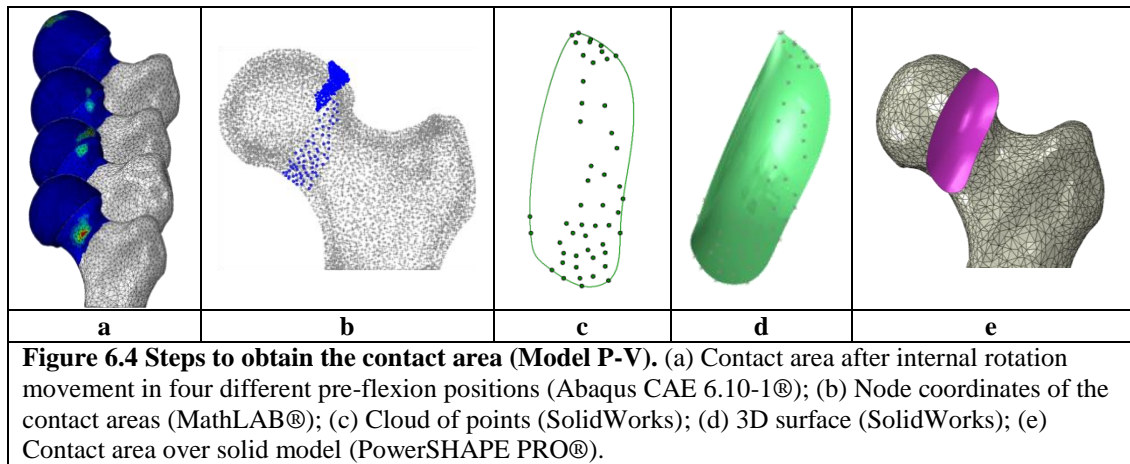
6.2.2 Geometry

The methodology described in Chapter IV was employed to obtain the 3-dimensional bone geometries of the hips for use in the analysis. As the CT scan data did not provide sufficient information for constructing the cartilage geometry accurately, it was created using a method that utilised the cortical bone geometry and assumed a uniform cartilage thickness. The process used to construct the cartilage geometries included in the models was as follows:

1. Preliminary cartilages were obtained in ScanIP® following completion of the bone segmentation process by expanding the corresponding image mask of the cortical bone, as illustrated in Figure 6.5a.

2. The expanded geometries were imported into PowerSHAPE Pro®, enabling modification using Boolean operations to facilitate the removal of virtual volumes between the preliminary cartilages and the bone geometries (Figure 6.5b).

3. The modified geometry was then imported into Abaqus 6.10-1® where final, minor modifications were made to ensure a smooth, realistic, accurate representation was achieved that could be subsequently meshed and analysed whilst avoiding the generation of unrealistic stress concentrations. Figure 6.5c shows the final cartilages used in the models.

Preliminary cartilages	Cortical bone + Preliminary cartilages	Final cartilages
a	b	c

Figure 6.5 Construction of the cartilages. (a) Preliminary cartilage masks (ScanIP®); (b) Cortical bone plus expanded geometries (PowerSHAPE PRO®); (c) Final cartilages (Abaqus CAE 6.10-1®).
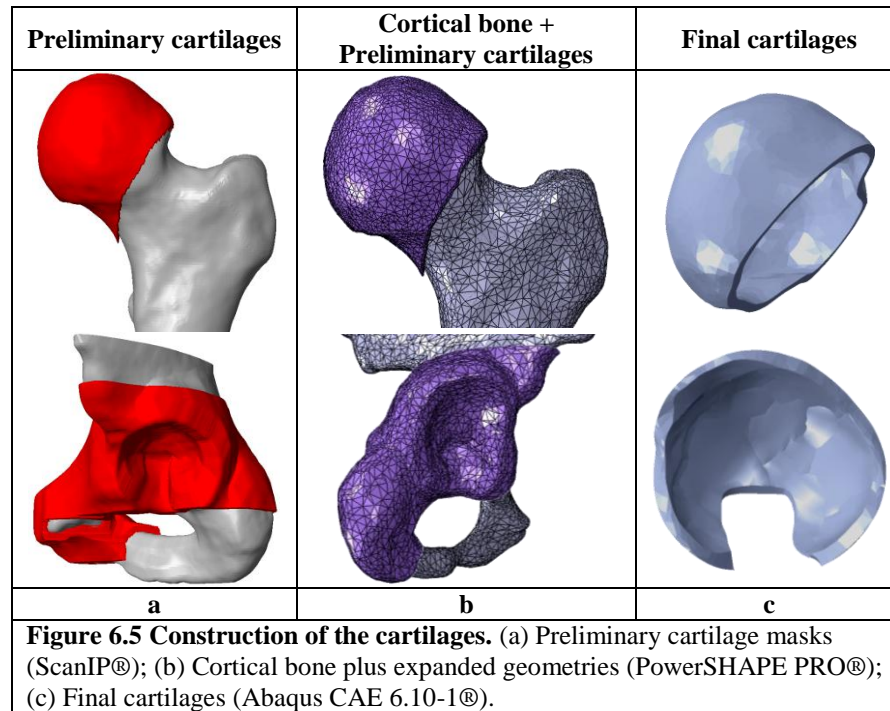
In order to avoid differences in the models due to variations in the CT scan data of each patient, the upper section of the pelvic bone was cut and the bottom surface of the cortical bone was extruded to create a tubular geometry to represent the femoral diaphysis in order to reduce the geometric variables in the models and make them more reproducible. Figure 6.6 illustrates the modifications made to the geometries to avoid differences between the models.

Figure 6.6 Homogeny of the models. (a) CT scan dimensional variations; (b) Models after dimensional modifications.

117
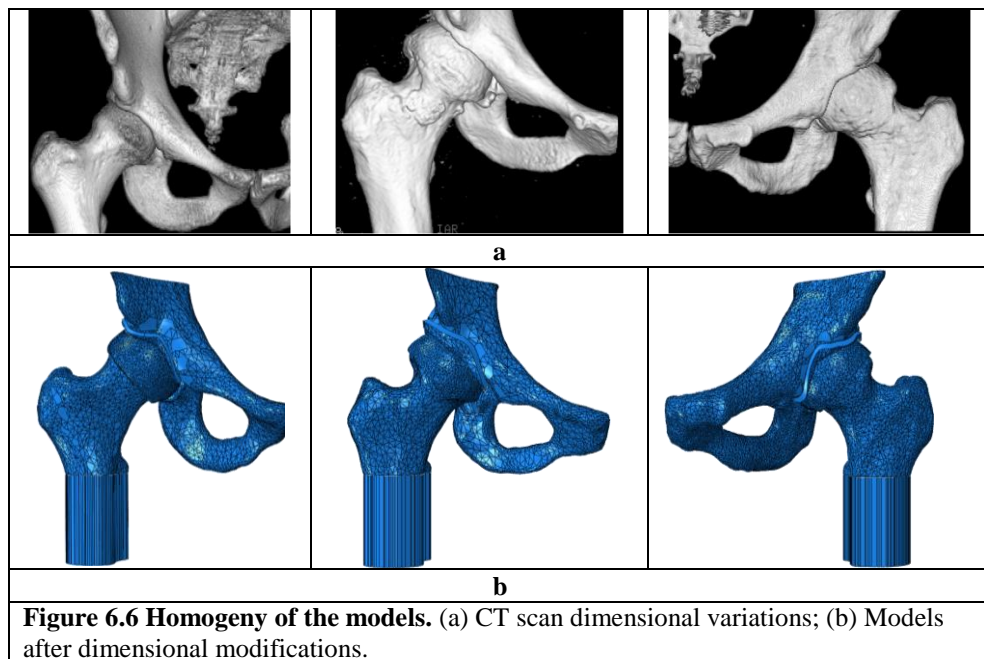
6.2.3 Material Properties

The cartilage, cortical, and trabecular bone were assumed to exhibit elastic-plastic isotropic behaviour and the material properties are listed in Table 6.1 [54, 87, 95, 121, 126, 127, 141-143].

Table 6.1 Elastic material properties for the two types of bone and cartilage used in the models

	Cortical bone	Trabecular bone	Cartilage
Density, ρ [t/mm3]	1.98e-9	4.3e-10	1.3e-9
Young's modulus, E [MPa]	17,000	477	12
Poisson's ratio	0.3	0.3	0.4

6.2.4 Boundary Conditions

The flexion-internal rotation analysis model requires additional restrictions compared to the static analyses in order to provide the required stability for the joint during the movement, so capsular ligaments were included in the models. Ligaments were represented using spring elements distributed around the joint as illustrated in Figure 6.7. Distribution of the springs was based on the anatomical location of the ligaments as previously described in Chapter III (Section 3.2.4). Table 6.2 shows the stiffness and number of spring elements used for each ligament [149-151].

a	b
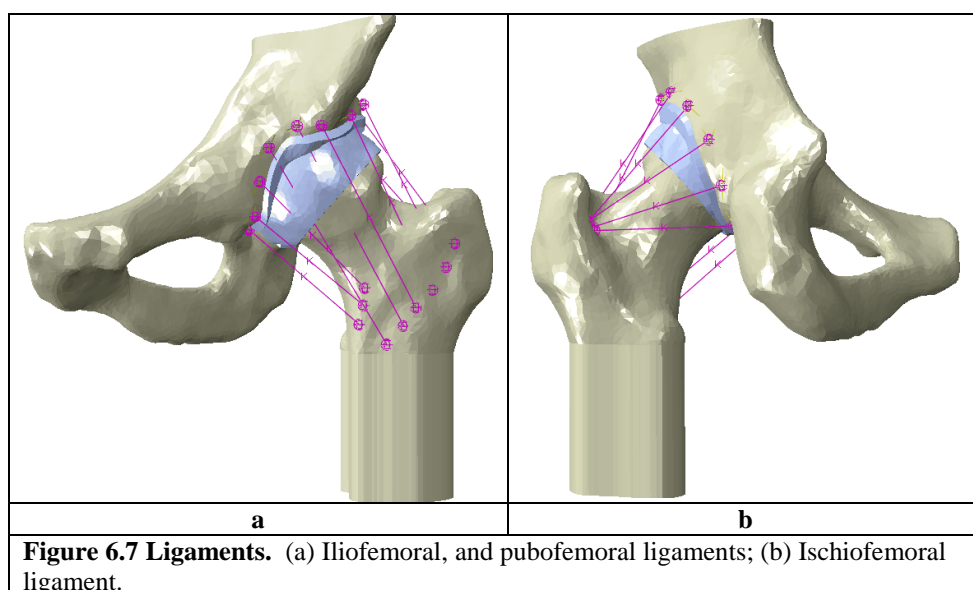
Figure 6.7 Ligaments. (a) Iliofemoral, and pubofemoral ligaments; (b) Ischiofemoral ligament.

Table 6.2 Stiffness of the ligaments.

Ligament	Stiffness [N/mm]	Stiffness per spring [N/mm]	Number of springs
Pubofemoral	36.9 ± 24.4	12	3
Iliofemoral	198 ± 60	33	6
Ischiofemoral	39.6 ± 24.4	9	4
Teres	68 ± 25	14	5

Full bonding was assumed at the interface between the cortical and trabecular bone and between the cartilage and cortical bone, as described in Chapter IV. The interaction between the acetabular and the femoral cartilage was modelled as frictionless surface to surface contact as the friction coefficient between cartilages is low ($\mu < 0.0025$) [95].

The centre of rotation of the femoral head was calculated by first fitting a circle to the head and then determining the intersection of the two perpendicular diameters [151, 152]. The centre of rotation was fixed with respect to displacements in all directions but free rotations were allowed about all axes. Figure 6.8 illustrates how the centre of rotation was located.

Fontal view	Transversal view	Sagittal view

Figure 6.8 Centre of rotation.
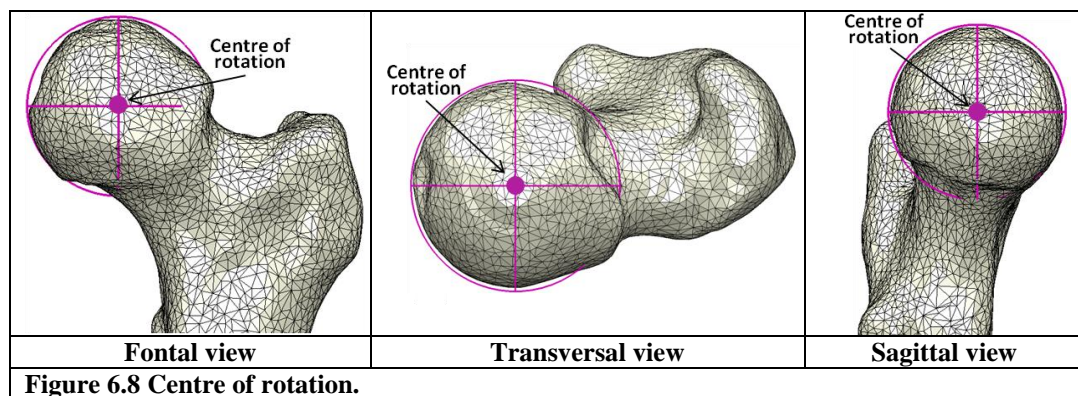
The top surface of the pelvis and 12 points of the medial zone were fixed, as shown in Figure 6.9.

119

Anterior view	Transversal view

Figure 6.9 Boundary conditions for the RoM analysis.
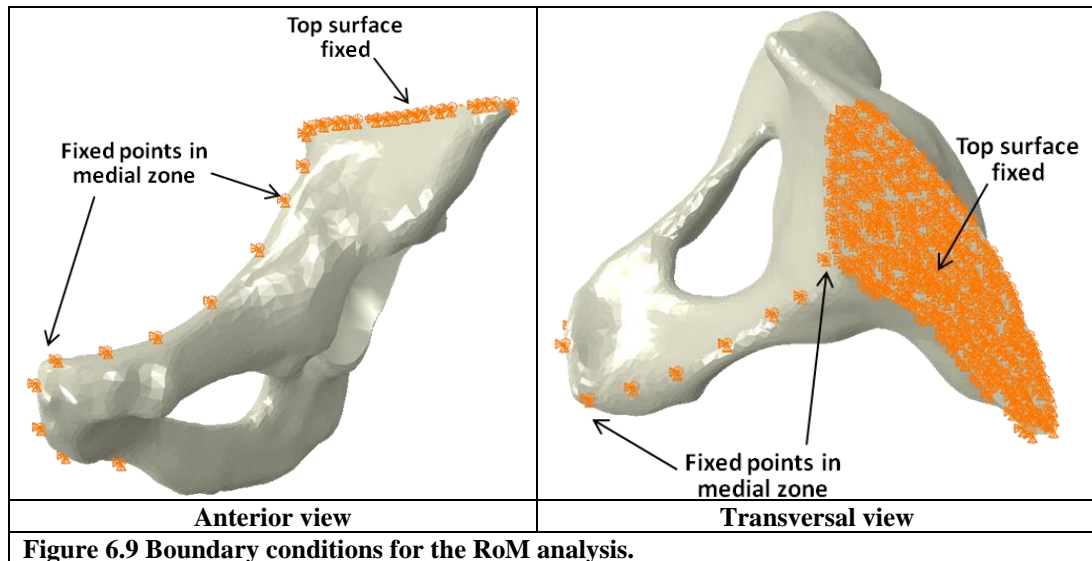
Because the CT scans were taken in a supine position, this position was assumed to correspond to 0º of flexion. Flexion and internal rotations were assigned to the tubular extrusion of the cortical bone which was considered to be a rigid body. The required motions were then applied to a reference point on the lower surface of the cortical bone, as shown in Figure 6.10.

a	b	c
Rigid body extrusion	Flexion	Internal rotation

Figure 6.10 Hip movement modelling.
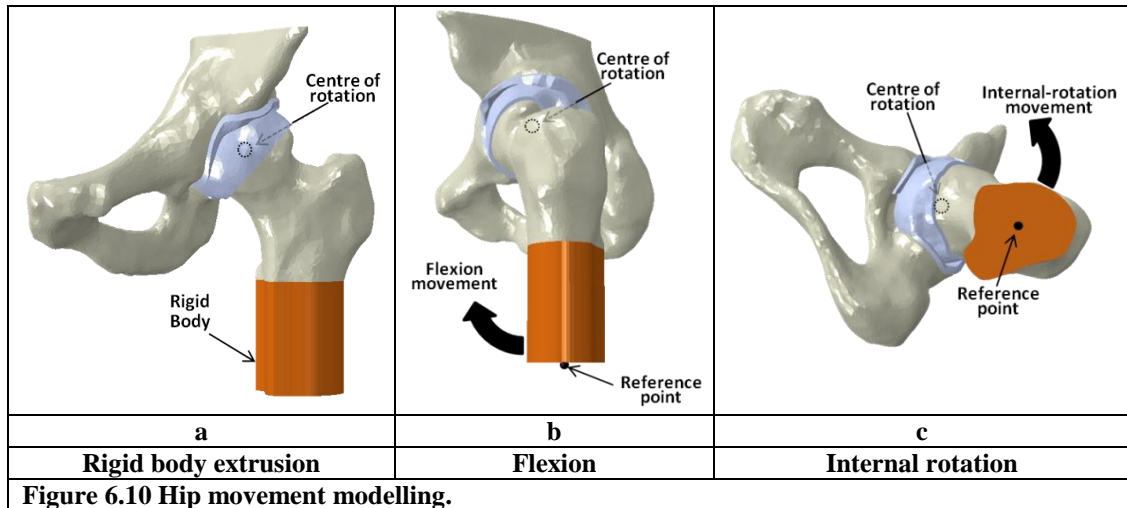
Movements were performed using the two auxiliary coordinate systems located at the centre of the femoral head. A Flexion Coordinate System (FCS) was defined based on the mechanical axis of the hip, which runs from the knee to the femoral head, having an angle of 3º with respect of the vertical line, as previously described in Chapter III.

The three perpendicular axes of the FCS run medial-laterally, anterior-posteriorly and over the mechanical axis as illustrated in Figure 6.11a. All the flexion movements were performed around the medial-lateral axis of the FCS.

The Rotation Coordinate System (RCS) and the FCS have in common the medial-lateral axis, however, the antero-posterior and the mechanical axes were rotated for each flexion position to keep their perpendicularity and their geometric location with respect to the femoral epiphysis.

Figure 6.11b shows the RCS used to analyse the internal rotation at 45° of flexion. Once the femur was rotated, the internal-rotation movement was defined around the mechanical axis of the RCS. Movements were determined by fixing the displacements in all directions and only allowing the rotation in the corresponding plane of the stage of flexion being analysed.

a	b

Figure 6.11 Flexion-internal rotation coordinate systems. (a) Flexion Coordinate System (FCS); (b) Rotation Coordinate System (RCS).
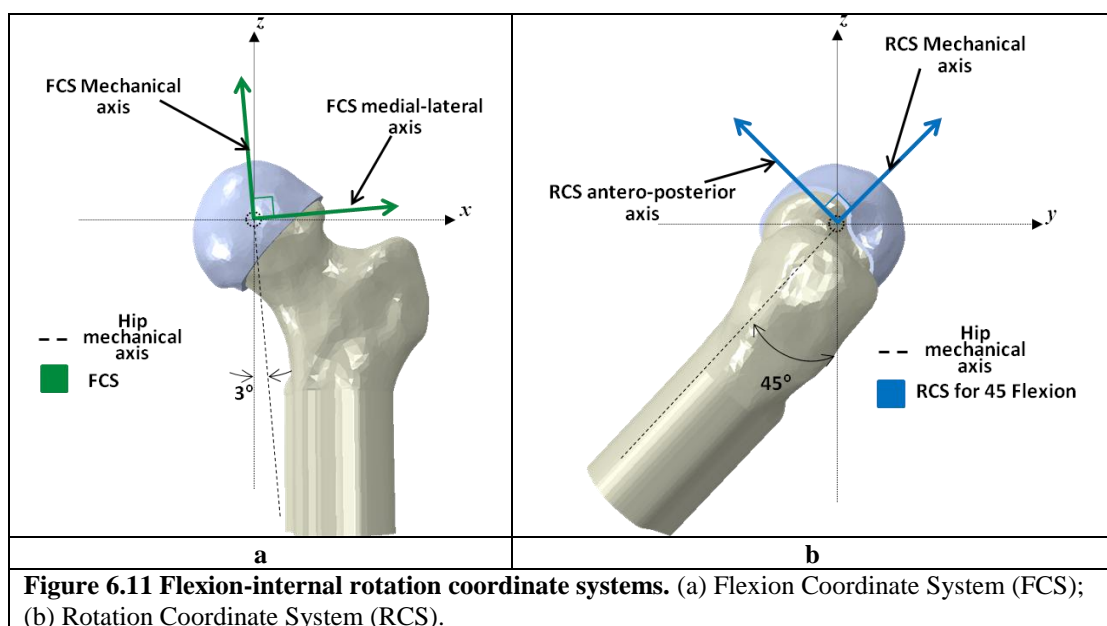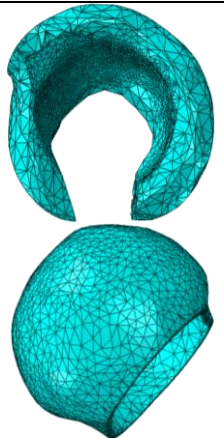
6.2.5 Mesh Sensitivity Analysis

Cortical and trabecular bone and cartilage geometry were meshed with linear, 4-node tetrahedral elements. Two-noded nonlinear tension-only spring elements were employed to represent the ligaments.

A mesh sensitivity analysis was performed in order to ensure model prediction accuracy was balanced against computational cost. The model of the hip from a

subject with normal hip morphology, P-I, was taken and mesh density varied. The mesh sensitivity analysis described in Chapter IV identified appropriate mesh densities for bone geometry. A new mesh sensitivity analysis was performed by varying the mesh density in the cartilages as impingement contact area and ROM were of primary concern in this research. Due to the nature of the analysis of the internal rotation movement it was essential to ensure accurate contact between cartilages because they are the surfaces in contact during the motion. So, average cartilage contact pressure and contact area was compared at three cartilage mesh densities (mesh 1: 37,780 elements, mesh 2: 193,729 elements, mesh 3: 976,205 elements) with the model subjected to the vertical component of the ground reaction force corresponding to a single leg stance applied to the pelvis [151]. The middle mesh density (mesh 2) was chosen because the difference in the results between the middle and finer mesh was <0.4%. Results from the cartilage mesh analysis are listed in Table 6.3

Table 6.3 Mesh convergence analysis for cartilages.

Mesh			
	Finer	**Medium**	**Coarse**
Number of elements	976,205	193,729	37,780
Computer time	72 hours*	8 hours	6 hours
Results variation — **Contact pressure**	----	0.4%	8.1%
Results variation — **Contact Area**	----	0.4%	9.4%
Not able to complete using desktop computer.			

Having established appropriate mesh densities, these were applied in the meshing of the cam-type FAI hip models, P-I, P-II, P-III, P-IV and P-V. Table 6.4 shows the number of elements employed in the models used in the RoM analysis.

Table 6.4 Number of elements employed in the models for the RoM analysis.

Model	Tetrahedral Elements			
	Cortical	**Trabecular**	**Cartilage**	**Total**
P-I	111,416	45,111	193,729	350,256
P-II	89,076	74,683	177,645	341,404
P-III	203,556	58,059	199,257	460,872
P-IV	104,786	56,867	174,478	336,131
P-V	184,290	79,584	182,183	446,057

6.2.6 Validation of the Model

The model was validated by comparing the RoM estimated from the patient who exhibited normal morphology (P-I) with those reported in the study by Tannast *et al.* [53]. Tannast *et al.* developed a computer-assisted method to estimate the RoM in FAI patients which they validated against the actual ROM from 27 (13 normal plastic and 14 fresh cadaveric) hips measured using a computer navigation system. Internal rotations at 90º of flexion were measured in the 27 hips. The RoM predicted for internal rotation at 90º of flexion from the P-V model was 24º which is in the range reported from the cadaver/plastic hip study, which was 23º-47º. The following section presents the results obtained from the RoM analysis.

6.2.7 Results – Range of Motion Analysis

For the purpose of analysing the results from study, the head-neck area (HN) was considered to be the region running from the level of the centre of the femoral head, through the femoral neck to the intertrochanteric line all around the bone, as illustrated in Figure 6.12. The average surface area of the HN is 3,600 mm^2,
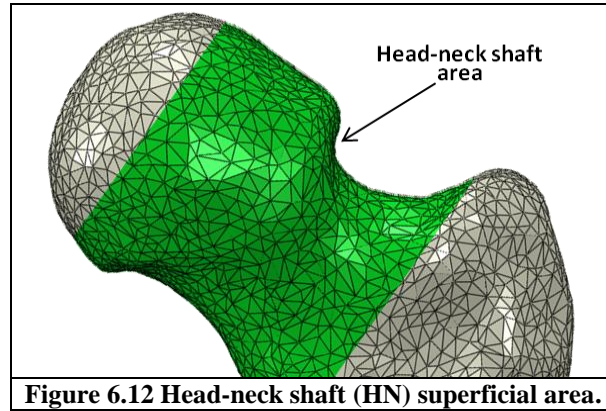
Figure 6.12 Head-neck shaft (HN) superficial area.

Figure 6.13 shows the locations on the femoral head-neck (HN) areas of the five hip models where contact occurred between the femur and acetabulum during internal rotation in the four flexion positions considered as predicted in the simulation. Also given in this figure is the magnitude of the impingement (contact) area for each hip, which is shown as a percentage of the total surface area of the femoral head-neck shaft region.

It can be seen upon inspection of Figure 6.13 that impingement occurs in the antero-superior area of the femoral HN region in all of the cam-type FAI hip models, with impingement area varying between 12% and 27% of the total HN surface area.
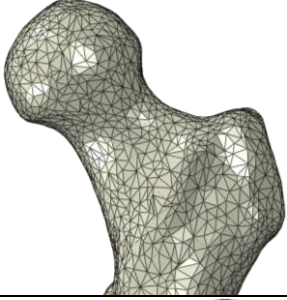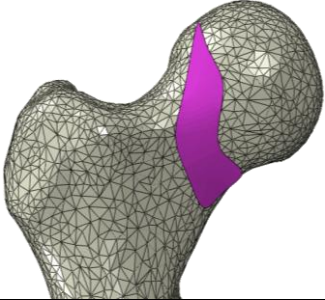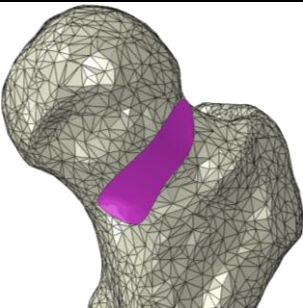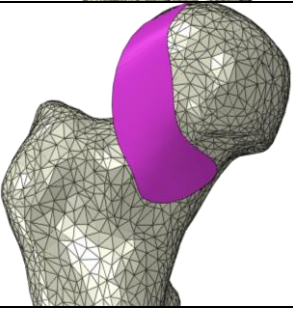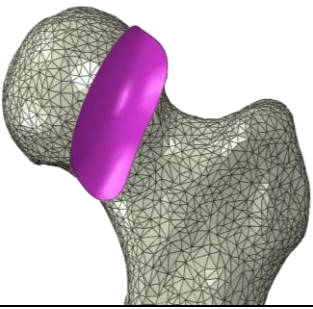
Location	Impinged area (% of HN)
	——
	465 mm^2 (13%)
	443 mm^2 (12%)
	980 mm^2 (27%)
	866 mm^2 (24%)

Figure 6.13 Impinged areas.

Figure 6.14 shows the maximum internal rotation (RoM) for the five hip models at the four flexion positions considered. The five hip models, P-I, P-II, P-III, P-IV and P-V, did not present any signs of impingement during the single flexion movements of 0°,45°, 90°, and 110° before the internal rotations were applied. At 0° flexion, none of the models predicted impingement during internal rotation up to the maximum rotation considered, which was 55°. However, at the 45°, 90°, and 110° flexion positions, impingement was predicted during internal rotation for all hip models, resulting in a reduction in RoM, and it can be seen from Figure 6.14 that RoM decreased as flexion angle increased. At 45° and 90° flexion the largest differences in RoM between the normal hip model (P-I) and the models of cam type FAI hips (P-II, P-III, P-IV and P-V) were recorded. At 45° flexion, the average RoM of the cam type FAI hips was 23.6° compared to 52.9° for the normal hip model, a reduction of 55%. At 90° flexion, the average FAI hip RoM was 7.4°, 69% less than the normal hip. The average FAI hip RoM at 110° of flexion was 4.4° compared to 6.2° for the normal hip of normal morphology.

P-I→ *Normal morphology model*
P-II to P-IV →*Cam-type morphology model*

Figure 6.14 RoM of internal rotation movement.
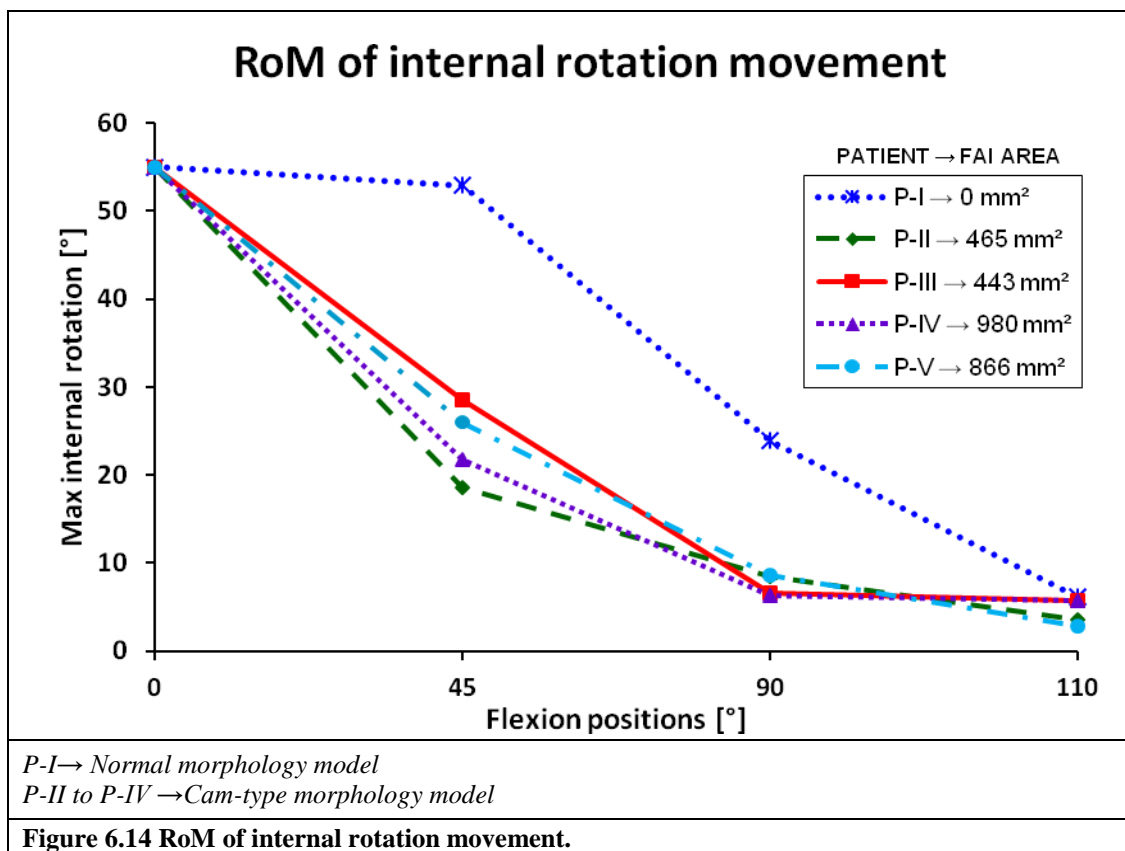
6.3 Development of the Virtual Osteochondroplasty

In Chapters IV and V, virtual osteochondroplasty was performed by removing a volume of bone from the femoral head in the models based on a resection area that was identified by a surgeon. Here, a similar methodology is used; however, the virtual resection is performed based on the areas of impingement calculated from the RoM analysis. The resulting virtual osteochondroplasty analysis described in this chapter involves the construction of a resection tool, the development of the virtual resection itself and finally the modelling of the flexion- internal rotation movement.

6.3.1 Methods – Development of the Virtual Osteochondroplasty

As described in "Methods – RoM analysis" (Section 6.2.1), 3D surfaces obtained from SolidWorks® which represent the impingement areas identified from the RoM analysis were saved as IGES files. Model P-V was taken and the 3D impingement surface obtained from the RoM analysis of the model was used to create an improved resection tool (RT) following the methodology outlined in Chapter V (Table 5.1). The 3D impingement surface was imported into PowerSHAPE Pro®, extruded and then finally exported so it could be imported into Abaqus CAE 6.10-1®. Figure 6.16 illustrates the process used to create the RT for the P-V model.

a	b	c

Figure 6.15 Resection Tool construction. (a) Cloud of points (SolidWorks®); (b) 3D surface (SolidWorks); (c) Solid Resection Tool (PowerSHAPE PRO®).
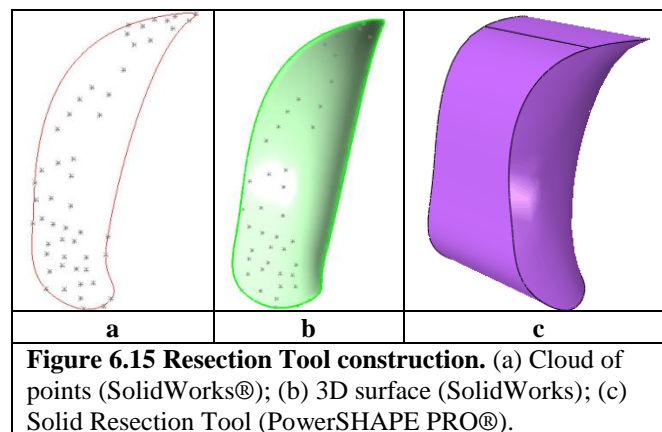
The second stage was to perform the virtual osteochondroplasty itself. The RT was imported into Abaqus CAE 6.10-1® and used to virtually resect hip model P-V; the resulting resected version of model P-V was denoted P-V_RT. The virtual osteochondroplasty was performed employing Boolean operations which facilitated the removal of the volume of the RT in the femoral HN as described in Chapter IV.

The process undertaken to perform the virtual osteochondroplasty is illustrated in Figure 6.17.
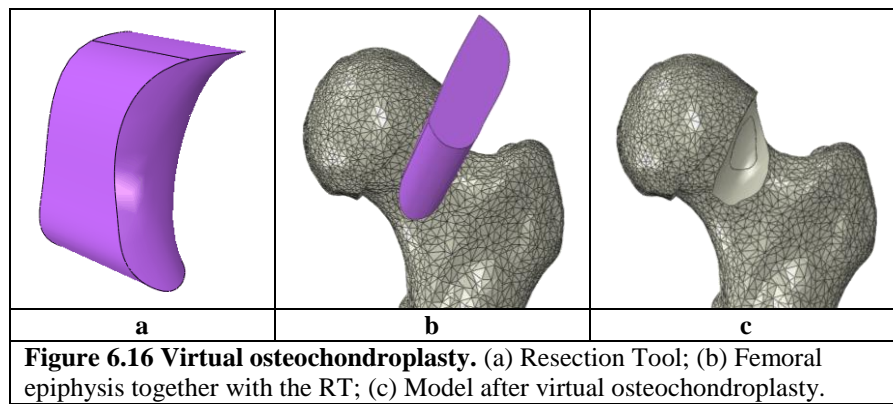
Figure 6.16 Virtual osteochondroplasty. (a) Resection Tool; (b) Femoral epiphysis together with the RT; (c) Model after virtual osteochondroplasty.

The P-V_RT model was then subjected to the flexion-internal rotation RoM analysis at the four stages of flexion previously mentioned (0º, 45º, 90º, 110º). The results from the analysis of the P-V_RT model were compared with the results obtained in the earlier RoM analysis for the same hip prior to the virtual resection being undertaken (model P-V).

Material properties and boundary conditions remained the same as in the original RoM analysis (Section 6.6). All geometries were meshed with linear, 4-node tetrahedral elements except the ligaments which were represented using two-noded nonlinear tension-only spring elements. Table 6.5 lists the number of elements employed in each model of the virtual osteochondroplasty analysis.

Table 6.5 Number of elements employed in the models for the virtual osteochondroplasty.

Model	Tetrahedral Elements			
	Cortical	Trabecular	Cartilage	Total
P-I	111,416	45,111	193,729	350,256
P-V	184,290	79,584	182,183	446,057
P-V_RT	184,812	78,433	181,569	445,030

6.3.2 Results - Development of the Virtual Osteochondroplasty

RoM predictions obtained for the FAI hip following virtual osteochondroplasty (model P-V_RT) were compared with the values obtained prior to resection (model P-V) and to those for the normal hip (model P-I). The results are shown in Figure 6.18 where upon inspection it can be seen that following the virtual resection, RoM increases significantly from pre-resection values to levels that are close to those of a normal hip.

P-I → Normal morphology model.
P-V → Cam-type morphology model.
P-V_RT → Cam-type morphology model after virtual osteochondroplasty.

Figure 6.17 RoM of internal rotation movement (pre and post virtual osteochondroplasty).
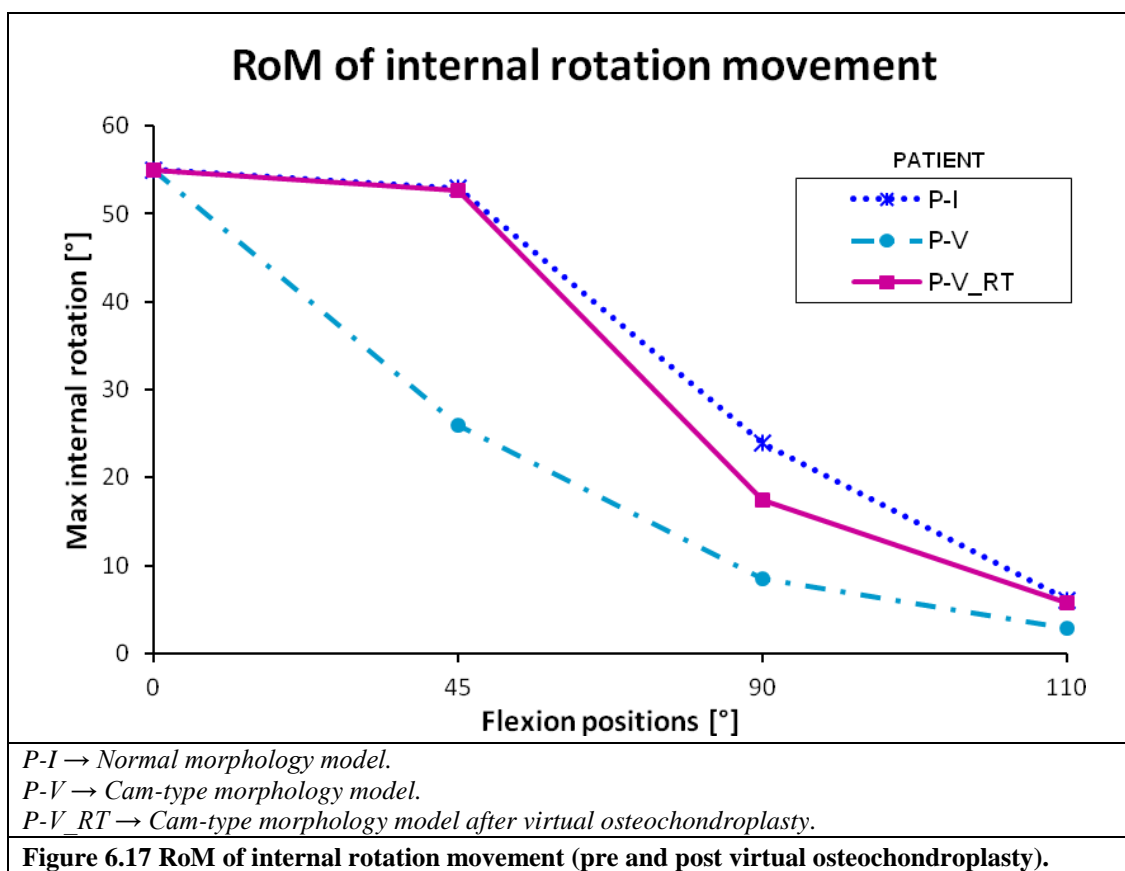
At 45° of flexion, RoM increases by 26.7° following the virtual resection to normal hip levels. At 90° of flexion, the virtual resection results in an increase in RoM of 8.9°, to a value 6.5° below that of the normal hip. At 110° of flexion, RoM increases by 3° to within 0.4° of that of the normal hip.

In summary, RoM increased following virtual osteochondroplasty from pre-resection values to levels similar to those of a normal hip without any sign of FAI occurring

during the simulation. Table 6.6 shows the principal characteristics of the model of the hip following the virtual resection.

Table 6.6 Status of the virtual osteochondroplasty model P-V_RT.

Model P-V_RT	
OUTER RESECTION AREA	866 mm^2
VOLUME BEFORE RESECTION (HNS)	43,356.43 mm^3
VOLUME AFTER RESECTION (HNS)	41,732.57 mm^3
VOLUME RESECTED	1619.86 mm^3
% VOLUME RESECTED	3.7 %
DEEPEST RESECTION POINT	6.42 mm

Since it has been demonstrated in the previous Chapters that the resections in the femoral head and neck should be kept <30% of the head-neck shaft diameter to ensure no damage occurs after surgical procedure [3, 100], the virtual resection in the model was performed within what can be considered to be the safe limits, as the resection depth was 6.4 mm or 21% of the head-neck shaft diameter at the deepest point.

6.4 Validation of the Technique

In this section a new model of a hip from an actual patient with FAI was created and the RoM predicted following application of the virtual osteochondroplasty methodology outlined in section 6.10 was compared with the results from a model of the same hip after an actual osteochondroplasty had been performed on the patient using a resection area and depth identified in the conventional way by a surgeon.

Model P-VI_PRE was constructed from CT scan data of the hip of a patient who presented a critical case of cam-type impingement prior to surgery. Model P-VI_POST was constructed from CT scan data of the same hip taken after the surgical procedure had been performed. Figure 6.19 shows the geometries obtained from the pre and post surgical procedure data for patient P-VI.

	Pre surgery	Post surgery
Anterior view		
Superior view		

Figure 6.18 Geometries from pre and post surgical procedure data for patient P-VI.
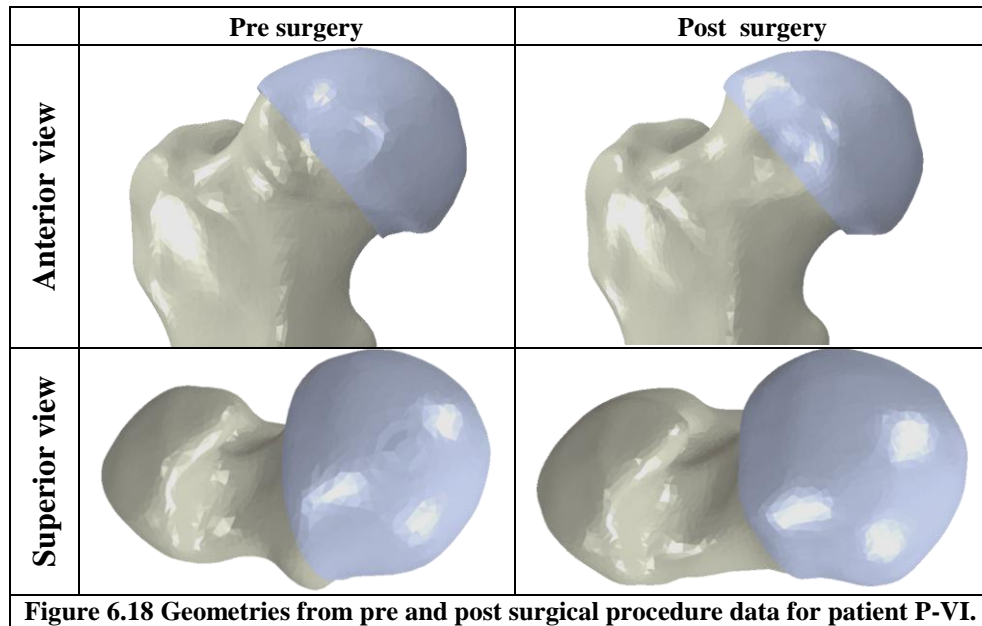
6.4.1 Methods – Validation of the Technique

Models P-VI_PRE and P-VI_POST were then both run under the previously defined conditions of flexion in order to determine the flexion-internal rotation RoM, prior to and following the actual osteochondroplasty.

Model P-VI_PRE was then used as the starting point for implementing the virtual osteochondroplasty technique.

The impingement area in model P-VI_PRE was calculated for the same four flexion-internal rotations cases. The coordinates of the nodes in contact were obtained in MATLAB R2010a® and exported into SolidWorks® to obtain the impingement area in order to perform the virtual resection as described in "Methods – RoM analysis" (Section 6.3). Geometry modifications were performed in model P-VI_PRE by using the RT derived from the calculated impingement area as described in "Methods – Virtual osteochondroplasty" (Section 6.11). The resulting new model was named P-VI_RT and was subjected to the same conditions of flexion and internal rotation in order to measure the RoM.

Material properties and boundary conditions remained the same as in the RoM analysis (Sections 6.5 and 6.6). Table 6.7 shows the number of elements employed in each model used.

Table 6.7 Number of elements employed in the models for the technique implementation.

Model	Tetrahedral Elements			
	Cortical	**Trabecular**	**Cartilage**	**Total**
P-I	111,416	45,111	193,729	350,256
P-VI_PRE	259,499	69,004	260,602	589,105
P-VI_POST	309,836	105,824	187,811	603,471
P-VI_RT	254,954	78,295	250,806	584,055

6.4.2 Results – Validation of the Technique

The abnormal morphology of the P-VI_PRE model resulted in a large reduction in the internal rotation ROM compared to that of a normal hip. This particular morphology has two implications. Firstly, the model was unable to reach the intended 110º of flexion because the impingement occurred at 106º and secondly, during the internal rotation, impingement was encountered even at 0º of flexion.

RoM increased significantly following actual osteochondroplasty (model P-VI_POST) as expected, to the extent that the maximum internal rotation angles achieved at 0º and 110º of flexion exceeded those of the hip of normal morphology (model P-I) without any sign of impingement. Following the virtual osteochondroplasty (Model P-VI_RT) impingement was also avoided and RoM increased notably from pre- virtual osteochondroplasty levels. In addition, the maximum internal rotation angle achieved at 110º of flexion was greater than that recorded for the normal hip (model P-I).

Figure 6.20 shows the ROM calculated in the pre, and post osteochondroplasty models, the model subjected to virtual osteochondroplasty, and the normal hip model, P-I.

| P-I→ Normal morphology model. |
| P-VI_PRE → Cam-type morphology model (Pre surgical procedure). |
| P-VI_POST → Cam-type morphology model (Post surgical procedure). |
| P-VI_RT → Cam-type morphology model after virtual osteochondroplasty. |

Figure 6.19 Maximum degrees of internal rotation (pre, post and virtual osteochondroplasty).
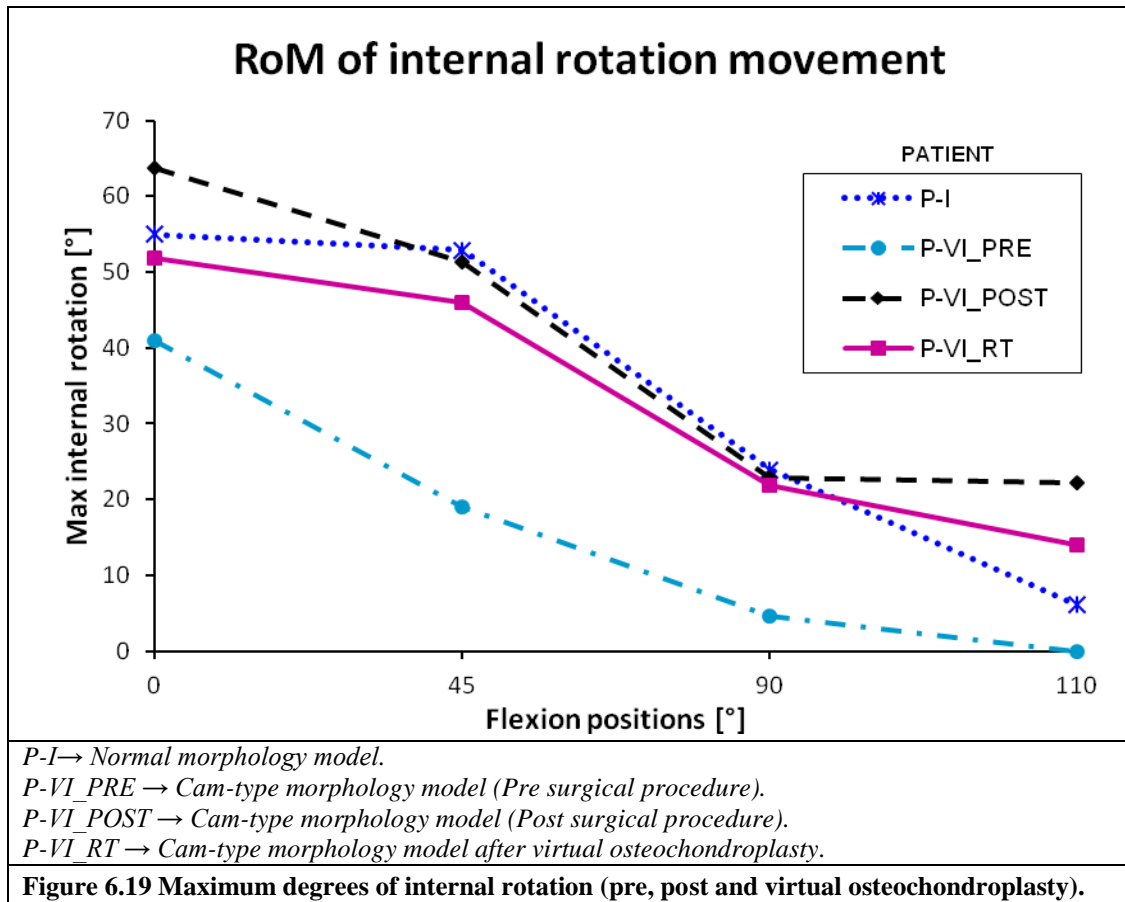
Table 6.6 shows the principal characteristics of the model of the hip following virtual resection (P-VI_RT) compared with the model of the hip following the actual surgical procedure (P-VI_POST).

Table 6.8 Status of the virtual and actual osteochondroplasty models.

	Model P-VI_POST	Model P-VI_RT
OUTER RESECTION AREA	*NM	1123 mm^2
** VOLUME BEFORE RESECTION (HNS)	**57,044.68 mm^3	57,044.68 mm^3
VOLUME AFTER RESECTION (HNS)	53,746.56 mm^3	51,967.14 mm^3
VOLUME RESECTED	3,298.12 mm^3	5,077.54 mm^3
% VOLUME RESECTED	5.7%	8.9 %
DEEPEST RESECTION POINT	*NM	4.81 mm

*NM = Not measurable.
** Only available for model P-VI_RT, but it was assumed for the calculations of model P-VI_POST only for a comparison in rough outline.

6.4 Summary of the Novel Technique

Figure 6.20 illustrates the complete virtual osteochondroplasty technique developed in the present study. It shows the sequential process used to perform the virtual osteochondroplasty to alleviate FAI, beginning with the information obtained from the CT scans, the consequent construction of the hip model, together with the preliminary analysis required to produce the results needed to construct the RT, and finally, the execution of the virtual resection and the final analysis.
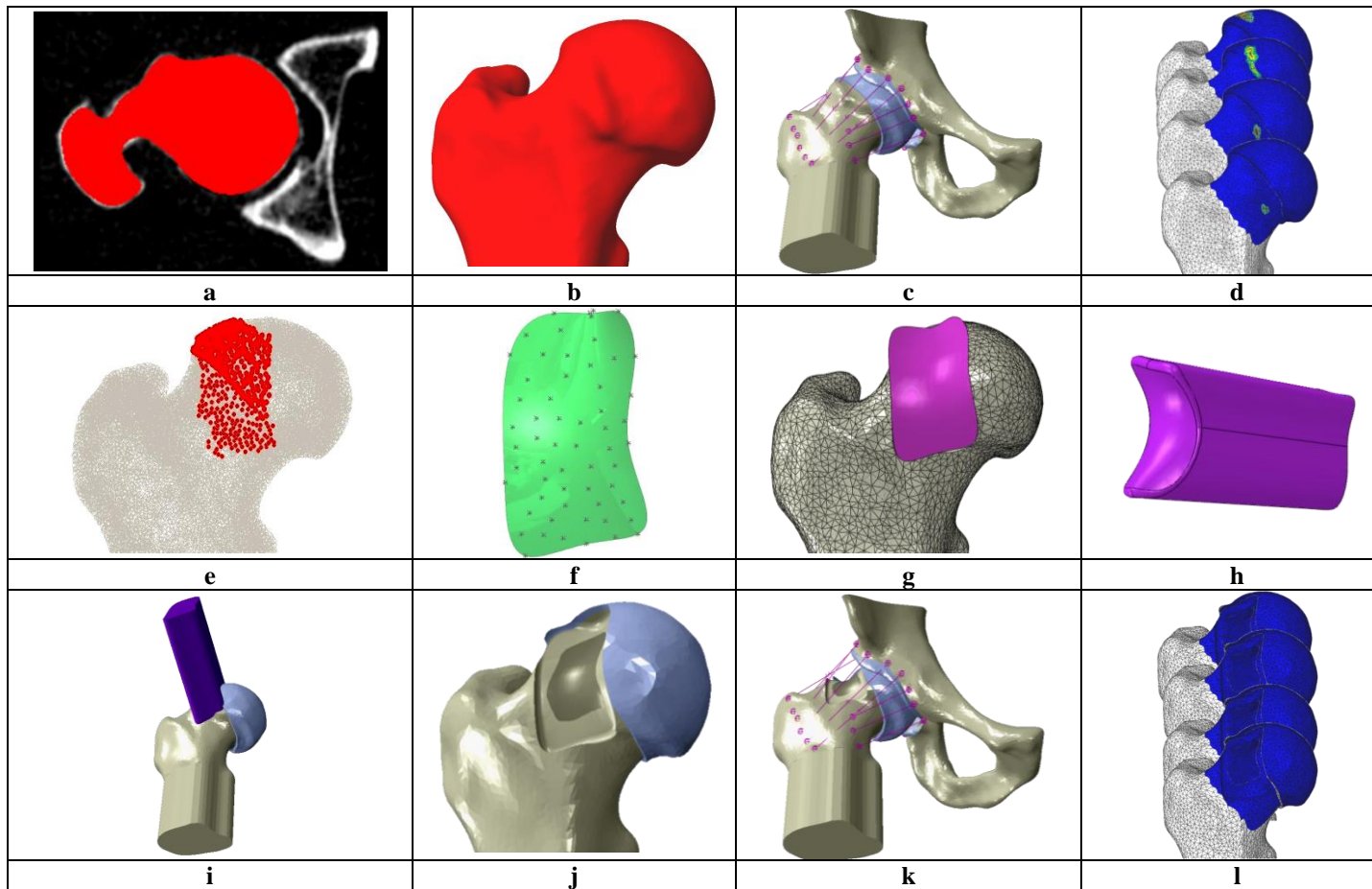
Figure 6.20 Complete methodology to perform the virtual osteochondroplasty to address FAI issues. (a) Colour mask in CT scan (ScanIP®); (b) 3D surface (ScanIP®); (c) Hip joint assembly (Abaqus CAE 6.10-1®); (d) Contact areas of the internal rotation movement (Abaqus CAE 6.10-1®); (e) Node coordinates of the contact areas (MathLAB®); (f) 3D surface (SolidWorks®); (g) Contact area over solid model (PowerSHAPE PRO®); (h) Resection tool for virtual osteochondroplasty (PowerSHAPE PRO®); (i) Volume subtraction in virtual osteochondroplasty (Abaqus CAE 6.10-1®); (j) Model after virtual osteochondroplasty (Abaqus CAE 6.10-1®); (k) Hip joint assembly after virtual osteochondroplasty (Abaqus CAE 6.10-1®); (l) Contact areas of the internal rotation movement in the model after virtual osteochondroplasty (Abaqus CAE 6.10-1®).

CHAPTER VII: CONCLUSIONS

7.1 Conclusions - Resection Depth Analysis

In this thesis a finite element model was developed to analyse the stress distribution in the femoral head–neck after resection. Five depths of resection in a cam-type impingement were considered in conjunction with five activities. The aim of the analysis was to understand the relationship between resection depth and the stress distribution in the head and neck.

From the analysis it was found that, in general, both the average von Mises stresses and the area of yielded bone significantly increased at a resection depth of ≥10 mm (33% of the head-neck shaft diameter), suggesting that when surgeons perform osteochondroplasty the depth of resection should be limited to 33% as a maximum. The activity of knee bending was the critical activity as in general it resulted in higher stresses than the other activities considered. The stress produced by the knee bend was between 1.5 and 2.5 times greater for the maximum resection depth investigated compared to the non resection case. The model predicted that yield was reached in the resection area at depths >10 mm or 1/3 the femoral neck diameter for the knee bend, normal walking, and walking down stairs, suggesting that patients should be advised to partial weight-bear on crutches for a period following surgery. Furthermore, as significant remodelling of the resection area will take considerably longer, patients should be advised to avoid impact type activities and single leg knee bends for a period post-operatively. The model suggests that bigger resections should probably be protected for longer times, whereas smaller resections can be rehabilitated faster.

As the depth of resection increases from 1/3 the diameter of the neck, the area where yield takes place expands from the resection area into the surface of the neck and inside through the cortical bone. The results suggest that for resection depths of 1/3 and 1/2 of the neck diameter fracture will occur in the resection area, in agreement with a previous experimental results [3], which showed that at 30% resection and greater, a change in the femoral head–neck response occurred, resulting in a reduction in the energy required to produce fracture and a modification to the failure

pattern, with fracture occurring at the level of the resection. In the current study it was found that at around 30% resection stresses start to increase sharply leading to yield in the resection area. While the experimental study used only axially loaded specimens, the study described in this thesis goes further by modelling a number of activities, thus providing a realistic expectation of what activities patients may attempt to undertake following surgery.

The current study utilized CT scan data from only one patient, thus restricting the analysis to a single resection area. But the results suggest that the stresses in the head and neck primarily depend on the resection depth relative to the overall neck diameter, and thus the findings are believed to be widely applicable.

The study had limitations and simplifications; for example, the virtual resection created was not as smooth as one that would be produced during surgery. However, a large number of elements were employed in these areas to accurately describe the geometry. Furthermore, the volume of each element was considered when calculating the stress; therefore, a reasonable degree of confidence can be associated with the predictions. The static model developed utilizes ''typical'' average peak hip contact forces [129] to provide an indication of the resected neck's response to load conditions resulting from various daily activities. Though the response to loading throughout the entire gait cycle was not considered, the model provides useful and insightful predictions and reinforces those obtained in a previous study [3].

Fracture propensity assessments were reported based on average von Mises stress and the volume of elements exceeding yield. While it may be argued that maximum principal stress is more applicable to fracture assessment, it was decided to report von Mises stress because of four reasons. First, a detailed assessment of fracture propensity was outside the scope of this initial study. The main focus was to investigate changes in stress patterns due to resections performed to avoid impingement. Hence, it was necessary to capture the changes in shape of the femoral head. Von Mises stress is an estimate of distortional energy in a loaded body; therefore, it was chosen for this study. Second, another set of analysis was conducted examining the maximum principal stresses and the trend of the average values of von

Mises and maximum principal stress for the various levels of resection was broadly similar as previously described in Chapter IV (Section 4.9). Third, numerical values of maximum stress may be high at a point due to surface irregularities after a virtual resection is performed. These irregularities may be absent in patients, but are hard to avoid in a numerical model due to non-uniform element sizes. Hence, an average stress was reported. Finally, many studies used Von Mises stress to report mechanical stresses in bones [141, 153, 154]. Adopting a similar metric may help researchers compare the results with the literature.

The model considered the trabecular bone as exhibiting elastic-plastic, isotropic material behaviour. The intact femur model using these properties was successfully validated against the results from a cadaveric investigation [3], so the material properties employed are sufficiently accurate for this study. In addition, while it is recognized that the elastic modulus of trabecular bone depends primarily on apparent bone density, the exact form of the dependency is controversial [155]. The issue is further complicated by the dependency of the relationship on loading direction, trabecular orientation, and anisotropy. It is acknowledged, however, that within a single anatomical site density range is limited [155], which suggests that an invariant bone property, as was used in this work, should enable relatively accurate predictions to be obtained.

In conclusion, the results suggest that to ensure integrity of the femoral head and neck, resection depth should be kept to <10 mm or 1/3 of the diameter of the neck.

7.2 Conclusions - Failure Analysis

In order to investigate the association between osteoporosis and both the mechanism and risk of femoral neck fracture after femoral osteochondroplasty, a 3D finite element model was developed using CT scan data from a patient with a cam-type femoroacetabular impingement. A quasi-brittle damage plasticity material formulation was employed in the finite element analysis to provide an in-depth evaluation of fracture risk. Three loading variations were considered in conjunction with both "normal" and a "critical" resection cases.

The results of the finite element analysis suggest that there is a risk of fracture in osteoporotic patients after femoral osteochondroplasty as indicated by the relatively large volumes of trabecular and cortical bone that the model predicts will undergo damage in the osteoporotic case. This risk extends to non-osteoporotic patients also when they are subjected to abnormally high loading.

The model predicted that no damage was present as a result of the "descending stairs" activity at any resection depth under "average peak loading". However, under "high peak loading", the model indicated that damage occurred, initiating in the trabecular bone of the femoral head-neck following osteochondroplasty. This damage was present in the 12mm resection case in healthy, non osteoporotic trabecular bone and in both the 6mm and 12mm cases for osteoporotic bone. At 6mm resection depth, 10% of the osteoporotic trabecular bone volume has undergone permanent damage, indicating the possibility of micro-fractures in the internal structure of the bone. At 12mm resection depth, the damage in the trabecular bone exceeds 50% signalling that internal fractures have become more significant.

The critical scenario occurred when osteoporotic bone was subjected to the loads developed in the "stumbling" scenario as the model predicted damage suggesting the initiation of fracture in both trabecular and cortical bone at all resection depths and also in the non-resection case. The volume of osteoporotic trabecular bone damage exceeded 30% in the non-resection case, rising to 70% at a resection depth of 12mm. The corresponding rise in osteoporotic cortical bone volume damage was from 5% to 10%, which although a small percentage, is very significant since cortical bone is the outer most bone of the femur structure and has a higher stiffness, suggesting that once this bone is damaged, the risk of fracture is significantly increased.

The FE model developed is subject to limitations which typically apply to all numerical analyses of this type [100], but particularly possible variations in the elastic modulus of the trabecular bone due to loading direction, trabecular orientation, and anisotropy [155] were not considered. However, research suggests that the error introduced by such an assumption should be relatively small when considering bone from a single anatomical site [155]. In addition, the effects of

repeated or cyclic loading were not investigated which may occur when a patient undertakes typical daily activities such as descending a flight of stairs, in which case fracture may occur at lower loading levels due to fatigue.

In summary, the model predicts that damage can occur in the bone of osteoporotic patients following osteochondroplasty for cam-type impingement during typical daily activities, such as descending stairs. The extent of bone damage is significantly greater than in non-osteoporotic bone indicating that strict protected weight bearing is indicated in the post-operative phase in such individuals. Furthermore, the level of damage increases significantly when patients are subjected to high load conditions and activities suggesting that even greater protection is required for heavier patients and that great care should be taken to avoid the adverse loading conditions modelled.

7.3 Conclusions – Range of Motion and Virtual Osteochondroplasty Analysis

A 3-Dimensional finite element model that can predict the internal rotation RoM and identify the impingement area in patients with cam type FAI was developed in this thesis. This model was used to investigate the impingement area and reduction in the internal rotation movement in four hips from FAI patients.

The results obtained from the model indicate that impingement area and RoM were patient dependant, being related to the particular morphology of the hip. Where impingement was predicted, it occurred in the anterosuperior area of the femoral neck-head shaft region. The average impingement area for the four FAI hips was 688.5 mm^2 or approximately 19% of the average overall head neck shaft surface area. Model predictions confirmed that FAI can result in a significant reduction in ROM in patients. In the FAI hips modelled in the present study, RoM was reduced by as much as 69% compared to a hip of normal morphology.

The FE model is subject to limitations including simplifications in materials properties, geometry representation and boundary conditions. However, the mesh sensitivity analysis and model validation exercises undertaken provide a degree of confidence in the accuracy of the model. In addition, the internal-rotation RoM

calculated at 90º of flexion in the four FAI models (P-II, P-III, P-IV and P-V) was between 6.33º and 8.55º which compares well with those (10º ± 6º) determined for Cam-type FAI patients from a clinical study [8].

The model developed overcomes some of the limitations identified in current software used to predict impingement and RoM in FAI hips, for example the geometric models analysed were based on CT data from actual hips with FAI. Also, the model developed considers and models cartilage and ligaments and realistic material properties are applied to all components in the model. Furthermore, the FE model can be applied to analyse hips presenting a large dysplasia, which is a limitation of some of the other models available.

In conclusion, the application of the methodology provides a very useful tool for calculating RoM and identifying the impingement area in FAI hips and is of benefit in the diagnosis, preoperative planning and selection of treatment for patients with FAI.

A virtual osteochondroplasty procedure was presented which involved undertaking a virtual resection of a FAI hip based on the areas of impingement calculated from the RoM analysis. Results following the virtual osteochondroplasty procedure analysis confirmed a reduction in FAI and an increase in the internal rotation RoM in all flexion conditions considered to values close to those found in hips with normal morphology.

Virtual osteochondroplasty reduced FAI and increased RoM to values close to those of the normal hip with a reduction in bone volume of 3.7% and a maximum resection depth that was within the safe range reported by the resection depth [3, 100] and failure analyses.

7.4 Conclusions – Validation of the Technique

In order to validate further the virtual osteochondroplasty procedure a model of a hip from an actual patient with FAI was created and the RoM predicted following application of the virtual osteochondroplasty methodology was compared with the results from a model of the same hip after an actual osteochondroplasty had been

performed on the patient using a resection area and depth identified in the conventional way by a surgeon.

Following virtual osteochondroplasty impingement was avoided and RoM increased substantially from prior to the virtual procedure to values close to those of the normal hip, with a reduction in bone volume of 8.9% and a maximum resection depth that would be considered safe (4.81 mm or 16% of the femoral neck diameter).

Actual osteochondroplasty resulted in the avoidance of FAI and an increase in RoM beyond normal hip levels but with a smaller resection volume which means it is somewhat safer than the resection indicated by virtual osteochondroplasty. Although, the actual cause of this anomaly is not clear, it is thought that it could result from the following considerations.

- The amount of bone resected in the acetabular region in the actual surgery which is not considered in the virtual procedure.
- Small variations in the positioning of the patient during the pre and post surgery scanning.
- Some dimensional variations due to the assumption of the volume before resection. Because the volume considered was calculated from P-VI_PRE and this model only shares the same dimensional conditions with model P-VI_RT as both come from the same CT scans, unlike model P-VI_POST which came from different CT scans, so it is not possible to calculate its corresponding volume before resection.
- Unexpected consequences of actual surgery on the connective tissue and auxiliary joint structures that are absent from the virtual osteochondroplasty model.

In conclusion, the technique presented emerges as a useful tool to diagnose, define and plan treatment preoperatively, and to predict the results after surgical procedures related to FAI.

7.5 Future work

Although the results presented here have demonstrated the success of the methodology presented it could be further developed based in the following considerations:

Modelling

- Perform more validations with models based on pre and post operative CT scans.
- Apply the methodology to perform the virtual osteochondroplasty in models of patients with pincer-type and mixer-type impingements.
- Apply the methodology in models of patients subjected to periacetabular osteotomy.

Implementation

- Execute the predicted virtual osteochondroplasty in physical models and test experimentally.
- Execute the predicted virtual osteochondroplasty in patients diagnosed with FAI.
- Execute the predicted virtual osteochondroplasty in physical models by using Computer-aided manufacturing (CAM) tools.
- Execute the predicted virtual osteochondroplasty in physical models by using CAM tools available in the orthopaedic market.
- If the available tools do not satisfy the requirements to apply the methodology, design or re-design a tool that can be used in the surgery room to apply the developed methodology.
- Execute the predicted virtual osteochondroplasty in physical models by using the CAM tool appropriated for the surgery room.
- Execute the predicted virtual osteochondroplasty in patients diagnosed with FAI by using the CAM tool appropriated for the surgery room.

PUBLICATIONS

Published

Changes in the stress in the femoral head neck junction after osteochondroplasty for hip impingement: a finite element study. Alonso-Rasgado T, Jimenez-Cruz D, Bailey CG, Mandal P, Board T. Journal of Orthopaedic Research 30:1999–2006, 2012. DOI: 10.1002/jor.22164

Submitted

Failure Analysis following Osteochondroplasty for Hip Impingement in Osteoporotic and Non-osteoporotic Bones. Jimenez-Cruz D, Alonso-Rasgado T, Bailey CG, Board T. Journal of Orthopaedic Research 2014.

Prediction of the Reduction of Range of Motion in Cam-type Femoroacetabular Impingement. Jimenez-Cruz D, Alonso-Rasgado T, Bailey CG, Board T. Journal of Orthopaedic Research 2014.

In Process

Methodology to perform a specific-patient diagnosis and virtual osteochondroplasty to solve Cam-type Femoroacetabular Impingement. Jimenez-Cruz D, Alonso-Rasgado T, Bailey CG, Board T.

Poster Presentations

A finite element based investigation into the stresses in the femoral head neck junction after osteochondroplasty for hip impingement. Jimenez-Cruz D, Alonso-Rasgado T, Bailey CG, Mandal P, Board T. British hip society. Annual scientific meeting. Manchester, United Kingdom 2012.

Investigation of the fracture mechanism of the osteoporotic and non-osteoporotic femoral head after osteochondroplasty for hip impingement: Finite element study. Jimenez-Cruz D, Alonso-Rasgado T, Bailey CG, Board T. European Hip society. 10th congress. Milano, Italy 2012.

Analysis of the Fracture Mechanism after Osteochondroplasty for Hip Impingement on Osteoporotic and Non-Osteoporotic Bones under Normal and High Loading:

Finite Element Study. Jimenez-Cruz D, Alonso-Rasgado T, Bailey CG, Board T. SET for BRITAIN 2014. London, United Kingdom 2014.

REFERENCES

1.   Drake R, Vogl W, Mitchell AW. 2007 Gray's anatomy for students. 2nd ed: Elsevier Inc.

2.   Gross JM, Fetto J, Rosen E. 2009. Chapter 11. The Hip. In: Gross JM, Fetto J, Rosen E, editors. Musculoskeletal examination. 3rd ed.: Wiley-Blackwell; p. 243-334.

3.   Mardones RM, Gonzalez C, Chen Q, Zobitz M, Kaufman KR, Trousdale RT. 2005. Surgical treatment of femoroacetabular impingement: evaluation of the effect of the size of the resection. J Bone Joint Surg Am 87(2): 273-9.

4.   Marieb E, Hoehn K. 2006. Human anatomy and physiology. 7th ed: Pearson Education, Inc.

5.   Palastanga N, Field D, Soames R. 2002. Anatomy and human movement. Structure and function. 4th ed: Butterworth-Heinemann; p 677.

6.   Rizzo D. 2001. Delmar's Fundamentals of Anatomy and Physiology. 1st ed: Thomson Learning; p 467.

7.   Beaulé PE. 2002. Femoro-acetabular impingement: A cause of hip pain. Proceedings of UCLA Healthcare 6(2).

8.   Dooley PJ. 2008. Femoroacetabular impingement syndrome: Nonarthritic hip pain in young adults. Can Fam Physician 54(1): 42-7.

9.   Fadul DA, Carrino JA. 2009. Imaging of femoroacetabular impingement. J Bone Joint Surg Am 91 Suppl 1: 138-43.

10.   Ganz R, Leunig M, Leunig-Ganz K, Harris WH. 2008. The etiology of osteoarthritis of the hip: An integrated mechanical concept. Clin Orthop Relat Res 466(2): 264-272.

11.   Ganz R, Parvizi J, Beck M, Leunig M, Nötzli H, Siebenrock KA. 2003 Femoroacetabular impingement. A cause for osteoarthritis of the hip. Clin Orthop Relat Res 417: 112-120.

12.   Graves ML, Mast JW. 2009. Femoroacetabular impingement: do outcomes reliably improve with surgical dislocations? Clin Orthop Relat Res 467(3): 717-23.

13.   Ito K, Leunig M, Ganz R. 2004. Histopathologic features of the acetabular labrum in femoroacetabular impingement. Clin Orthop Relat Res (429): 262-71.

14.   Jaberi FM, Parvizi J. 2007. Hip pain in young adults: femoroacetabular impingement. J Arthroplasty 22(7 Suppl 3): 37-42.

15.   Kassarjian A, Belzile E. 2008. Femoroacetabular impingement: presentation, diagnosis, and management. Semin Musculoskelet Radiol 12(2): 136-45.

16.   Kassarjian A, Brisson M, Palmer WE. 2007. Femoroacetabular impingement. Eur J Radiol 63(1): 29-35.

17.   Lavigne M, Parvizi J, Beck M, Siebenrock KA, Ganz R, Leunig M. 2004. Anterior femoroacetabular impingement. Part I. Techniques of joint preserving surgery. Clin Orthop Relat Res 418: 61-66.

18.   Leunig M, Beaulé PE, Ganz R. 2009. The concept of femoroacetabular impingement: current status and future perspectives. Clin Orthop Relat Res 467(3): 616-622.

19.   Leunig M, Beck M, Dora C, Ganz R. 2005. Femoroacetabular impingement: etiology and surgical concept. Oper Tech Orthop 15(3): 247-255.

20.   Leunig M, Ganz R. 2009. FAI - Concept and etiology. Clin Orthop Relat Res 38(5): 394-401.

21.   Philippon M, Schenker M, Briggs K, Kuppersmith D. 2007. Femoroacetabular impingement in 45 professional athletes: Associated pathologies and return to sport following arthroscopic decompression. Knee Surg Sport Tr A 15(7): 908-914.

22.   Philippon MJ, Maxwell RB, Johnston TL, Schenker M, Briggs KK. 2007. Clinical presentation of femoroacetabular impingement. Knee Surg Sport Tr A 15(8): 1041-1047.

23.   Sink EL, Gralla J, Ryba A, Dayton M. 2008. Clinical presentation of femoroacetabular impingement in adolescents. J Pediatr Orthop 28(8): 806-11.

24.   Tannast M, Goricki D, Beck M, Murphy SB, Siebenrock KA. 2008. Hip damage occurs at the zone of femoroacetabular impingement. Clin Orthop Relat Res 466(2): 273-80.

25.   Tannast M, Siebenrock KA, Anderson SE. 2007. Femoroacetabular impingement: radiographic diagnosis--what the radiologist should know. Am J Roentgenol 188(6): 1540-52.

26.   Wisniewski SJ, Grogg B. 2006. Femoroacetabular impingement: an overlooked cause of hip pain. Am J Phys Med Rehabil 85(6): 546-9.

27.   Leunig M, Robertson W, Ganz R. 2007. Femoroacetabular impingement: Diagnosis and management, including open surgical technique. Oper Techn Sport Med 15: 178-188.

28.   Jager M, Wild A, Westhoff B, Krauspe R. 2004. Femoroacetabular impingement caused by a femoral osseous head-neck bump deformity: clinical, radiological, and experimental results. J Orthop Sci 9(3): 256-63.

29.   Burnett RS, Della Rocca GJ, Prather H, Curry M, Maloney WJ, Clohisy JC. 2006. Clinical presentation of patients with tears of the acetabular labrum. J Bone Joint Surg Am 88(7): 1448-57.

30.   Ecker TM, Puls M, Steppacher SD, Bastian JD, Keel MJ, Siebenrock KA, Tannast M. 2011. Computer-assisted femoral head-neck osteochondroplasty using a surgical milling device an in vitro accuracy study. J Arthroplasty 27(2): 310-6.

31.   Delcam. Copy CAD. 2010 [cited; Available from: http://www.delcam.com/.

32.   Simpleware.   ScanIP.   2010   [cited;   Available   from: http://www.simpleware.com/software/scanip/.

33.   SIMULIA   DS.   Abaqus/CAE.   2010   [cited;   Available   from: http://www.simulia.com/index.html.

34.   Mardones RR, Barrientos CV, Nemtala UF, Tomic A, Salineros UM. 2010. Femoroacetabular impingement as a cause of inguinal pain. Rev Med Chil 138(1): 102-8.

35.   Arbabi E, Chegini S, Boulic R, Tannast M, Ferguson SJ, Thalmann D. 2010. Penetration depth method--novel real-time strategy for evaluating femoroacetabular impingement. J Orthop Res 28(7): 880-6.

36.   Giori NJ, Trousdale RT. 2003. Acetabular retroversion is associated with osteoarthritis of the hip. Clin Orthop Relat Res (417): 263-9.

37.   Wyss TF, Clark JM, Weishaupt D, Notzli HP. 2007. Correlation between internal rotation and bony anatomy in the hip. Clin Orthop Relat Res 460: 152-8.

38.   AAOS.   Description   of   FAI.   2013   [cited;   Available   from: http://orthoinfo.aaos.org/.

39.   Kassarjian A, Cerezal L, Llopis E. 2006. Femoroacetabular impingement. Top Magn Reson Imaging 17(5): 337-45.

40.   Leunig M, Ganz R. 2005. Femoroacetabuläres impingement. Häufige ursache von zur arthrose führenden hüftbeschwerden. Unfallchirurg 108: 9-17.

41.   Leunig M,   Huff TW, Ganz R. 2009. Femoroacetabular impingement: Treatment of the acetabular side. Instructional course lectures 58: 223-229.

42.   Pfirrmann CW, Mengiardi B, Dora C, Kalberer F, Zanetti M, Hodler J. 2006. Cam and pincer femoroacetabular impingement: characteristic MR arthrographic findings in 50 patients. Radiology 240(3): 778-85.

43.   Ito K,   Minka MA, 2nd,   Leunig M,   Werlen S, Ganz R. 2001. Femoroacetabular   impingement   and   the   cam-effect.   A   MRI-based quantitative anatomical study of the femoral head-neck offset. J Bone Joint Surg Br 83(2): 171-6.

44.   Dhawan A, Huang H, Kim D. 2008. Principles and advanced methods in medical imaging and image analysis. 1st ed: World Scientific Publishing; p 850.

45.   Leondes C. 2005. Medical imaging systems technology. Methods in general anatomy. 1st ed. Vol. A: World Scientific Publishing; p 335.

46.   Horisberger M,   Brunner A, Herzog R. 2010. Arthroscopic treatment of femoroacetabular impingement of the hip. A new technique to access the joint. Clin Orthop Relat Res 468: 182-190.

47.   Philippon MJ, Briggs KK, Yen YM, Kuppersmith DA. 2009. Outcomes following hip arthroscopy for femoroacetabular impingement with associated chondrolabral dysfunction: Minimum two-year follow-up. J Bone Joint Surg Br 91(1): 16-23.

48.   Ganz R, Gill TJ, Gautier E, Ganz K, Krugel N, Berlemann U. 2001. Surgical dislocation of the adult hip a technique with full access to the femoral head and acetabulum without the risk of avascular necrosis. J Bone Joint Surg Br 83(8): 1119-24.

49.   Bardakos NV, Vasconcelos JC, Villar RN. 2008. Early outcome of hip arthroscopy for femoroacetabular impingement: the role of femoral osteoplasty in symptomatic improvement. J Bone Joint Surg Br 90(12): 1570-5.

50.   Petit CJ, Philippon MJ. 2008. Arthroscopic management of osteochondral defects of the hip. Oper Techn Sport Med 16(4): 194-200.

51.   Byrd T. 2001. Hip Arthroscopy Principles and Application. In: A Smith & Nephew Technique Plus™ Illustrated Guide: Smith & Nephew, Inc.; p. 1-12.

52.   Beaule PE, Zaragoza E, Motamedi K, Copelan N, Dorey FJ. 2005. Three-dimensional computed tomography of the hip in the assessment of femoroacetabular impingement. J Orthop Res 23(6): 1286-92.

53.   Tannast M, Kubiak-Langer M, Langlotz F, Puls M, Murphy SB, Siebenrock KA. 2007. Noninvasive three-dimensional assessment of femoroacetabular impingement. J Orthop Res 25(1): 122-31.

54.   Chegini S, Beck M, Ferguson SJ. 2009. The effects of impingement and dysplasia on stress distributions in the hip joint during sitting and walking: a finite element analysis. J Orthop Res 27(2): 195-201.

55.   Jorge JP, Simoes FM, Pires EB, Rego PA, Tavares DG, Lopes DS, Gaspar A. 2012. Finite element simulations of a hip joint with femoroacetabular impingement. Comput Methods Biomech Biomed Engin.

56.   Clinical Graphics Online. Femoroacetabular Impingement Analysis Report. 2012 [cited 2012 26/12/12]; Available from: http://www.clinicalgraphics.com/.

57.   An Y, Draughn R. 2000. Mechanical Testing of Bone and the Bone-Implant Interface: CRC Press LLC.

58.   Bartl R, Frisch B. 2009. Osteoporosis. Diagnosis, Prevention, Therapy: Springer.

59.   Dudek R. 2000. High-Yield Histology. 2 ed: Lippincott Williams & Wilkins.

60.   Guyton A, Hall J. 2006. Textbook of Medical Physiology. 11 ed: Elsavier Inc.

61.   Nather A. 2005. Bone Grafts and Bone Substitutes. Basic Science and Clinical Applications. 1st ed: World Scientific Publishing; p 592.

62.   Calais-Germain B. 2007. Anatomy of movement. Rev ed: Eastland Press, Inc.; p 316.

63.   Ethier CR, Simmons CA. 2007. Introductory Biomechanics: From Cells to Organisms. 1st ed: Cambridge Unversity Press; p 498.

64.   Cael C. 2010. Functional Anatomy: Lippincott Williams & Wilkins; p 446.

65.   Fawcett D, Bloom W, Jensh R. 1995. Bloom and Fawcett. A textbook of histology. 12th ed: Chapman & Hall.

66.   Nordin M, Frankel V. 2001. Basic Biomechanicas of the Musculoskeletal System ed. Nordin M, Frankel V: Lippincott Williams & Wilkins; p 323.

67.   Peterson D, Bronzino J. 2008. Biomechanics. Principles and applications: CRC Press; p 353.

68.   Thompson J. 2002. Netter's Concise Atlas of Orthopaedic Anathomy. 1st ed: Elsevier Inc.

69.   Cowin S, Doty S. 2007. Tissue Mechanics: Springer Science+Business Media, LLC.

70.   Buckwalter JA, Glimcher MJ, Cooper RR, Recker R. 1996. Bone Biology Part 1: Structure, Blood supply, Cells, Matrix and Mineralization. J Bone Joint Surg Br 77(A): 1256-1275.

71.   Martin B, Burr D. 1998. Skeletal tissue mechanics: Springer- Verlang.

72.   Tzelepi V, Tsamandas A. 2009. Bone Anatomy, physiology and function. In: Kardamakis E, Vassiliou V, Chow E, editors. Bone Metastases: A Translational and Clinical Approach: Springer p. 3-29.

73.   Mirelles R, Puig M. 2000. Biomecanica Clinica del Apararto Locomotor: Masson, S.A.; p 321.

74.   Mow VC, Huiskes R. 2005. Basic orthopaedic biomechnics and mechano-biology. 3rd ed: Lippencott Williams and Wilkins.

75.   Skinner H, McMahon P. 2006. Current diagnosis and treatment in orthopedics. 4th ed: Mc Graw-Hill Companies, Inc; p 1032.

76.   Fyhrie DP, Kimura JH. 1999. NACOB presentation Keynote lecture. Cancellous bone biomechanics. North American Congress on Biomechanics. J Biomech 32(11): 1139-48.

77.   Goldstein SA. 1987. The mechanical properties of trabecular bone: dependence on anatomic location and function. J Biomech 20(11-12): 1055-61.

78.   Martin RB. 1991. Determinants of the mechanical properties of bones. J Biomech 24 Suppl 1: 79-88.

79.   Reilly DT, Burstein AH. 1974. Review article. The mechanical properties of cortical bone. J Bone Joint Surg Am 56(5): 1001-22.

80.   Reilly DT, Burstein AH. 1975. The elastic and ultimate properties of compact bone tissue. J Biomech 8(6): 393-405.

81.   Turner CH, Rho J, Takano Y, Tsui TY, Pharr GM. 1999. The elastic properties of trabecular and cortical bone tissues are similar: results from two microscopic measurement techniques. J Biomech 32(4): 437-41.

82.   Morgan EF, Barnes GL. 2008. The Bone Organ System: Form and Function. In: Marcus R, Feldman D, editor^editors. Osteoporis Int. 3rd ed.: Elsevier, Inc.; p. 3-25.

83.   Nather A. 2005. Bone Grafts and Bone Substitutes. Basic Science and Clinical Applications: World Scientific Publishing.

84.   Brinckmann P, Frobin W, Leivseth G. 2002. Musculoskeletal Biomechanics: Thieme.

85.   Ibarra LG, Valdes M. 2012. Osteoporosis: Prevencion, diagnostico, tratamiento y rehabilitacion. 1st ed: Editorial Trillas; p 276.

86.   Carter DR, Hayes WC. 1977. The compressive behavior of bone as a two-phase porous structure. J Bone Joint Surg Am 59(7): 954-62.

87.   An Y, Draughn R. 2000. Mechanical Testing of Bone and the Bone-Implant Interface. 1st ed: CRC Press LLC; p 320.

88.   Gupta HS, Zioupos P. 2008. Fracture of bone tissue: The 'hows' and the 'whys'. Med Eng Phys 30(10): 1209-26.

89.   Hansen U, Zioupos P, Simpson R, Currey JD, Hynd D. 2008. The effect of strain rate on the mechanical properties of human cortical bone. J Biomech Eng 130(1): 011011.

90.   Han SK, Federico S, Epstein M, Herzog W. 2005. An articular cartilage contact model based on real surface geometry. J Biomech 38(1): 179-84.

91.   Maciel A, Boulic R, Thalmann D. 2003. Deformable Tissue Parameterized by Properties of Real Biological Tissue. IS4TM: 74-87.

92.   Lewis CL, Sahrmann SA. 2006. Acetabular labral tears. Phys Ther 86(1): 110-21.

93.   Ferguson SJ, Bryant JT, Ganz R, Ito K. 2000. The influence of the acetabular labrum on hip joint cartilage consolidation: a poroelastic finite element model. J Biomech 33(8): 953-60.

94.   Barbucci R. 2002. Integrated Biomaterials Sicence: Kluwer Academic Publishers.

95.   Nigg BM, Herzog W. 2003. Biomechanics of the musculo-skeletal system. 2nd ed. Ontario: John Wiley & Sons; p 643.

96.   Peterson D, Bronzino J. 2008. Biomechanics. Principles and Applications. 1st ed: CRC Press; p 353.

97.   Boudriot U, Hilgert J, Hinrichs F. 2006. Determination of the rotational center of the hip. Arch Orthop Trauma Surg 126(6): 417-20.

98.   Fessy MH, N'Diaye A, Carret JP, Fischer LP. 1999. Locating the center of rotation of the hip. Surg Radiol Anat 21(4): 247-50.

99.   Wu G, Siegler S, Allard P, Kirtley C, Leardini A, Rosenbaum D, Whittle M, D'Lima DD, Cristofolini L, Witte H, Schmid O, Stokes I. 2002. ISB recommendation on definitions of joint coordinate system of various joints for the reporting of human joint motion--part I: ankle, hip, and spine. International Society of Biomechanics. J Biomech 35(4): 543-8.

100.   Alonso-Rasgado T, Jimenez-Cruz D, Bailey CG, Mandal P, Board T. 2012. Changes in the stress in the femoral head neck junction after

osteochondroplasty for hip impingement: a finite element study. J Orthop Res 30(12): 1999-2006.

101. Ayeni OR, Bedi A, Lorich DG, Kelly BT. 2011. Femoral neck fracture after arthroscopic management of femoroacetabular impingement: a case report. J Bone Joint Surg Am 93(9): e47.

102. e Souza BGS, Philippon MJ. 2012. Complications and revision surgery in hip arthroscopy In: Marin-Peña O, editors. Femoroacetabular Impingement. 1st ed. Berlin: Springer-Verlag; p. 147-158.

103. Gedouin JE, May O, Bonin N, Nogier A, Boyer T, Sadri H, Villar RN, Laude F. 2010. Assessment of arthroscopic management of femoroacetabular impingement. A prospective multicenter study. Orthop Traumatol Surg Res 96(8 Suppl): S59-67.

104. Ilizaliturri VM. 2009. Complications of arthroscopic femoroacetabular impingement treatment: a review. Clin Orthop Relat Res 467(3): 760-8.

105. Papavasiliou AV, Bardakos NV. 2012. Complications of arthroscopic surgery of the hip. Bone Joint Res 1(7): 131-44.

106. Sampson TG. 2005. Arthroscopic treatment of femoroacetabular impingement. Tech Orthop (20): 65-62.

107. Sampson TG. 2005. Complications of hip arthroscopy. Tech Orthop 20: 63-66.

108. Bathe KJ. 1996. Finite Element Procedures. Rev ed: Prentice-Hall, Inc.; p 1036.

109. Cook R. 1995. Finite Element Modelling for Stress Analysis. 1st ed: John Wiley and Sons Inc.; p 320.

110. Kwon Y, Hyochoong B. 1997. The Finite Element Method using MATLAB. 1st ed: CRC Press LLC; p 519.

111. Moaveni S. 1999. Finite Element analysis: Theory and Application with ANSYS. 1st ed: Prentice-Hall, Inc.; p 527.

112. Logan D. 2007. A first course in the Finite Element Method. 4 ed: Thomson Canada Limited.

113. Fish J, Belytschko T. 2007. A first course in Finite Elements: John Wiley and Sons Inc.

114. Huiskes R, Chao EY. 1983. A survey of finite element analysis in orthopedic biomechanics: the first decade. J Biomech 16(6): 385-409.

115. Speirs AD, Heller MO, Duda GN, Taylor WR. 2007. Physiologically based boundary conditions in finite element modelling. J Biomech 40(10): 2318-23.

116. Brekelmans WA, Poort HW, Slooff TJ. 1972. A new method to analyse the mechanical behaviour of skeletal parts. Acta Orthop Scand 43(5): 301-17.

117. Adler R. 2010. Osteoporosis. Phatophysiology and clinical managment. 2nd ed: Humana Press.

118. SIMULIA DS. 2010. Abaqus/CAE 6.10. Analysis User's Manual.

119. Laude F, Sariali E, Nogier A. 2009. Femoroacetabular impingement treatment using arthroscopy and anterior approach. Clin Orthop Relat Res 467(3): 747-52.

120. Simpleware, *Reference Guide. ScanIP, +ScanFE, +ScanCAD. Version 3.2*. 2010.

121. Anderson AE, Ellis BJ, Maas SA, Peters CL, Weiss JA. 2008. Validation of finite element predictions of cartilage contact pressure in the human hip joint. J Biomech Eng 130(5): 051008.

122. Majumder S, Roychowdhury A, Pal S. 2007. Simulation of hip fracture in sideways fall using a 3D finite element model of pelvis-femur-soft tissue complex with simplified representation of whole body. Med Eng Phys 29(10): 1167-78.

123. Phillips AT, Pankaj P, Howie CR, Usmani AS, Simpson AH. 2007. Finite element modelling of the pelvis: inclusion of muscular and ligamentous boundary conditions. Med Eng Phys 29(7): 739-48.

124. Thompson MS, Flivik G, Juliusson R, Odgaard A, Ryd L. 2004. A comparison of structural and mechanical properties in cancellous bone from the femoral head and acetabulum. Proc Inst Mech Eng H 218(6): 425-9.

125. Wirtz DC, Schiffers N, Pandorf T, Radermacher K, Weichert D, Forst R. 2000. Critical evaluation of known bone material properties to realize anisotropic FE-simulation of the proximal femur. J Biomech 33(10): 1325-30.

126. Augat P, Link T, Lang TF, Lin JC, Majumdar S, Genant HK. 1998. Anisotropy of the elastic modulus of trabecular bone specimens from different anatomical locations. Med Eng Phys 20(2): 124-31.

127. Dickenson RP, Hutton WC, Stott JR. 1981. The mechanical properties of bone in osteoporosis. J Bone Joint Surg Br 63-B(2): 233-8.

128. Li B, Aspden RM. 1997. Composition and mechanical properties of cancellous bone from the femoral head of patients with osteoporosis or osteoarthritis. J Bone Miner Res 12(4): 641-51.

129. Bergmann G, Deuretzbacher G, Heller M, Graichen F, Rohlmann A, Strauss J, Duda GN. 2001. Hip contact forces and gait patterns from routine activities. J Biomech 34(7): 859-71.

130. Little JP, Taddei F, Viceconti M, Murray DW, Gill HS. 2007. Changes in femur stress after hip resurfacing arthroplasty: Response to physiological loads. Clin Biomech 22(4): 440-448.

131. Lotz JC, Cheal EJ, Hayes WC. 1995. Stress distributions within the proximal femur during gait and falls: implications for osteoporotic fracture. Osteoporis Int 5(4): 252-61.

132. Bartl R, Frisch B. 2009. Osteoporosis: Diagnosis, Prevention, Therapy. 2nd ed. Berlin: Springer-Verlag; p 321.

133. Dennison E, Cole Z, Cooper C. 2005. Diagnosis and epidemiology of osteoporosis. Curr Opin Rheumatol 17(4): 456-61.

134. Stevenson JC, Marsh MS. 2007. An Atlas of Osteoporosis. 3rd ed. London: CRC Press; p 96.

135. Adachi JD, Bensen WG, Hodsman AB. 1993. Corticosteroid-induced osteoporosis. Semin Arthritis Rheum 22(6): 375-84.

136. Kanis JA, Johansson H, Oden A, Johnell O, de Laet C, Melton IL, Tenenhouse A, Reeve J, Silman AJ, Pols HA, Eisman JA, McCloskey EV, Mellstrom D. 2004. A meta-analysis of prior corticosteroid use and fracture risk. J Bone Miner Res 19(6): 893-9.

137. Burstein AH, Reilly DT, Martens M. 1976. Aging of bone tissue: mechanical properties. J Bone Joint Surg Am 58(1): 82-6.

138. Zioupos P, Currey JD. 1998. Changes in the stiffness, strength, and toughness of human cortical bone with age. Bone 22(1): 57-66.

139. Mazess RB. 1982. On aging bone loss. Clin Orthop Relat Res (165): 239-52.

140. Brown TA, Kohan L, Ben-Nissan B. 2007. Assessment by finite element analysis of the impact of osteoporosis and osteoarthritis on hip resurfacing. In 5th Australasian Congress on Applied Mechanics (ACAM 2007) Brisbane, Australia.

141. Zhao X, Chosa E, Totoribe K, Deng G. 2010. Effect of periacetabular osteotomy for acetabular dysplasia clarified by three-dimensional finite element analysis. J Orthop Sci 15(5): 632-40.

142. Morgan EF, Keaveny TM. 2001. Dependence of yield strain of human trabecular bone on anatomic site. J Biomech 34(5): 569-77.

143. Taylor ME, Tanner KE, Freeman MA, Yettram AL. 1996. Stress and strain distribution within the intact femur: compression or bending? Med Eng Phys 18(2): 122-31.

144. Polikeit A, Nolte LP, Ferguson SJ. 2004. Simulated influence of osteoporosis and disc degeneration on the load transfer in a lumbar functional spinal unit. J Biomech 37(7): 1061-9.

145. Zhang L, Yang G, Wu L, Yu B. 2010. The biomechanical effects of osteoporosis vertebral augmentation with cancellous bone granules or bone cement on treated and adjacent non-treated vertebral bodies: a finite element evaluation. Clin Biomech 25(2): 166-72.

146. Lotz JC, Cheal EJ, Hayes WC. 1991. Fracture prediction for the proximal femur using finite element models: Part II--Nonlinear analysis. J Biomech Eng 113(4): 361-5.

147. Morgan EF, Bouxsein ML. 2008. Biomechanics of bone and age-related fractures. In: Bilezikian JP, Raisz LG, Martin TJ, editor^editors. Principles of Bone Biology 3rd ed.: Elsevier Inc. ; p. 29-51.

148. Bergmann G, Graichen F, Rohlmann A, Bender A, Heinlein B, Duda GN, Heller MO, Morlock MM. 2011. Realistic loads for testing hip implants. Biomed Mater Eng 20(2): 65-75.

149. Hewitt J, Guilak F, Glisson R, Vail TP. 2001. Regional material properties of the human hip joint capsule ligaments. J Orthop Res 19(3): 359-64.

150. Wenger D, Miyanji F, Mahar A, Oka R. 2007. The mechanical properties of the ligamentum teres: a pilot study to assess its potential for improving stability in children's hip surgery. J Pediatr Orthop 27(4): 408-10.

151. Zou Z, Chavez-Arreola A, Mandal P, Board TN, Alonso-Rasgado T. 2012. Optimization of the position of the acetabulum in a ganz periacetabular osteotomy by finite element analysis. J Orthop Res 31(3): 472-9.

152. Schofer MD, Pressel T, Heyse TJ, Schmitt J, Boudriot U. 2010. Radiological determination of the anatomic hip centre from pelvic landmarks. Acta Orthop Belg 76(4): 479-85.

153. Innocenti B, Truyens E, Labey L, Wong P, Victor J, Bellemans J. 2009. Can medio-lateral baseplate position and load sharing induce asymptomatic local bone resorption of the proximal tibia? A finite element study. J Orthop Surg Res 4: 26.

154. Taddei F, Cristofolini L, Martelli S, Gill HS, Viceconti M. 2006. Subject-specific finite element models of long bones: An in vitro evaluation of the overall accuracy. J Biomech 39(13): 2457-67.

155. Keaveny TM, Morgan EF, Niebur GL, Yeh OC. 2001. Biomechanics of trabecular bone. Annu Rev Biomed Eng 3: 307-33.

ANNEX 1

Changes in the Stress in the Femoral Head Neck Junction after Osteochondroplasty for Hip Impingement: A Finite Element Study

Teresa Alonso-Rasgado,[1] David Jimenez-Cruz,[1] Colin G. Bailey,[1] Parthasarathi Mandal,[1] Tim Board[2]

[1]School of Mechanical, Aerospace and Civil Engineering, The University of Manchester, Manchester M13 9PL, UK, [2]Wrightington Hospital, Wigan and Leigh NHS Foundation Trust, Lancashire, UK

ABSTRACT: The surgical treatment of femoroacetabular impingement (FAI) often involves femoral osteochondroplasty. One risk of this procedure is fracture of the femoral neck. We developed a finite element (FE) model to investigate the relationship between depth of resection and femoral neck stress. CT data were used to obtain the geometry of a typical cam-type hip, and a 3D FE model was constructed to predict stress in the head–neck after resection surgery. The model accounted for the forces acting on the head and abductor muscular forces. Bone resection was performed virtually to incremental resection depths. The stresses were calculated for five resection depths and for five different activities (i) standing on one leg (static case); (ii) two-to-one-to-two leg standing; (iii) normal walking; (iv) walking down stairs; and (v) a knee bend. In general, both the average Von Mises stresses and the area of bone that yielded significantly increased at a resection depth of ≥ 10 mm. The knee bend and walking down stairs demonstrated the highest stresses. The FE model predicts that fracture is likely to occur in the resection area first following removal of a third (10 mm) or more of the diameter of the femoral neck. We suggest that when surgeons perform osteochondroplasty for hip impingement, the depth of resection should be limited to 10 mm. © 2012 Orthopaedic Research Society. Published by Wiley Periodicals, Inc. J Orthop Res

Keywords: hip impingement; osteochondroplasty; finite element

In cam type femoroacetabular impingement (FAI), abnormal contact occurs between the anterosuperior femoral head–neck junction and the acetabular cartilage[1–5] during flexion and internal rotation of the hip. Normally, this area of the femur has a concave configuration but in cam impingement, it is flattened or convex[1–18] (Fig. 1). Osteochondroplasty for FAI aims to alleviate abnormal contact to allow normal motion. The procedure can be done via surgical hip dislocation,[19] allowing 360° visualization of the hip with promising mid-term results[1,5,13,14,17,20–22] or arthroscopically. The main drawback with arthroscopy stems from the poor visualization of the femoral neck, leading to osteochondroplasty of reduced effectiveness.[5–8,10,13,14,17,18,21]

Although achieving adequate resection is a common issue little information in the literature exists to guide a safe depth of resection. Logically, the greater the amount of bone removed, the greater the clearance for safe range of hip movement without impingement. However, as resection depth increases, so would the likely stress in the remaining bone in the neck, increasing the risk of post-operative fracture. Neck fracture is recognized as a serious complication of hip arthroscopy[23–27] with incidence rates in the range of 0.8–1%.[23–25] The only study to address the issue of resection depth was a cadaveric study[17] that concluded that peak loads only rise significantly once 50% of the neck is removed.

We investigated the stress distribution in the femoral head–neck after resection using a finite element (FE) model. Five depths of resection in a cam-type impingement were considered in conjunction with five activities: standing on one leg (static), two-to-one-to-two leg standing, normal walking, walking down stairs, and a knee bend. The aim was to understand the relationship between resection depth and the stress distribution in the head and neck.

METHODS

CT data were taken from a scan of a patient exhibiting cam-type impingement (Fig. 2). Slices were taken every 3 mm to give ~200 slices, which were used to construct the model; the dicom data were read into ScanIP® (Simpleware Ltd., Exeter, UK) to the create surfaces of the geometry (Fig. 3a,b). The surface information was exported into Delcam PowerSHAPE Pro® (Delcam Plc, Birmingham, UK) from which the solid model was created (Fig. 3c). The solid model was exported in parasolid format to Abaqus 6.9-2® FE analysis software (Abaqus, Inc., Dassault Systemes Simulia Corp, Providence, RI) to be meshed and analyzed (Fig. 3d).

The area of virtual resection was identified by a surgeon (TB) as a "worst case scenario." Having identified the resection area, five virtual operations were simulated with resection depths of 2 mm (7% of the neck diameter), 4 mm (13%), 6 mm (20%), 10 mm (33%), and 15 mm (50%; Fig. 4). In each case, the same outer area of cut was considered as this was the maximum extent of the impingement zone indicated by the CT scan. The resection depth for a cam-type impingement such as this one would typically be ~4 to 8 mm. The five activities (e.g., standing on one leg) were considered for each depth.

Geometry

The virtual resections were generated using Boolean operations and morphological filters with the shape of the resection being preserved across the depths considered. The Boolean operations facilitated the removal of virtual material from the 3D geometry of the head and neck. Morphological filters were employed to smooth the surfaces from which
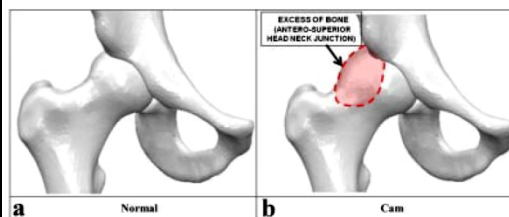
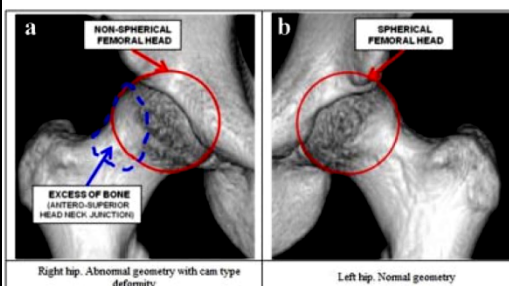**Figure 1.** Cam type impingement deformity. (a) Normal. (b) Cam.

Figure 2. CT scan diagnosis showing Femoroacetabular Impingement. (a) Right hip: Abnormal geometry with cam type deformity. (b) Left hip: Normal geometry.

material was removed. Six 3D FE models of the head–neck were developed to represent each resection depth and the head prior to resection. The geometry was meshed with linear, 4-noded tetrahedral elements.

Materials

The model considered cortical and cancellous bone and cartilage. These tissues were assumed to exhibit elastic-plastic, isotropic material behavior with properties taken from the literature[28–32] (Table 1). Full bonding was assumed at the interface between cortical and the cancellous bone.

Boundary Conditions

The boundary conditions that were considered were as follows. The bottom surfaces of the proximal femoral segment were fixed (displacements/rotations zero in all directions, Fig. 5a). Concentrated forces were used to represent the abductor muscle force and the force on the head due to body weight (Fig. 5b). To transmit the force to the head, a section of the hemi-pelvis including the acetabulum was included. The interface between the head and acetabulum was modeled using the "tie" constraints of Abaqus 6.9-2[®], so that adjoining nodes had the same displacements. A concentrated force was applied to the top of the pelvis. To avoid local stress concentrations and localized deformations, the pelvis was set as rigid enabling it to effectively transfer the load on to the head. The muscle force was applied at a reference point above the greater trochanter using a kinematic coupling constraint (Fig. 5c).

To determine the forces applied to the model, a free body diagram of the upper part of the head (Fig. 6) was used to calculate the reaction forces on the head and from the muscles considering the application of a percentage of the body weight, depending upon the activity.[33] The maximum values for each motion were employed. Table 2 illustrates the forces and the associated angles calculated from the free body diagram. Only the frontal plane forces were considered as these are generally higher forces than the transversal plane forces and our focus was on investigating which postoperative activities are important to avoid.

Mesh Sensitivity Analysis and Physical Corroboration of the Model

A sensitivity analysis based on a comparison of different mesh densities was performed to ensure accuracy of the results. The analysis consisted of employing the non-resection, intact model and three densities (77,666, 91,068, and 360,444 elements) and comparing the average Von Mises stress in the neck. The middle density was chosen since the average Von Mises stress in the neck changed by <0.5% between the middle and finest mesh.

The number of elements used changed with resection depth due to the removal of material and the geometry of the remaining resected area (Table 3). After a virtual resection, the area exposed was highly irregular, and a large number of elements was required to capture the geometry and ensure high accuracy in stress predictions. Although less volume of cancellous bone was being meshed as the resection depth increased, the number of elements employed actually increased due to the increased complexity of the geometry.

The model was corroborated by comparing predictions from the intact femur model with results from a cadaveric study.[17] That investigation consisted of testing 15 pairs of femora to fracture using a materials testing system following removal of 10%, 30%, or 50% of the femoral neck from one femur in each pair. The contralateral femur was left intact as a control. A compressive load was applied to the head at a displacement rate of 20 mm/min until fracture. Our intact,
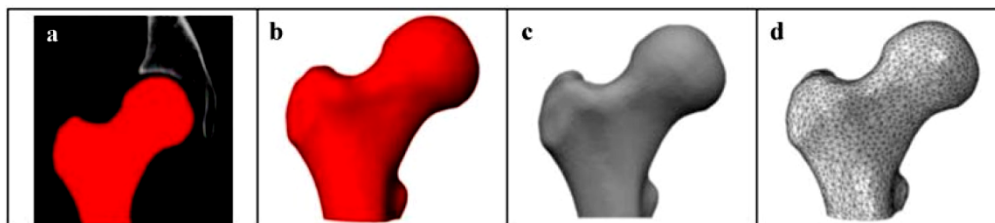

Figure 3. Model development process. (a) Slice mask on CT scan DICOM data. (ScanIP[®]). (b) 3D surface (ScanIP[®]). (c) Solid model obtained from the 3D surface (Delcam PowerSHAPE Pro[®]). (d) Solid part imported to create the model (Abaqus 6.9-2[®]).
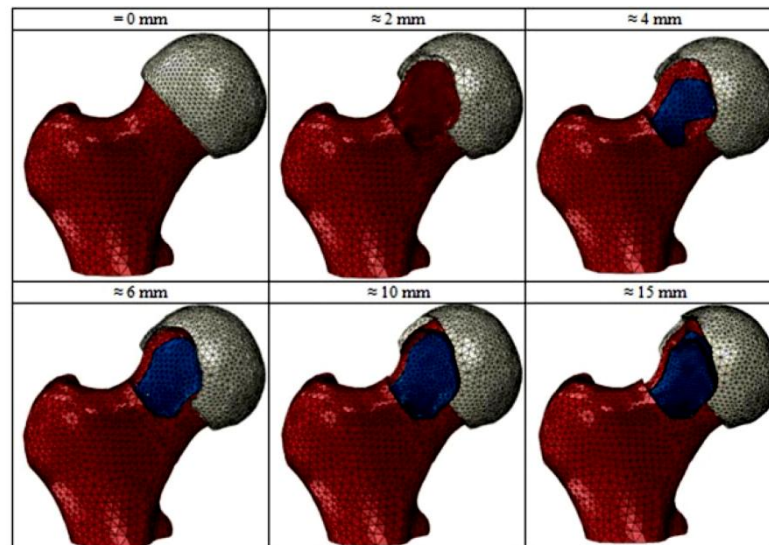
Figure 4. Resection area and depths considered in the study. Three tissues can be differentiated in the model. Cortical bone in red, cancellous bone in blue, and cartilage in white.

non-resection femur model was corroborated against the results from the control femora group in the cadaver study. Appropriate boundary conditions were applied, and compressive loading was applied to the head at the same rate as in the experimental study. Mean age for the cadavers was 79 years (range of 57–98 years) so the elastic modulus of the cortical and cancellous bone in the model was reduced[34,35] to represent the typical reduction in elastic modulus with age and the degree of osteoporosis. The stiffness of the neck was calculated from the linear portion of the load–displacement curve from the model and was compared to the mean neck stiffness from the cadaveric control group (686 N/mm vs. 638 N/mm).

RESULTS

Four zones of interest (A–D) were defined in the resection region. The depth of the zones was taken to be the coronal plane at a level 1 mm below the maximum resection depth (Fig. 7). Average Von Mises stresses and the yielded volume were calculated for each zone. Average stresses were calculated by multiplying the volume of each element by its corresponding stress value. These results were then added before being

divided by the total volume of the elements in the zone:

$$\text{Average Von Mises stress} = \frac{\sum_i V_{E_i} S_{E_i}}{\sum V_{E_i}} \qquad (1)$$

where V_{E_i} is the volume of the ith element of the zone under consideration, S_{E_i} is the Von Mises stress in the ith element of the zone.

Figures 8–11 show the average Von Mises stress and the volume of material yielded in the inferior-medial (A), superior-medial (B), superior-lateral (C), and inferior-lateral (D) areas of the resection, respectively, for the different resection depths and activities. Higher Von Mises stresses were obtained for the knee bend, normal walking, and walking down stairs activities. In the case of the B and C resection areas, the knee bend had the highest average stresses at all resection depths (Figs. 8a–11a). For the remaining two resection areas (A and D), the results for knee bend, normal walking, and walking down stairs activities were similar, between 1.4 and 2.5 times greater for the maximum resection depth compared to the non-resection case.

Table 1. Material Properties for the Two Types of Bone and Cartilage Used in the Model

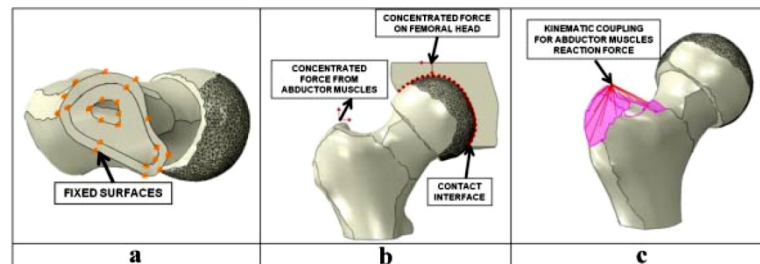| Material	Young's Modulus, E (MPa)	Poisson's Ratio	Yield Stress, σ (MPa)	Material Behavior
Cortical bone	17,000	0.3	100	Homogeneous, elastic-plastic, isotropic
Cancellous bone	150	0.3	6	Homogeneous, elastic-plastic, isotropic
Cartilage	12	0.4	5	Homogeneous, elastic-plastic, isotropic

4   ALONSO-RASGADO ET AL.

Figure 5.   Boundary conditions: (a) Bottom fixed in all directions. (b) Concentrated forces. (c) Kinematic coupling.

$$F_M \cos(\Theta_2) + W = F_{FH} \cos\Theta_1$$
$$F_M \sin(\Theta_2) = F_{FH} \sin\Theta_1$$

CG = CENTRE OF GRAVITY
W = BODY WEIGHT
F$_{FH}$ = REACTION FORCE ON FEMORAL HEAD
F$_M$ = REACTION FORCE FROM ABDUCTOR MUSCLES
Θ_1 = ANGLE BETWEEN ACTION LINES OF **W** AND **F$_{FH}$**
Θ_2 = ANGLE BETWEEN ACTION LINES OF **W** AND **F$_M$**
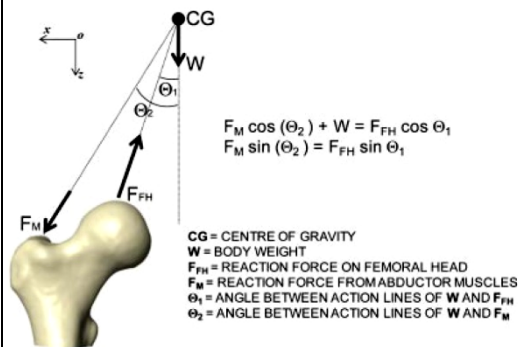
Figure 6.   Free body diagram of one side of the upper part of the body.

In all the cases, average Von Mises stress increased with resection depth. In the case of A, B, and D resection areas, the rate of increase in average stress became greater at resections ≥10 mm, corresponding to depths equal to ~1/3 of the average diameter of the neck and beyond. At resection depths <1/3 of the diameter of the neck (depths of <10 mm), the volume of material yielded was small (Figs. 8b–11b). The volume yielded increased significantly at resection

depths of 10 and 15 mm, corresponding to 1/3 and 1/2 of the neck diameter, respectively. Yielding was confined to the cortical bone and was only significant in the knee bend, normal walking, and walking down stairs activities. The yield pattern suggests that for resections depths of 1/3 and 1/2 of the neck diameter, fracture is likely in the resected area expanding to the femoral neck (Fig. 12, with yielded areas depicted in red).

Contour Plot Analysis

Figure 12 shows the average Von Mises stress distribution in the femoral head and neck for the knee bend activity at resection depths equivalent to ≥1/3 the diameter of the neck. At a resection depth of ~1/3 the diameter of the neck (10 mm), stress reached the yield in the area of the resection region, and over a small portion of the neck (depicted in red). At this depth, the areas where yield was reached were limited to the surface and cortical bone. As resection depth increased to 1/2 the diameter (15 mm) the yielded area expanded to the neck region surface and internally in the cortical bone.

DISCUSSION

In general, both the average Von Mises stresses and the area of yielded bone significantly increased at a

Table 2.   Variables Considered in the Model

Activity	Angles	W (N)	% W	F$_M$ (N)	F$_M$ (N) Components	F$_{FH}$ (N)	F$_{FH}$ (N) Components
1 leg stand	$\Theta_1 = 13°$ $\Theta_2 = 20°$	785	90	1,303.70	F$_{M(X)}$ = 445.89 F$_{M(Z)}$ = 1,225.07	1,982.36	F$_{FH(X)}$ = −445.93 F$_{FH(Z)}$ = −1,931.55
Normal walking	$\Theta_1 = 13°$ $\Theta_2 = 20°$	785	238	3,447.57	F$_{M(X)}$ = 1,179.13 F$_{M(Z)}$ = 3,239.65	5,242.26	F$_{FH(X)}$ = −1,179.25 F$_{FH(Z)}$ = −5,107.90
Down stairs	$\Theta_1 = 12°$ $\Theta_2 = 20°$	785	260	3,049.25	F$_{M(X)}$ = 1,042.90 F$_{M(Z)}$ = 2,865.35	5,015.96	F$_{FH(X)}$ = −1,042.87 F$_{FH(Z)}$ = −4,906.34
Knee bend	$\Theta_1 = 16°$ $\Theta_2 = 20°$	785	143	4,435.19	F$_{M(X)}$ = 1,516.92 F$_{M(Z)}$ = 4,167.71	5,503.63	F$_{FH(X)}$ = −1,517.00 F$_{FH(Z)}$ = −5,290.42
2-1-2 legs stand	$\Theta_1 = 7$ $\Theta_2 = 20°$	785	231	982	F$_{M(X)}$ = 336.00 F$_{M(Z)}$ = 923.00	2,757	F$_{FH(X)}$ = −355.00 F$_{FH(Z)}$ = −2,737.00

W, body weight considered for an individual of 80 kg. From Bergman et al.,[33] %*W*, percent of body weight according to the activities. $F_{M(X)}$,: component of the reaction force from the abductor muscles on the axis X. $F_{M(Z)}$, component of the reaction force from the abductor muscles on the axis Z. $F_{FH(X)}$, component of the reaction force on the femoral head on the axis X. $F_{FH(Z)}$, component of the reaction force on the femoral head on the axis Z.
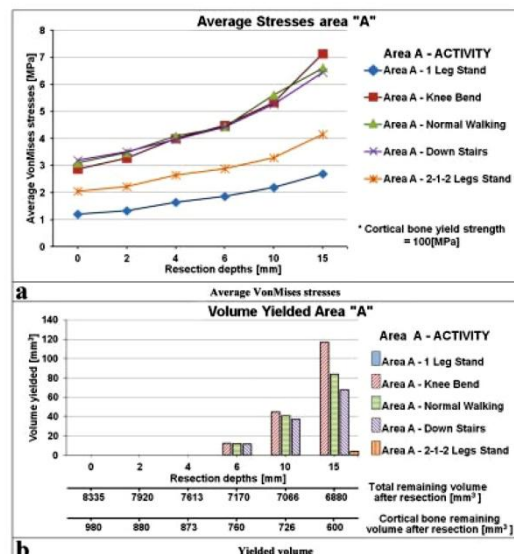
Table 3. Number of Tetrahedral Elements Employed for the Cartilage, Cortical, and Trabecular Bones for the Different Resections Considered

Resection Depth (mm)	Tetrahedral Elements			
	Cortical	Trabecular	Cartilage	Total
0	25,959	55,465	9,644	91,068
2	28,586	55,465	9,403	93,695
4	26,453	57,231	9,248	92,932
6	25,333	58,976	9,453	93,762
10	24,991	61,043	8,702	94,736
15	24,189	67,056	8,551	99,796

Figure 8. (a) Average stress and (b) yielded volume in the area A (inferior-medial of the resection area) for the six resection depths and five activities.

resection depth of ≥ 10 mm (33%), suggesting that when surgeons perform osteochondroplasty the depth of resection should be limited to 33% as a maximum. The activity of knee bending was the critical activity as in general it resulted in higher stresses than the other activities considered. The stress produced by the knee bend was between 1.5 and 2.5 times greater for the maximum resection depth investigated compared to the non resection case. The model predicted that yield was reached in the resection area at depths >10 mm or 1/3 the femoral neck diameter for the knee bend, normal walking, and walking down stairs, suggesting that patients should be advised to partial weight-bear on crutches for a period following surgery. Furthermore, as significant remodeling of the resection area will take considerably longer, patients should be advised to avoid impact type activities and single leg knee bends for a period post-operatively. The model suggests that bigger resections should probably be protected for longer times, whereas smaller resections can be rehabilitated faster.

As the depth of resection increases from 1/3 the diameter of the neck, the area where yield takes place expands from the resection area into the surface of the neck and inside through the cortical bone. The results suggest that for resection depths of 1/3 and 1/2 of the neck diameter fracture will occur in the resection area, in agreement with a previous experimental study,[17]

which showed that at 30% resection and greater, a change in the femoral head–neck response occurred, resulting in a reduction in the energy required to produce fracture and a modification to the failure pattern, with fracture occurring at the level of the resection. We found that at around 30% resection stresses start to increase sharply leading to yield in the resection area. While the experimental study used only axially loaded specimens, our study goes further by modeling a number of activities, thus providing a realistic expectation of what activities patients may attempt to undertake following surgery.

Our study utilized CT scan data from only one patient, thus restricting the analysis to a single resection
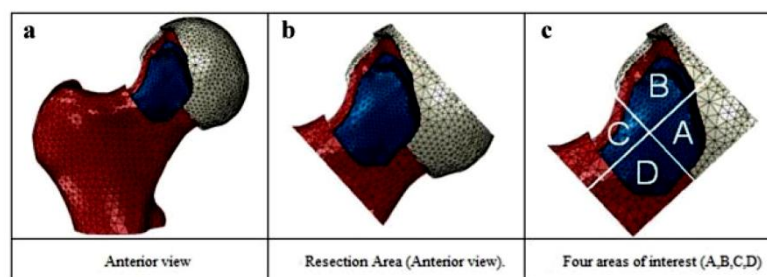
Figure 7. Areas of interest considered in the analysis. (a) Anterior view. (b) Resection area (anterior view). (c) Four areas of interest (A,B,C,D).
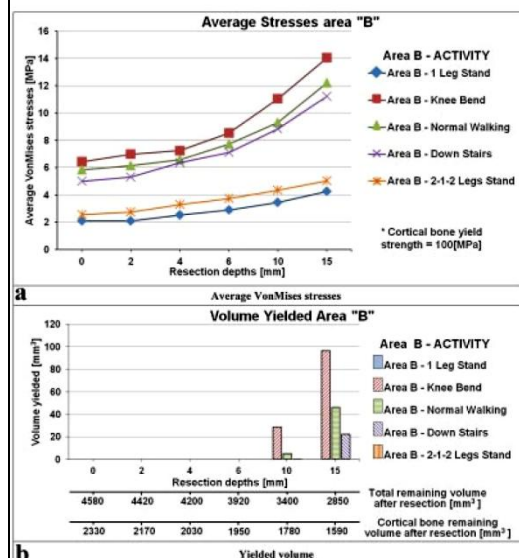
6   ALONSO-RASGADO ET AL.

Figure 9. (a) Average stress and (b) yielded volume in the area of interest B (superior-medial of the resection area) for the six resection depths and five activities.

Figure 11. (a) Average stress and (b) yielded volume in the area D (inferior-lateral of the resection area) for the six resection depths and five activities.

area. But the results suggest that the stresses in the head and neck primarily depend on the resection depth relative to the overall neck diameter, and we believe that our findings are widely applicable.
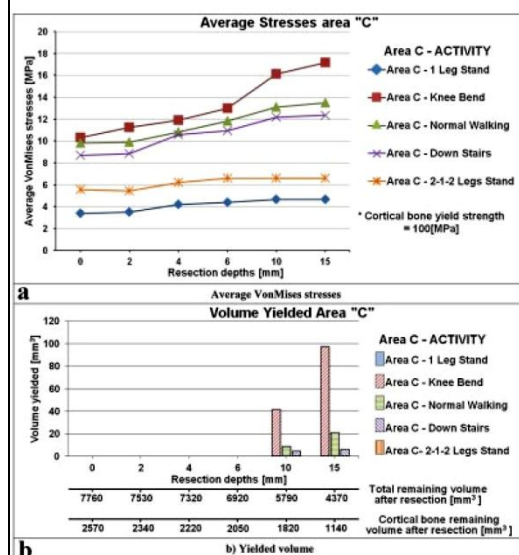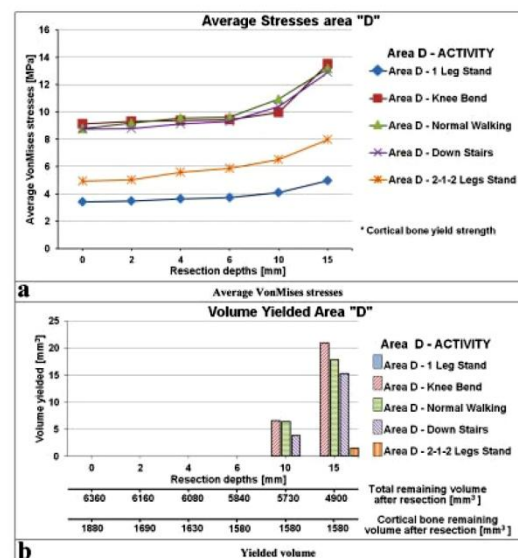

Figure 10. (a) Average stress and (b) yielded volume in the area C (superior-lateral of the resection area) for the six resection depths and five activities.

Our study had limitations and simplifications; for example, the virtual resection created was not as smooth as one that would be produced during surgery. However, a large number of elements were employed in these areas to accurately describe the geometry. Furthermore, the volume of each element was considered when calculating the stress; therefore, a reasonable degree of confidence can be associated with the predictions. The static model we developed utilizes "typical" average peak hip contact forces[33] to provide an indication of the resected neck's response to load conditions resulting from various daily activities. Though the response to loading throughout the entire gait cycle was not considered, the model provides useful and insightful predictions and reinforces those obtained in a previous study.[17]

Fracture propensity assessments were reported based on average Von Mises stress and the volume of elements exceeding yield. While it may be argued that maximum principal stress is more applicable to fracture assessment, we decided to report Von Mises stress because four reasons. First, a detailed assessment of fracture propensity was outside the scope of our study. The main focus was to investigate changes in stress patterns due to resections performed to avoid impingement. Hence, it was necessary to capture the changes in shape of the femoral head. Von Mises stress is an estimate of distortional energy in a loaded body; therefore, it was chosen for our study. Second, the authors performed another set of analysis examining maximum principal stresses and the trend of the average
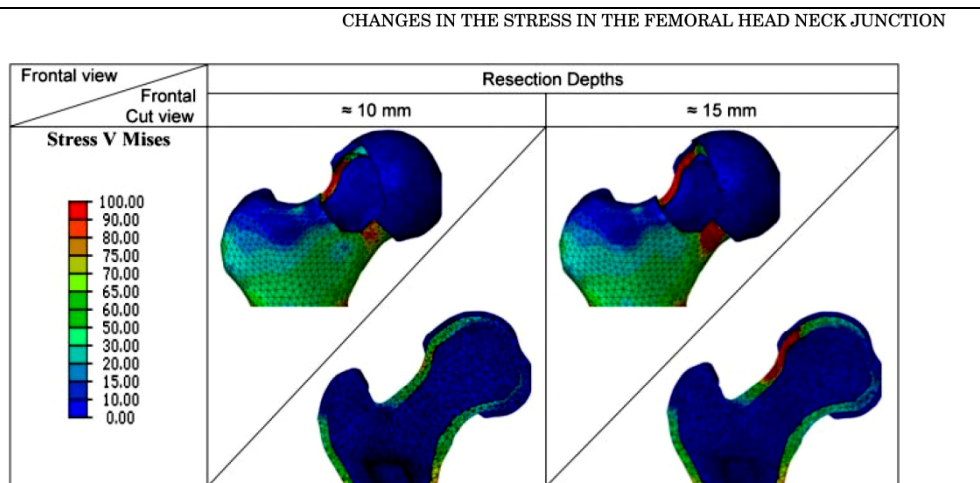
Figure 12. Von Mises stress distribution knee bend activity.

values of Von Mises and maximum principal stress for the various levels of resection was broadly similar. Third, numerical values of maximum stress may be high at a point due to surface irregularities after a virtual resection is performed. These irregularities may be absent in patients, but are hard to avoid in a numerical model due to non-uniform element sizes. Hence, an average stress was reported. Finally, many studies used Von Mises stress to report mechanical stresses in bones.[36–38] Adopting a similar metric may help researchers compare our results with the literature.

Our model considered cancellous bone as exhibiting elastic-plastic, isotropic material behavior. The intact femur model using these properties was successfully corroborated against the results from a cadaveric investigation,[17] so the material properties employed are sufficiently accurate for this study. In addition, while we recognize that the elastic modulus of cancellous bone depends primarily on apparent bone density, the exact form of the dependency is controversial.[39] The issue is further complicated by the dependency of the relationship on loading direction, trabecular orientation, and anisotropy. We acknowledge, however, that within a single anatomical site density range is limited,[39] which suggests that an invariant bone property, as was used in this article, should enable relatively accurate predictions to be obtained.

In conclusion, our results suggest that to ensure integrity of the femoral head and neck, resection depth should be kept to <10 mm or 1/3 of the diameter of the neck.

ACKNOWLEDGMENTS

REFERENCES

1. Ganz R, Parvizi J, Beck M, et al. 2003. Femoroacetabular impingement. A cause for osteoarthritis of the hip. Clin Orthop Relat Res 417:112–120.
2. Fadul DA, Carrino JA. 2009. Imaging of femoroacetabular impingement. J Bone Joint Surg Am 91:138–143.
3. Kassarjian A, Brisson M, Palmer WE. 2007. Femoroacetabular impingement. Eur J Radiol 63:29–35.
4. Sink EL, Gralla J, Ryba A, et al. 2008. Clinical presentation of femoroacetabular impingement in adolescents. J Pediatr Orthop 28:806–811.
5. Tannast M, Siebenrock KA, Anderson SE. 2007. Femoroacetabular impingement: radiographic diagnosis–what the radiologist should know. AJR Am J Roentgenol 188:1540–1552.
6. Bardakos NV, Vasconcelos JC, Villar RN. 2008. Early outcome of hip arthroscopy for femoroacetabular impingement: the role of femoral osteoplasty in symptomatic improvement. J Bone Joint Surg Br 90:1570–1575.
7. Ganz R, Leunig M, Leunig-Ganz K, et al. 2008. The etiology of osteoarthritis of the hip: an integrated mechanical concept. Clin Orthop Relat Res 466:264–272.
8. Horisberger M, Brunner A, Herzog R. 2010. Arthroscopic treatment of femoroacetabular impingement of the hip. A new technique to access the joint. Clin Orthop Relat Res 468:182–190.
9. Ito K, Leunig M, Ganz R. 2004. Histopathologic features of the acetabular labrum in femoroacetabular impingement. Clin Orthop Relat Res 429:262–271.
10. Jaberi FM, Parvizi J. 2007. Hip pain in young adults: femoroacetabular impingement. J Arthroplasty 22:37–42.
11. Jager M, Wild A, Westhoff B, et al. 2004. Femoroacetabular impingement caused by a femoral osseous head–neck bump deformity: clinical, radiological, and experimental results. J Orthop Sci 9:256–263.
12. Kassarjian A, Belzile E. 2008. Femoroacetabular impingement: presentation, diagnosis, and management. Semin Musculoskelet Radiol 12:136–145.
13. Leunig M, Beaule PE, Ganz R. 2009. The concept of femoroacetabular impingement: current status and future perspectives. Clin Orthop Relat Res 467:616–622.

8   ALONSO-RASGADO ET AL.

14. Leunig M, Beck M, Dora C, et al. 2005. Femoroacetabular impingement: etiology and surgical concept. Oper Tech Orthop 15:247–255.
15. Leunig M, Ganz R. 2009. FAI—concept and etiology. FAI—Konzept und Ätiopathogenese. Orthopäde 38:394–401.
16. Leunig M, Robertson W, Ganz R. 2007. Femoroacetabular impingement: diagnosis and management, including open surgical technique. Oper Tech Sports Med 15:178–188.
17. Mardones RM, Gonzalez C, Chen Q, et al. 2005. Surgical treatment of femoroacetabular impingement: evaluation of the effect of the size of the resection. J Bone Joint Surg Am 87:273–279.
18. Philippon MJ, Briggs KK, Yen YM, et al. 2009. Outcomes following hip arthroscopy for femoroacetabular impingement with associated chondrolabral dysfunction: minimum two-year follow-up. J Bone Joint Surg B 91:16–23.
19. Ganz R, Gill TJ, Gautier E, et al. 2001. Surgical dislocation of the adult hip. A technique with full access to the femoral head and acetabulum without the risk of avascular necrosis. J Bone Joint Surg Br 83:1119–1124.
20. Dooley PJ. 2008. Femoroacetabular impingement syndrome: nonarthritic hip pain in young adults. Can Fam Physician 54:42–47.
21. Petit CJ, Philippon MJ. 2008. Arthroscopic management of osteochondral defects of the hip. Oper Tech Sports Med 16:194–200.
22. Philippon M, Schenker M, Briggs K, et al. 2007. Femoroacetabular impingement in 45 professional athletes: associated pathologies and return to sport following arthroscopic decompression. Knee Surg Sports Traumatol Arthrosc 15:908–914.
23. Sampson TG. 2005. Complications of hip arthroscopy. Tech Orthop 20:63–66.
24. Sampson TG. 2005. Arthroscopic treatment of femoroacetabular impingement. Tech Orthop 20:56–62.
25. Gedouin J-E, May O, Bonin N, et al. 2010. Assessment of arthroscopic management of femoroacetabular impingement. a prospective multicenter study. Orthop Traumatol Surg Res 96S:S59–S67.
26. Laude F, Sariali E, Nogier A. 2009. Femoroacetabular impingement treatment using arthroscopy and anterior approach. Clin Orthop Relat Res 467:747–752.
27. Ilizaliturri VM. 2009. Complications of arthroscopic femoroacetabular impingement treatment. Clin Orthop Relat Res 467:760–768.
28. Anderson AE, Ellis BJ, Maas SA, et al. 2008. Validation of finite element predictions of cartilage contact pressure in the human hip joint. J Biomech Eng 130:051008.
29. Augat P, Link T, Lang TF, et al. 1998. Anisotropy of the elastic modulus of trabecular bone specimens from different anatomical locations. Med Eng Phys 20:124–131.
30. Chegini S, Beck M, Ferguson SJ. 2009. The effects of impingement and dysplasia on stress distributions in the hip joint during sitting and walking: a finite element analysis. J Orthop Res 27:195–201.
31. Dickenson RP, Hutton WC, Stott JRR. 1981. The mechanical properties of bone in osteoporosis. J Bone Joint Surg Br 63:233–238.
32. Li B, Aspden RM. 1997. Composition and mechanical properties of cancellous bone from the femoral head of patients with osteoporosis or osteoarthritis. J Bone Miner Res 12:641–651.
33. Bergmann G, Deuretzbacher G, Heller M, et al. 2001. Hip contact forces and gait patterns from routine activities. J Biomech 34:859–871.
34. Little JP, Taddei F, Viceconti M, et al. 2007. Changes in femur stress after hip resurfacing arthroplasty: response to physiological loads. Clin Biomech 22:440–448.
35. Lotz JC, Cheal EJ, Hayes WC. 1995. Stress Distributions within the proximal femur during gait and falls: implications for osteoporotic fracture. Osteoporos Int 5:252–261.
36. Innocenti B, Truyens E, Labey L, et al. 2009. Can medio-lateral baseplate position and load sharing induce asymptomatic local bone resorption of the proximal tibia? A finite element study. J Orthop Surg Res 4:26.
37. Zhao X, Chosa E, Totoribe K, et al. 2010. Effect of periacetabular osteotomy for acetabular dysplasia clarified by three-dimensional finite element analysis. J Orthop Sci 15:632–640.
38. Taddei F, Cristofolini L, Martelli S, et al. 2006. Subject-specific finite element models of long bones: an in vitro evaluation of the overall accuracy. J Biomech 39:2457–2467.
39. Keaveny TM, Morgan EF, Niebur GL, et al. 2001. Biomechanics of trabecular bone. Annu Rev Biomed Eng 3:307–333.